Engineering the electronic structure of two dimensional chalcogenide materials

Alexander John Armstrong

PhD

University of York

Physics

August 2024

Abstract

As two dimensional materials technology matures and the focus turns to optimization, fine tuning the optoelectronic properties of materials is becoming necessary for progress. The focus of this thesis is on developing methods to achieve such modulation in terms of variation of the band gap and introduction of dopants within the two dimensional chalcogenide family of semiconductors. Changing the structure of materials can change the band structure within the optically relevant band gap region of materials by either changing the energies of existing bands to modify the band gap, or by introducing new 'defect' states within this region.

Three methods of such optoelectronic property modulation are investigated within this thesis - uniaxial strain, point defects and edge defects. The investigations into uniaxial strain focus on band gap variation in monolayer MoS_2, TiS_3 using first principle calculations and in monolayer WS_2 experimentally. The first principle calculations reveal a high directional dependence of uniaxial strain on the band gap response in TiS_3 compared to MoS_2, while the experimental investigation focused more on optimization of strain introduction - achieved through deposition of WS_2 on pillars.

The point defects study focuses on the potential for p and n type doping within four layer MoS_2 through the introduction of oxygen and chlorine dopants - finding oxygen an unsuitable candidate for p type doping (without inclusion of substrate effects) and chlorine a candidate for electron donation. Edge defects are also investigated using first principles calculations in a WS_2 system, focusing on the impact of different edge terminations on the introduction of optically relevant defect states. Armchair terminations are found to reduce the band gap significantly, with terminations between armchair and zigzag directions able to modulate this reduction to some degree, and zigzag terminations resulting in a metallic structure.

Acknowledgements

Formal Acknowledgements

I would like to thank my supervisors Prof. Keith McKenna and Dr. Yue Wang for their support and guidance throughout the project. Their insight has been extremely valuable in making the project possible. I would also like to thank the many members of both the photonics and McKenna materials modelling research groups who have helped me throughout. I also thank our industrial collaborators, AIXTRON, who provided WS_2 samples as well as well as our academic collaborators in the nano and optoelectronics research laboratory at Istanbul university.

Informal Acknowledgements

While many people from both research groups have helped me throughout my PhD, I would like to specifically thank Adam, Tom and Ieuan from the McKenna materials modelling who were particularly helpful. Discussions with Tom and Ieuan in the office were invaluable for both illuminating difficult topics and helping to spot the variety of mistakes I made along the way. Adam was especially helpful and patient in helping me understand the intricacies of VASP at the start of my PhD. From the photonics research group I'd particularly like to thank Sam for many discussions during teaching labs about the various frustrations of life as a PhD student - this definitely helped maintain a certain level of sanity through the more difficult periods.

Outside of the university, my family and friends have also been of extreme importance in helping me through the hard times - especially my partner Robin who has put up with multiple rants about various seemingly impossible to solve problems. I am exceedingly grateful for the unending support and generosity you have shown me and look forward to returning this kindness in the years to come.

Declaration

I declare that this thesis is a presentation of my own work, unless otherwise stated within the text. This work has not previously been presented for an award at this, or any other, University. All sources are acknowledged as References.

Publications

The following is a list of publications which contribute to this thesis. All chapters which use wording from such publications mention the relevant publications at the beginning of each chapter.

1. Alex Armstrong, Keith P. McKenna, and Yue Wang. Directional dependence of band gap modulation via uniaxial strain in MoS2 and TiS3. Nanotechnology, 35(1):015704, 10 2023.

2. Fahrettin Sarcan, Alex J. Armstrong, Yusuf K. Bostan, Esra Kus, Keith P. McKenna, Ayse Erol, and Yue Wang. Ultraviolet-Ozone Treatment: An Effective Method for Fine-Tuning Optical and Electrical Properties of Suspended and Substrate-Supported MoS2. Nanomaterials 2023, Vol. 13, Page 3034, 13(23):3034, 11 2023.

Contents

List of Figures

List of Tables

Abbreviations

DFT density functional theory

BZ Brillouin zone

GGA generalised gradient approximation

PBE Perdew-Burke-Ernzerhof

PL photoluminescence

HSE06 Heyd-Scuseria-Ernzerhof

VASP Vienna *ab initio* simulation package

SOC spin-orbit coupling

CBM conduction band minimum

VBM valence band maximum

XRD x-ray diffraction

CVD chemical vapour deposition

LDA local density approximation

TMDs transition metal dichalcogenides

ML monolayer

SOC spin orbit coupling

AFM atomic force microscope

TISE time independent Schrödinger equation

HF Hartree-Fock

vdW van der Waals

PAW projector augmented wave

CCD charge coupled device

2D two dimensional

3D three dimensional

UV ultraviolet

hBN hexagonal Boron Nitride

PMMA Poly(methyl methacrylate)

IR infrared

IPA isopropyl alcohol

PDMS polydimethylsiloxane

MBE molecular beam epitaxy

CVD chemical vapour deposition

EBL electron beam lithography

RIE reactive ion etching

LED light emitting diode

SEM scanning electron microscopy

GDS graphical data stream

DOS density of states

TMD transition metal dichalcogenide

STM scanning tunneling microscopy

Chapter 1

Introduction

1.1 Motivation

As the technology surrounding two dimensional (2D) semiconductors matures - with a variety of applications developing in areas such as flexible electronics, photonics, and catalysis [1–5] - it is becoming more important for electronic properties to be fine-tuned to enable tailoring of their properties for specific applications. One approach to tailoring electronic properties is the introduction of defects within the crystal, which often alters energies of electronic states without the need for external fields to be applied. These changes can modify the optoelectronic properties of materials when such states are situated close to or within the band gap [6]. A number of point and extended defect types can be present in materials, the impact of which are not fully understood in many cases in part due to the large configuration space such a problem involves. This provides an exciting avenue for research with many open questions. Although not technically a defect, introduction of crystal strain can also be used as a mechanism for modifying the properties of materials in a similar manner [7]. This thesis presents a study of the effects of both strain and a number of specific defect types on the

properties of 2D transition metal chalcogenides (MoS_2, WS_2 and TiS_3) - with a focus on changes in their electronic properties by tuning the band gap in order to engineer the photoluminescence spectrum of such materials.

1.2 Two dimensional materials

With the advent of exfoliation techniques pioneered in the exfoliation of graphene in 2004 a new parameter space opened up for research into novel 2D materials [8]. Such materials have a layered structure, with the shared characteristic of high in-plane strength and weak out-of-plane van der Waals interactions between layers, enabling easy separation of layers to form mono- to few-layer materials [9]. Many materials exist with these properties, with a wide variety of electronic properties; including insulators, metals and semiconductors. Graphene is often used in devices requiring an electrical conductor, as it is a semi-metal with the conduction band minimum (CBM) and valence band maximum (VBM) touching at a single point - known as the Dirac point (shown in Fig. 1.1 [10]). Other applications require a material with a band gap, such as the 2D insulator hexagonal Boron Nitride (hBN) which is often used in 2D electrical devices to prevent current flow. A huge advantage of van der Waals (vdW) materials is their ability to be easily stacked: stacking layers of different materials changes the properties of both due to interlayer interactions. This effectively produces a new material called a heterostructure; an illustration of this concept is shown in Fig. 1.2 [11]. This thesis focuses specifically on semiconductors: materials with a band gap small enough for electrons from the VBM to be excited into the CBM with energies accessible at room temperature.

2D semiconductors have emerged as a fertile ground for research in recent years spurred on by both fundamental interest and potential for applications in

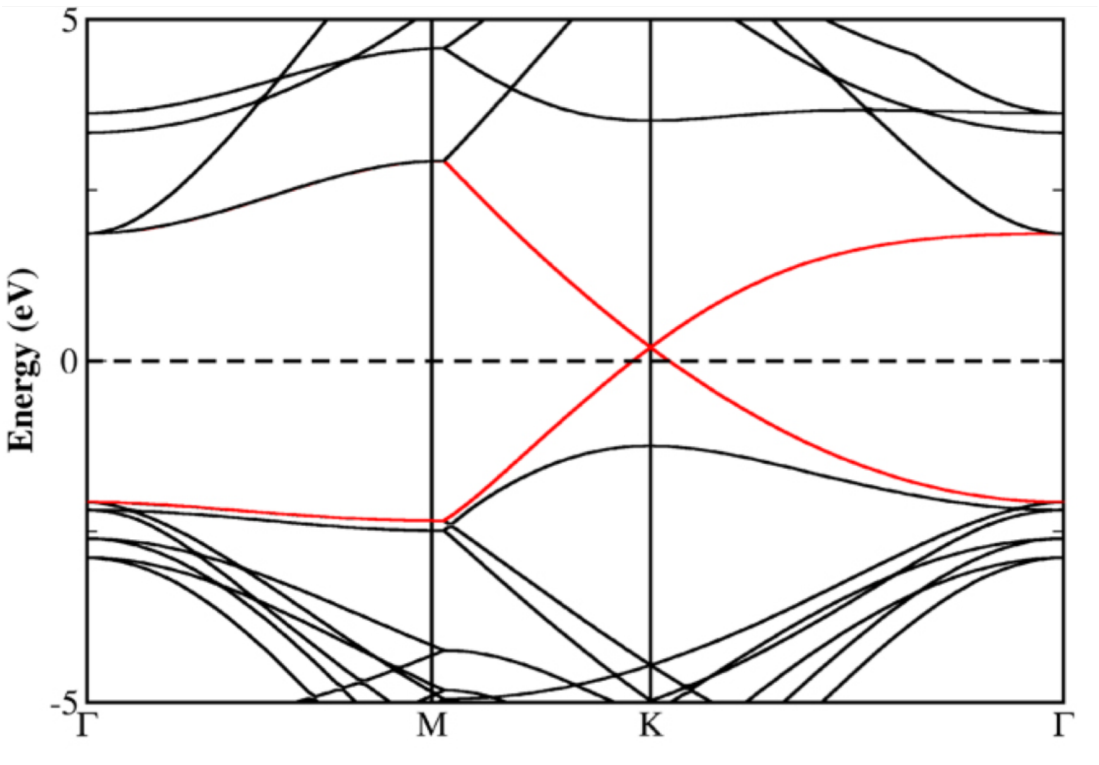

Figure 1.1: DFT-calculated graphene band structure, showing the Dirac point at K in red. Reproduced from [10] under creative commons licence.

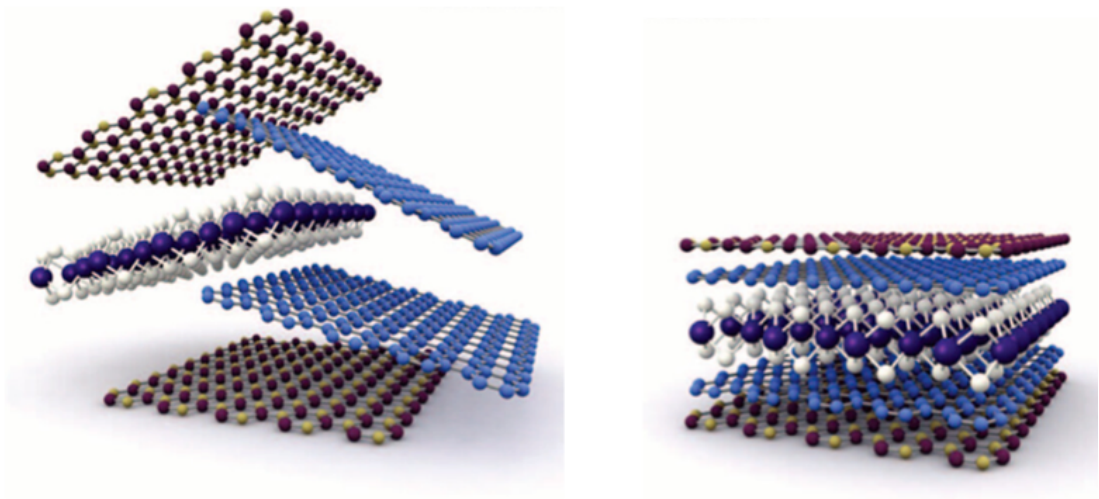

Figure 1.2: Illustration of heterostructure concept, showing layers of a transition metal dichalcogenide encapsulated with hexagonal boron nitride layers, all encapsulated in graphene layers - which could function as an LED. Reproduced from [11] under creative commons licence.

photonics, catalysis and nanoelectronics [1–5]. Their low dimensionality can often result in interesting optoelectronic properties such as high carrier mobility and photoluminescence due to charge carrier confinement within a plane [12]. Such materials can have a range of band gaps leading to emission and absorption across a range of wavelengths, for example within the visible, infrared (IR), and near-IR wavelength ranges. A non-exhaustive list of examples of 2D materials and their emission wavelengths is shown in Table 1.1. These emission wavelengths are experimentally determined thus include the exciton binding energy. This often results in large discrepancy compared to the electronic band gap emission wavelengths calculated through density functional theory (DFT) calculations, as excitonic effects are not included.

Table 1.1: Comparison of monolayer direct band gaps in a variety of 2D materials, stated in both energy and wavelength, with associated references.

Material	E_g (eV)	E_g (nm)	Reference
Molybdenum disulfide	1.9	650	[13]
Titanium trisulfide	1.1	1130	[14]
Tungsten disulfide	2.1	590	[15]
Hexagonal boron nitride	5.9	210	[16]
Black phosphorous	0.3	4100	[16]
Molybdenum ditelluride	1.1	1130	[17]

A key example of active research in this area is within silicon photonics; silicon has an indirect band gap, making it an inefficient photon emitter/absorber for use in photonic devices [18]. A material with a direct band gap smaller than that of silicon would be able to interface with the mature silicon technology - enabling charge carriers in silicon to be injected and radiatively recombine to emit light more efficiently than in silicon alone [19]. 2D semiconductors provide a potential avenue to achieving such an interface due to their potential for band structure engineering and the large space for materials discovery they represent.

Three 2D semiconductors are considered within this thesis in a combination

of theoretical and experimental studies: two hexagonal structures with similar structures to graphene - MoS_2 and WS_2 - and a more anisotropic material with monoclinic structure TiS_3. It should be noted that the similarity between MoS_2 and WS_2 comes from their hexagonal structure, however these materials involve more elements. This means that each carbon site in graphene is replaced by a metal and two sulfur atoms - resulting in a three atoms in a plane compared to one in graphene.

1.3 Strain

Strain within crystals displaces atoms from their equilibrium positions in the bulk and can be induced using a variety of methods. Lattice mismatch is one mechanism where the lattice constant of a material is not commensurate with the underlying substrate [20]. This can cause either a change in lattice constant to fit the substrate or, in the cases of larger strain, induce dislocation defects within the crystal - as illustrated in Fig. 1.3. Such a method has limited tunability, as the level of strain introduced is dependent on the ratio of unstrained lattice constants in the crystal and substrate [21]. Lattice constants are dictated by the materials used, thus there are a discrete number of options for tuning in this manner. The picture for 2D materials is a little different with interlayer interaction being limited to the van der Waals interaction and hence being quite weak. This also extends to the substrate [22]. While the substrate can still induce strain within a 2D crystal, the effect is less easily modelled as these weak interactions mean the lattice is more free to relax over a longer length scale, introducing periodicity over a length scale much larger than the primitive cell of the 2D crystal alone [23]. Strain is important within 2D materials, and has emerged as a method of varying the band structure in 2D materials to tune both

optical and electronic properties for different applications due to the high strains such materials can withstand [24]. For example, local strain due to wrinkles has been shown to cause a 'funneling' effect, moving carriers towards strained areas - a phenomenon potentially useful for single photon emission [24]. More generally, the method has been extensively shown to modify the band gap in transition metal dichalcogenides (TMDs) and other van der Waals materials, enabling the emission wavelength to be tuned via strain [25,26]. As a result of these interesting modifications of electronic properties such as band structure, various methods for inducing strain within such materials have been developed such as transferring to a flexible substrate to enable stretching or bending of the system more easily, or inducing strain via a nanofabricated patterned substrate [25].

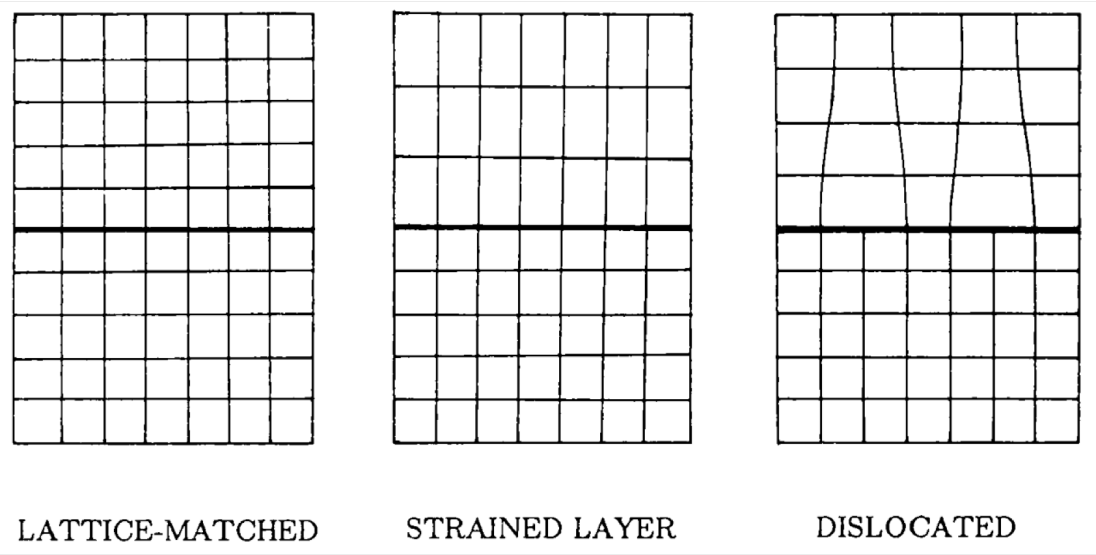

Figure 1.3: Illustration of lattice mismatch between crystal and substrate, with a grid representing atomic sites. Reproduced from [21] with permission.

1.4 Defects

Crystal defects can have different dimensionality, for example point defects (zero dimensional), line defects (one dimensional) and surfaces/interfaces (two dimen-

sional). The study of defects is therefore a broad topic, with this thesis focusing mainly on the effects of point and edge defects within 2D materials.

Point defects exist in many varieties, the simplest being vacancy defects where a single atom is removed from the equilibrium structure, or a substitution where an atom is simply substituted for a different species. More complex point defects can also exist like antisite or interstitial defects, with atoms removed and replaced at different positions within the crystal. Fig. 1.4 shows some examples of such defects [27].

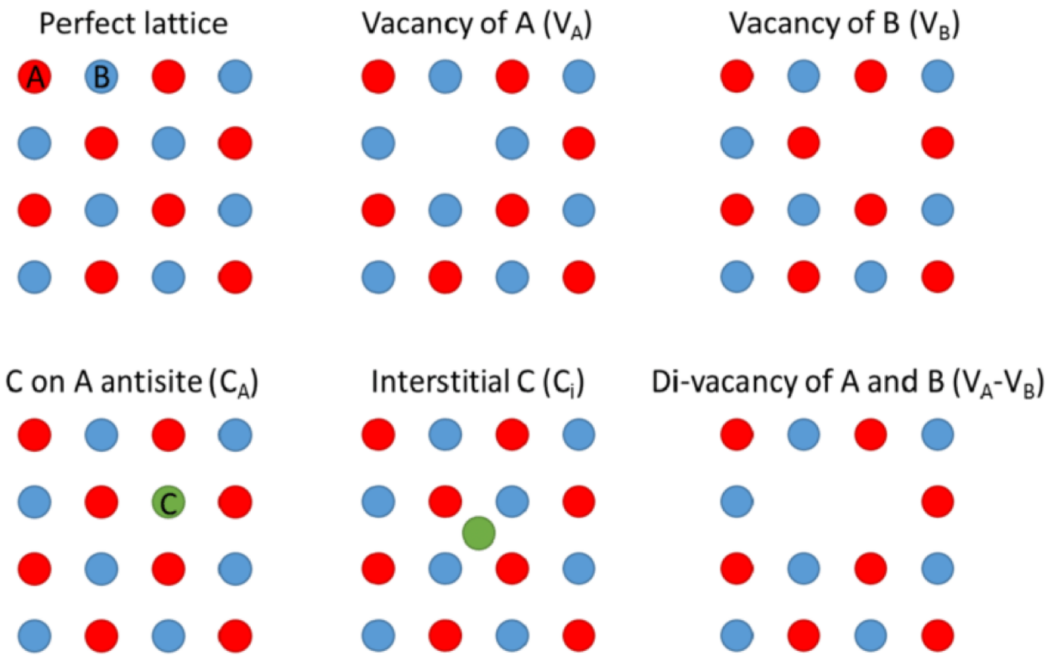

Figure 1.4: Diagrams showing various point defects. Reproduced from [28] under creative commons license.

The introduction of defects can lead to reconstruction of the surrounding atoms, creating a localized strain field around the defect and often introducing new electronic states - called defect states - into the crystal's band structure [29]. For low concentrations, point defects introduce non-dispersive electronic states into the system. A shallow defect state within the band gap can reduce the energy

for an electron or hole to localize on this defect relative to a free charge carrier. This causes charge trapping, while a deeper defect closer to the centre of the band gap could cause both electrons and holes to localize, resulting in electron-hole recombination. Point defects can have a significant effect on electronic and optical properties of the material and are thus important to understand. It is important to note that defects can have a range of effects on various properties and do not always negatively impact crystal properties, depending upon the application [30]. For example, electron donor or acceptor atoms can be chosen to form defects within a crystal, creating n-type or p-type doping respectively. This can be useful for applications such as transistors, which often require both n and p-type components [31].

Edges in 2D materials are rapidly becoming an important defect as devices are being realized. The standard example of graphene highlights this importance, as clean edges have been found necessary to avoid excessive electron scattering in devices. This has driven research into growing graphene with atomically sharp edges [32]. Because such defects introduce a difference in symmetry in a crystal, they can also have an effect on the band structure. Using a hexagonal structure crystal as an example, which is a common structure within 2D chalcogenide materials, several different edges can be present at an edge termination. The simplest examples of these are along the two high symmetry directions, known as the 'armchair' and 'zigzag' directions. Other edges can exist, for example if the unit cell were terminated at some angle in between the armchair and zigzag directions, a series of kink defects would be formed, with a mixture of zigzag and armchair terminations. These edges can not therefore be modelled as the sum of armchair and zigzag termination properties, as such edges could result in a different reconstruction of atoms at the termination - likely exhibiting different properties. Fig. 1.5 highlights these different terminations for the example of

WS_2.

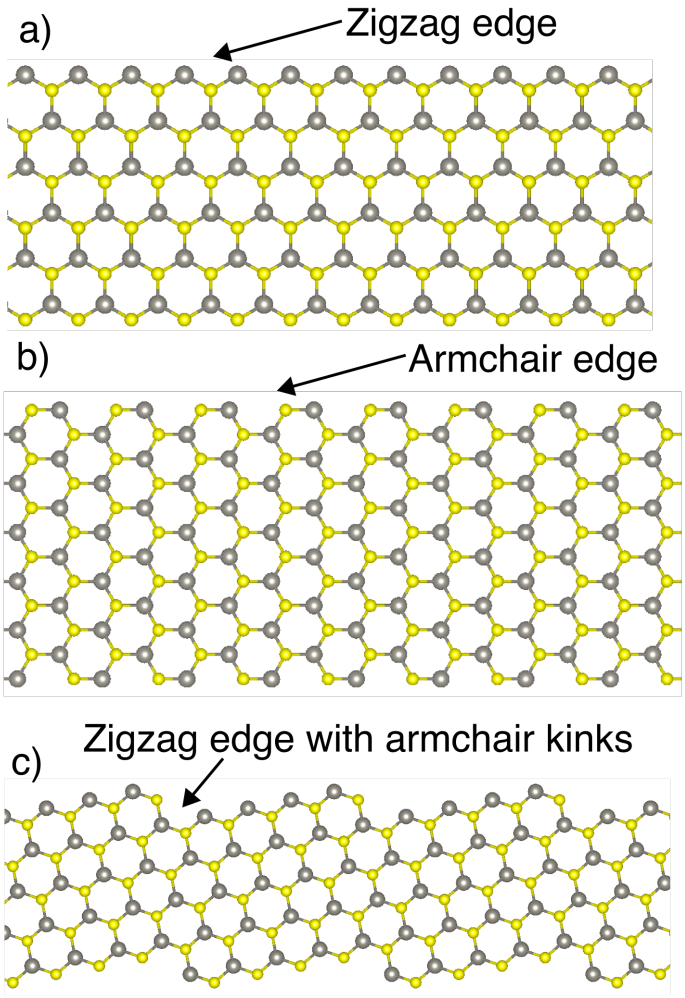

Figure 1.5: Structures of different edge terminations present in WS_2 nanoribbons, showing a) zigzag termination, b) armchair edge termination and c) a combination of both zigzag and armchair edges to produce a 'kinked' edge defect.

1.5 Aims of thesis

This thesis aims to provide insight into how defects and strain can be used to modify electronic properties in 2D materials, specifically focusing on examples of

such engineering in MoS_2, WS_2 and TiS_3. Such effects are investigated using a combination of techniques, both experimental and theoretical, such as DFT and photoluminescence (PL).

1.6 Overview of thesis

In this chapter the general motivation for the work presented in later chapters has been given, along with brief background information relevant for 2D materials and defects/strain therein.

Chapter 2 focuses in depth on the theory necessary to describe such systems using DFT and extensions to this theory used within the thesis, then describes theory relevant to the experimental methods.

Chapter 3 focuses on methods used in computational implementation of DFT in practice, and discusses the experimental techniques applicable to this work.

Chapter 4 presents DFT calculations undertaken to investigate the effect on band structure of introducing uniaxial strain along different crystallographic directions - focusing on two representative vdW materials MoS_2 and TiS_3 and the differences between them.

Chapter 5 describes on experimental work undertaken on WS_2 monolayer samples strained by fabricated nanopillars on a substrate. Steps are taken within this chapter to characterise how such strain affects the band gap via photoluminescence studies.

Chapter 6 presents calculations undertaken to describe potential defects present in MoS_2 treated with UV-ozone - providing insight into different possible mechanisms for electron trapping. This is motivated by experimentally observed p-type doping in 4-layer MoS_2 via UV-ozone treatment.

Chapter 7 presents DFT calculations for WS_2 edge defects, investigating how

introducing edges of different natures changes the band structure. This could potentially be useful for engineering the electronic properties of such systems.

Finally, chapter 8 summarises the main conclusions of the thesis, along with prospective future work.

Chapter 2

Theory

2.1 Density functional theory

2.1.1 The Many Particle Schrödinger Equation

Solving the Schrödinger equation is central to quantum mechanics, theoretically providing a route to calculating all electronic properties of a given system. In practice there exists the problem that for many particle systems the wavefunction quickly becomes far too complex to calculate. While the single particle solution to the Schrödinger equation involves wavefunctions which depend only on the coordinates of that particle, allowing for quick calculations (or in some cases analytical solutions), the many particle wavefunctions depend on the interactions of each particle with every other particle. This means that a many body wavefunction becomes increasingly complex as the number of particles increases, to such an extent that a numerical solution quickly becomes impossible to store on even the most advanced supercomputers. The interaction between particles also results in a set of coupled differential equations, which are far more complex to solve than independent particle equations.

Several methods exist to tackle this problem, one of the most popular being

DFT. 'Pure' DFT provides a solution to this problem by reformulating the wavefunction as charge density dependent rather than electron coordinate dependent. Orbitals are reintroduced to the problem in the most widely used formulation - Kohn-Sham DFT - but this simplifies the problem to a series of non-interacting single particle problems, vastly reducing the complexity of calculations [33, 34].

2.1.2 Born-Oppenheimer Approximation

The Born-Oppenheimer approximation is central to many quantum mechanical problems and has the effect of decoupling nuclear motion from that of the surrounding electrons for small time scales. This is justified as the electrons have a far smaller mass than that of the nuclei, hence can respond to a change in potential far more rapidly. The reason this simplifies the problem is that the nuclear potential acting on the electrons can then be regarded as fixed with respect to changing electron positions [35].

If nuclear and electronic motion are coupled, a given state is described by the wavefunction, $\Psi_i(\mathbf{r_1}, \mathbf{r_2}, ..., \mathbf{r_n}, \mathbf{R_1}, \mathbf{R_2}, ..., \mathbf{R_N})$, meaning the wavefunction is a function of the positions of all electrons, $\mathbf{r_i}$, and nuclei, $\mathbf{R_i}$. This wavefunction can then be operated on by the Hamiltonian operator, $\hat{\mathcal{H}}$, to calculate the energies of each state according to the time independent Schrödinger equation (TISE):

$$\hat{\mathcal{H}}\Psi_i = E_i\Psi_i. \tag{2.1}$$

The Hamiltonian contains operators for the kinetic energy of nuclei and electrons ($\hat{\mathcal{T}}_n$ and $\hat{\mathcal{T}}_e$ respectively), potential operators for the interactions between them ($\hat{\mathcal{U}}_{ne}$, $\hat{\mathcal{U}}_{ee}$, and $\hat{\mathcal{U}}_{nn}$ for nuclei-electron, electron-electron and nuclei-nuclei interactions respectively), plus an external potential consisting of everything else such

as any external electromagnetic fields applied to the system, $\hat{\mathcal{V}}_{ext}$:

$$\hat{\mathcal{H}} = \hat{\mathcal{T}}_e + \hat{\mathcal{T}}_n + \hat{\mathcal{U}}_{ne} + \hat{\mathcal{U}}_{ee} + \hat{\mathcal{U}}_{nn} + \hat{\mathcal{V}}_{ext}. \tag{2.2}$$

The Born-Oppenheimer approximation involves writing the wavefunction as a product of nuclear and electronic wavefunctions ($\Phi = \phi_n \phi_e$). All purely nuclear terms are separated from electronic terms, as the nuclear motion occurs on far larger timescales than the electronic motion. Hence we can remove the nuclear kinetic energy term to find the electronic Hamiltonian:

$$\hat{\mathcal{H}}_e = \hat{\mathcal{T}}_e + \hat{\mathcal{U}}_{ee} + \hat{\mathcal{U}}_{ne} + \hat{\mathcal{V}}_{ext}, \tag{2.3a}$$

$$\hat{\mathcal{H}} = \hat{\mathcal{H}}_e + \hat{\mathcal{H}}_n. \tag{2.3b}$$

This defines the electronic energy eigenvalues, E_e, when operating on the electronic wavefunction, ψ_e with fixed nuclear positions:

$$\hat{\mathcal{H}}_e \psi_e = E_e(\{\mathbf{R_N}\})\psi_e, \tag{2.4}$$

where the electronic wavefunction depends on electronic and nuclear positions. The corresponding equation including all interactions is:

$$(\hat{\mathcal{T}}_n + E_e(\{\mathbf{R_N}\}))\psi_n = E\psi_n. \tag{2.5}$$

It can be seen that when nuclear coordinates are allowed to vary (nuclear coordinates denoted by $\mathbf{R_N}$), the electronic energy eigenvalue also varies. The electronic energy eigenvalue acts as a potential in the nuclear equation. The Born-Oppenheimer approximation is used throughout this thesis unless specifically stated otherwise.

2.1.3 Hartree-Fock Theory

One approximation to the TISE for many particles is Hartree-Fock (HF) theory; the principle of which is to assume the wavefunction can be expressed in terms of single electron orbitals [36].

After simplifying the wavefunction using the Born-Oppenheimer approximation, the problem still remains as to how to approximate the (now purely electronic) wavefunction. The simplest way of achieving this, the Hartree method, results in a separable wavefunction of the form:

$$\Psi_i(\mathbf{r_1}, \mathbf{r_2}, ..., \mathbf{r_n}) = \phi_1(\mathbf{r_1})\phi_2(\mathbf{r_2})...\phi_n(\mathbf{r_n}) \tag{2.6}$$

This does not, however, satisfy the antisymmetry principle which necessitates a change of sign when two coordinates are swapped. For two electrons this could be satisfied by:

$$\Psi_i(\mathbf{r_1}, \mathbf{r_2}, ..., \mathbf{r_n}) = \frac{1}{\sqrt{2}}(\phi_1(\mathbf{r_1})\phi_2(\mathbf{r_2}) - \phi_1(\mathbf{r_2})\phi_2(\mathbf{r_1})). \tag{2.7}$$

and can be generalised to n electrons via a Slater determinant:

$$\psi = \frac{1}{\sqrt{n!}} \begin{vmatrix} \phi_1(\mathbf{r_1}) & \phi_2(\mathbf{r_1}) & \dots & \phi_n(\mathbf{r_1}) \\ \phi_1(\mathbf{r_2}) & \phi_2(\mathbf{r_2}) & \dots & \phi_n(\mathbf{r_2}) \\ \vdots & \vdots & \ddots & \vdots \\ \phi_1(\mathbf{r_n}) & \phi_2(\mathbf{r_n}) & \dots & \phi_n(\mathbf{r_n}) \end{vmatrix}. \tag{2.8}$$

This also ensures the wavefunction is zero if two orbitals are the same (e.g setting $\phi_2 = \phi_1$), which elegantly demonstrates the Pauli exclusion principle mathematically. An important point to note here is that, although the exchange interaction is included here, correlation effects will not arise due to the use of a single de-

terminant. Other methods exist that include this effect via the use of multiple determinants [37]. The variational principle can be applied to the wavefunction to determine a set of equations to describe the system - with the choice of ansatz therefore affecting the form of such equations. One consequence of choosing to represent the wavefunction as a single determinant is that these equations represent each electron interacting with the average electron density. This introduces a non-physical self interaction, as each electron also interacts with itself through the average density. The single determinant wavefunction system can be described by:

$$\left(-\frac{1}{2}\nabla_i^2 + \sum_j \int \frac{|\phi_j(\mathbf{r}_j)|^2}{|\mathbf{r}_i - \mathbf{r}_j|} \mathrm{d}\mathbf{r}_j + V_{\text{ext}}(\mathbf{r}_i) - \hat{\mathcal{F}}\right) \phi_i(\mathbf{r}_i) = \epsilon_i \phi_i(\mathbf{r}_i), \tag{2.9}$$

where the final term is written as:

$$\hat{\mathcal{F}}\phi_i(\mathbf{r}_i) = \int \sum_j^{\text{occ.}} \frac{\phi_j^*(\mathbf{r}_j)\,\phi_j(\mathbf{r}_i)}{|\mathbf{r}_i - \mathbf{r}_j|} \phi_i(\mathbf{r}_j)\,\mathrm{d}\mathbf{r_j}. \tag{2.10}$$

The terms in equation 2.9 represent: kinetic energy, Coulomb potential from the average electronic charge density, external potential (including from the ionic potential), and the exchange interaction respectively. The exchange interaction term has no classical analogue and is known as the exchange operator - defined in 2.10. This is non-local in nature, resulting in heavy computational cost to calculate due to the potential depending on both $\mathbf{r_i}$ and $\mathbf{r_j}$, rather than just $\mathbf{r_i}$.

The HF equations can be solved self consistently to give the energy of the system. Self consistency is necessary because the wavefunction appears on both sides of the equation, hence applying the Hamiltonian to a wavefunction will yield an energy multiplied by another wavefunction. The wavefunctions on both sides of the equation must be consistent for a solution to be found, both in the operator on the left hand side and the wavefunction this operates on, but this is not

guaranteed. The self consistent solution must therefore be found by solving with a trial wavefunction, then solving again using the newly generated wavefunction and repeating until the wavefunctions match that of the operator [38].

2.1.4 Hohenberg-Kohn theorems

The Hohenberg-Kohn theorems provide a framework to recast the TISE in terms of the electron density, rather than coordinates of individual electrons. This reduces the complexity of the problem, as the number of coordinates necessary to describe a system of n electrons is reduced from the coordinates of all electrons $(\mathbf{r_1}, \mathbf{r_2}, ..., \mathbf{r_n})$ to just one set of coordinates, $\mathbf{r}$.

Hohenberg and Kohn set out a proof showing the external potential uniquely defines the density of a system [39]. They then extended this to show that the energy of a system is a functional of the density such that:

$$E[n(\mathbf{r})] \equiv F[n(\mathbf{r})] + \int V_{ext}(\mathbf{r}) n(\mathbf{r}) d\mathbf{r}. \tag{2.11}$$

Through the variational principle it can be seen that $E[n(\mathbf{r})]$ will be minimised for the ground state density, hence the ground state energy can be found if the universal functional $F[n(\mathbf{r})]$ is known. Together, the Hohenberg-Kohn theorems provide the fundamental basis for DFT.

2.1.5 Kohn-Sham DFT

The most widely used formalism for DFT is Kohn-Sham DFT. In this formalism, the interacting electron system is replaced by an equivalent fictitious non-interacting system, which produces the same electron density as the real system. This enables a system of non-interacting particle equations to be solved [40]. These equations are considerably simpler to solve than the full interacting equa-

tions and is achieved by using an effective potential, giving the set of equations:

$$\left(-\frac{1}{2}\nabla^2_{\mathbf{r}} + V_{eff}(\mathbf{r})\right)\phi_i(\mathbf{r}) = \epsilon_i\phi_i(\mathbf{r}). \tag{2.12}$$

The effective potential can be split into its constituent parts, such that:

$$V_{eff} = V_H + V_{ext} + V_{xc}, \tag{2.13}$$

where V_H is coulomb repulsion between electrons (referred to as the Hartree potential), V_{ext} is the external potential and V_{xc} is the exchange-correlation energy. The Hartree potential can be written as:

$$V_H(\mathbf{r}) = \int \frac{n(\mathbf{r_i})}{|\mathbf{r_i} - \mathbf{r_j}|} d\mathbf{r_i}. \tag{2.14}$$

The external potential is then defined by the system being studied, reducing the problem to one of approximating the exchange correlation potential. It should be noted that the expression for the 'Hartree potential' integrates the whole charge density, which inevitably includes the charge density from the electron for which the potential is acting upon. This has the effect of ensuring each electron is interacting with itself, introducing an error (called the self interaction error). This has the effect of overestimating electron-electron repulsion, hence can result in nonphysical delocalisation if unaccounted for. The correction for the self interaction is incorporated into the approximation for the exchange-correlation potential and thus the self interaction error should be eliminated if the exchange correlation functional is exact.

2.1.6 Exchange-correlation functionals

The exchange correlation energy must be a functional of the density, however it can have different forms depending upon the assumptions made in forming it [41]. The simplest of these functionals is known as the local density approximation (LDA), and has the form:

$$E_{xc} = \int n(\mathbf{r})\epsilon_{xc}(n(\mathbf{r}))d\mathbf{r}. \tag{2.15}$$

$n(\mathbf{r})$ is the density and ϵ_{xc} is the exchange correlation energy per electron. This is easily calculable, as ϵ_{xc} can be found numerically as the energy per electron in a homogeneous electron gas. As this approximation is based upon a system with homogeneous charge density, the approximation works best if the charge density varies slowly (such as in many solid state systems apart from close to atoms). Nevertheless, the assumption of homogeneity can reduce accuracy in systems with highly inhomogeneous charge density. Another class of functional was proposed to improve upon this, the generalised gradient approximation (GGA), which has the form:

$$E_{xc} = \int n(\mathbf{r})\epsilon_{xc}(n(\mathbf{r}), \nabla n(\mathbf{r}))d\mathbf{r}. \tag{2.16}$$

The GGA takes into account the gradient of the density as well as the density, improving the accuracy for most materials. Many different formulations of this exist, however the Perdew-Burke-Ernzerhof (PBE) version is the most widely used [42]. There also exist a set of functionals, referred to as meta-GGA's, which also take into account the gradient of this gradient and have seen some success in improving the approximation further, however the GGA still dominates most research due to its simplicity combined with reasonable accuracy for many situations.

2.1.7 Hybrid functionals

DFT is known to underestimate the band gap of materials, sometimes even to the extent of predicting semiconductors to be metals. While this is not an inherent property of DFT, the source of this error lies within the approximation of exchange-correlation functionals. The calculation of band gap requires energies of the system with differing numbers of electrons to be calculated. The exact functional must have discontinuities in its derivative when an electron is added or removed from the system, as fractional particles do not exist. Therefore the effect of adding an electron should be a discrete change in exchange-correlation energy. In contrast, any local or semi-local approximation to the functional produces a continuous derivative with respect to changing numbers of electrons, causing an inherent error within these functionals. This results in the self interaction error not being fully cancelled, which in turn increases the energy of occupied states. As the energy error is different for different numbers of electrons, and the calculation of band gap relies on energy differences when an extra electron is added, this results in a reduced band gap prediction. Another way to calculate the band gap is the difference between highest occupied state and lowest unoccupied state. In such a case the energy of occupied states are overestimated, while unoccupied states do not contribute towards the density so do not have this self interaction error, thus reducing the band gap prediction.

Hybrid functionals use the idea of coupling standard functionals with some Fock exchange to improve the model. The idea is that where a local or semi-local functional underestimates the band gap, HF theory overestimates it. The inclusion, therefore, of a perfectly tuned amount of Fock exchange should cause these errors to cancel each other, as illustrated in Fig. 2.1.

The simplest method for doing this is to mix a set fraction of a standard DFT functional with a set fraction of Fock exchange. In the case of choosing PBE as

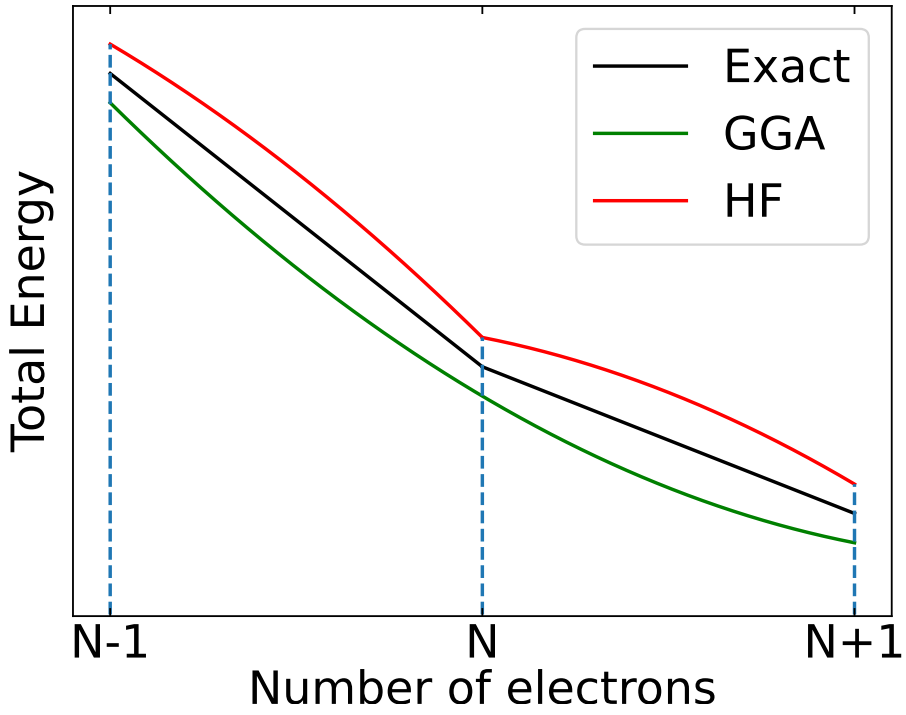

Figure 2.1: Illustration of the systematic errors in energies predicted by HF and GGA approximations with respect to changing number of electrons.

this standard functional, the total exchange-correlation energy is given by:

$$E_{\mathrm{xc}}^{\mathrm{PBE}\alpha} = \alpha E_{\mathrm{x}}^{\mathrm{HF}} + (1-\alpha)E_{\mathrm{x}}^{\mathrm{PBE}} + E_{\mathrm{c}}^{\mathrm{PBE}}. \tag{2.17}$$

The energies are here split into exchange and correlation energies (x and c subscript respectively), with the total exchange given by a mixing of Fock exchange and PBE exchange, with correlation energy purely coming from PBE. The PBE0 functional is an example of this, with α taken as $\frac{1}{4}$ - a value determined by theoretical derivation by Perdew, Burke and Ernzerhof [43]. This dependence on α could be tested for each material and tuned to find the optimal value, however this would reduce the predictive power of the functional as this value would always need to be determined empirically on a material to material basis. This

would reduce the usefulness for novel materials with little to no empirical data to tune to.

The Heyd-Scuseria-Ernzerhof (HSE06) functional builds on this principle by adding the concept of range separation [44]. Essentially, the $\frac{1}{r}$ decaying interaction in the exchange correlation functional is rewritten as:

$$\frac{1}{r} \approx \frac{\mathbf{erfc}(\omega r)}{r} + \frac{\mathbf{erf}(\omega r)}{r}. \tag{2.18}$$

These terms represent the short and long range contributions respectively, where ω is a parameter that defines the balance between short and long range interactions to be considered in the system, as illustrated in Fig. 2.2.

Applying this to the exchange interaction of the general hybrid functional (PBEα) gives:

$$E_x^{HSE} = \alpha E_x^{HF,SR} + (1-\alpha)E_x^{PBE,SR} + \alpha E_x^{HF,LR} + (1-\alpha)E_x^{PBE,LR}. \tag{2.19}$$

The long range HF and PBE exchange energies are roughly equal for reasonable values of ω and contribute very little to the energy, thus this can be written more simply as:

$$E_x^{HSE} = \alpha E_x^{HF,SR} + (1-\alpha)E_x^{PBE,SR} + E_x^{PBE,LR} \tag{2.20}$$

The long range HF exchange has thus been removed from the equation, reducing the computational cost. The HSE06 functional is used extensively in this thesis, and is defined for the case of $\omega = 0.2$ Å^{-1} and $\alpha = 0.25$. These values were found by fitting predictions of the functional to extensive data from literature, averaged over a range of materials.

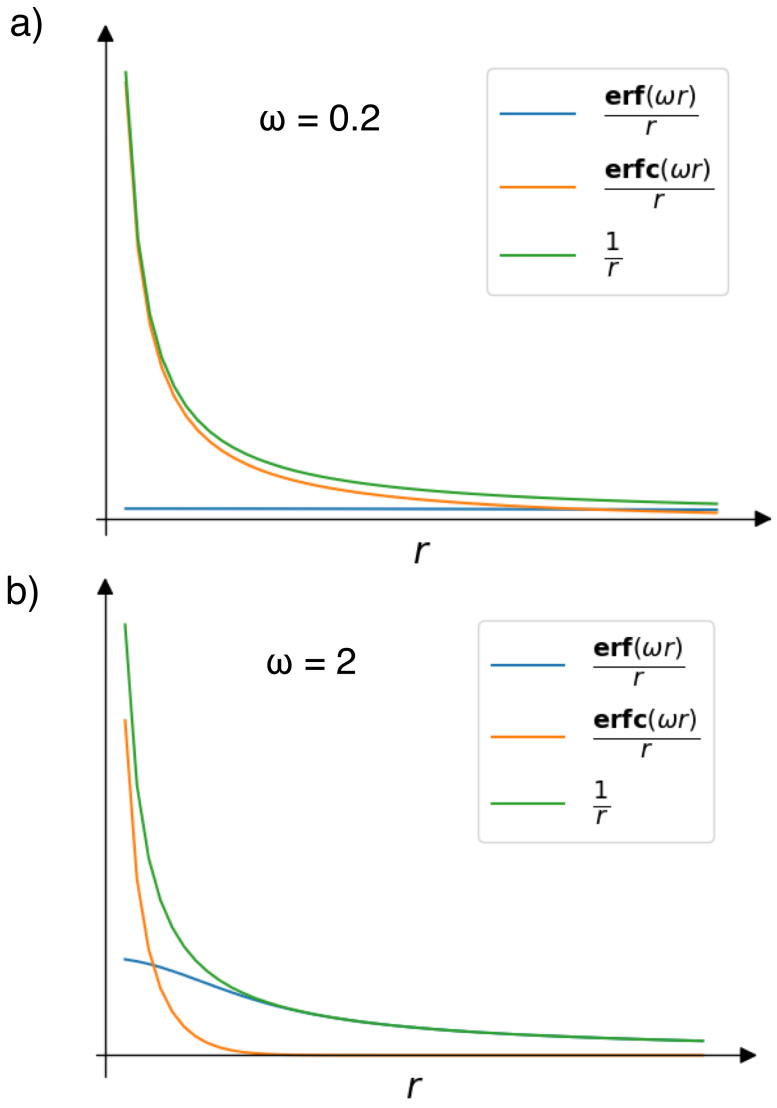

Figure 2.2: The form of a range separated potential using the error and complementary error functions for a) $\omega = 0.2$ Å^{-1} and b) $\omega = 2$ Å^{-1}, illustrating that a higher ω value increases long range contribution and reduces short range contribution to the $\frac{1}{r}$ potential.

2.1.8 Van-der-Waals Corrections

Van-der-Waals forces are dependent upon correlation effects between electrons, however longer range effects are generally ignored by the DFT approach due to the assumption of local dependence in the exchange-correlation functional [45]. These

energy contributions are often negligible, so can safely be omitted. In the absence (or near absence) of other forces they can however have non-negligible effects. One such category of materials are the two dimensional materials described in this thesis, often called 'van der Waals materials' because the inter-layer distances are governed by the vdW interaction. In such materials, an energy correction must be introduced to include such interactions. These interactions can be considered to decay as $-\frac{C_6}{r^6}$. Higher order terms also contribute e.g ($\frac{C_8}{r^8}$, $\frac{C_{10}}{r^{10}}$) but for large distances the first order approximation is sufficient [46]. The terms C_i represent functional-dependent proportionality constants for each $-\frac{1}{r^i}$ term.

The energy correction can be introduced non self-consistently to the DFT energy by simple addition:

$$E_{tot} = E_{dft} + E_{vdw}, \tag{2.21}$$

and the energy correction can be written as a sum of pair-wise interactions:

$$E_{vdw} = \sum_{i>j} f(r_{ij}) \frac{C_6^{ij}}{r_{ij}}, \tag{2.22}$$

where i and j label each atomic site and $f(r_{ij})$ is a damping function to remove the divergent behaviour of the r_{ij}^{-6} function for small distances. Clearly to make use of this approximation, the C_6^{ij} constants must be defined. One method is to calculate these from the charge density (called DFT+vdW methods), however this thesis uses the DFT+D method [47, 48]. This involves calculating the dispersion coefficients for each atom via ionisation potentials and polarizabilities found from computational calculations (C_6^i, C_6^j) and taking the geometric mean ($C_6^{ij} = \sqrt{C_6^i C_6^j}$). Other methods exist but are not discussed here.

2.1.9 Periodic boundary conditions

Individual molecules/few molecule systems have a small enough number of electrons to be modelled using DFT in a reasonable timeframe, which can yield reasonable properties for gases. Conversely, the number of electrons in a model of a solid material can be very large, with non-negligible interactions between atoms. This results in prohibitively expensive calculations if all electrons were to be considered separately. Fortunately, many solids arrange in crystal form, with a periodic arrangement of atoms. The crystal can then be viewed as an infinitely repeating unit (a unit cell), an approximation known as periodic boundary conditions [49].

Mathematically, this can be described by defining a set of basis vectors to describe the unit cell:

$$\begin{aligned} \mathbf{a} &= a_1\hat{\mathbf{x}} + a_2\hat{\mathbf{y}} + a_3\hat{\mathbf{z}} \\ \mathbf{b} &= b_1\hat{\mathbf{x}} + b_2\hat{\mathbf{y}} + b_3\hat{\mathbf{z}} \\ \mathbf{c} &= c_1\hat{\mathbf{x}} + c_2\hat{\mathbf{y}} + c_3\hat{\mathbf{z}} \end{aligned} \quad . \tag{2.23}$$

If a point within the unit cell is translated by an integer number of these lattice vectors (i.e a translation of $\mathbf{R} = n_1\mathbf{a}+n_2\mathbf{b}+n_3\mathbf{c}$), the same point in a neighboring unit cell will result. As we are considering an infinite crystal, these points are identical. Only 14 sets of distinct periodic lattice vectors are possible, known as the Bravais lattices [50]. While a Bravais lattice defines the periodicity of a crystal, the locations of atoms within the unit cell must also be defined to fully define crystal structure. The set of these atomic positions is known as the atomic basis.

A second set of lattice vectors can be defined corresponding to the Fourier transform of real space - known as reciprocal space. The same periodic condition

also applies to these vectors, with the definition of such vectors:

$$\begin{aligned} \mathbf{a}* &= 2\pi \frac{\mathbf{b}\times\mathbf{c}}{\mathbf{a}\cdot(\mathbf{b}\times\mathbf{c})} \\ \mathbf{b}* &= 2\pi \frac{\mathbf{c}\times\mathbf{a}}{\mathbf{a}\cdot(\mathbf{b}\times\mathbf{c})} \\ \mathbf{c}* &= 2\pi \frac{\mathbf{a}\times\mathbf{b}}{\mathbf{a}\cdot(\mathbf{b}\times\mathbf{c})} \end{aligned} \quad . \tag{2.24}$$

An integer number of translations of these vectors (i.e a translation of $\mathbf{G} = n_1\mathbf{a}* + n_2\mathbf{b}* + n_3\mathbf{c}*$) will again result in an identical point.

2.1.10 Bloch's theorem

Bloch's theorem describes the wave function in an infinite crystal as a plane wave modulated by a periodic function such that:

$$\psi_{n,\mathbf{k}}(\mathbf{r}) = u_{n,\mathbf{k}}(\mathbf{r})\mathbf{e}^{i\mathbf{k}\cdot\mathbf{r}}, \tag{2.25}$$

where $u_{n,\mathbf{k}}(\mathbf{r})$ is a periodic function with the same periodicity as the crystal, with n and $\mathbf{k}$ being the band index and wave vector in the reciprocal lattice basis respectively. The periodicity in space means that $\psi_{n,\mathbf{k}}(\mathbf{r}) = \psi_{n,\mathbf{k}}(\mathbf{r}+\mathbf{R})$, while the periodicity in reciprocal space similarly results in $\psi_{n,\mathbf{k}}(\mathbf{r}) = \psi_{n,\mathbf{k}+\mathbf{G}}(\mathbf{r})$. Consequently, if a solution is found for a single unit cell, and a single real space unit cell and a single reciprocal space unit cell (called the Brillouin zone), the system is fully solved as neighboring cells contain no new information.

The Kohn-Sham equations thus become:

$$\left(-\frac{1}{2}(\nabla + i\mathbf{k})^2 + V_{\text{eff}}(\mathbf{r})\right) u_{n,\mathbf{k}}(\mathbf{r}) = \epsilon_{n,\mathbf{k}} u_{n,\mathbf{k}}(\mathbf{r}) \tag{2.26}$$

where $V_{\text{eff}}(\mathbf{r})$ is the Kohn-Sham potential (Eq. 2.13). Clearly the eigenvalues, $\epsilon_{n,\mathbf{k}}$, vary with $\mathbf{k}$ - opening up the possibility of dispersive bands contrary to the

non-dispersive states seen in non-periodic systems.

2.2 Photoluminescence in 2D materials

2.2.1 Absorption and Emission

Fig. 2.3 illustrates a simple two level excitation and deexcitation in a configuration space. When a photon is incident on a system it can be absorbed by an electron to form an excited electron with increased energy, without changing the configuration of atoms. The atomic structure will then relax to the lowest energy configuration of the excited state via emission of phonons. It is energetically favourable for the electron to minimise its energy, thus can emit a photon of this energy to return back to the ground state (or a phonon in the case of non-radiative recombination). In such a system, the energy of the incident photon would have to be that of the difference between energy levels, with the emitted photon also this energy. In an undoped semiconductor, the highest occupied energy level is at the top of the valence band, thus for an incident photon to be absorbed and promote an electron directly from the VBM to the CBM it must have the same energy as the band gap in this simple model. In reality, energy levels also exist above the band gap which electrons can be excited into, so it is enough for the incident photon energy to be above that of the band gap. If an electron is excited above the CBM further energy transitions and combinations of transitions are possible to return the electron to the VBM. This results in a spreading in the possible energies of emitted photons. The band gap energy is the most probable energy transition, thus corresponds to the peak of the PL spectra (a plot of emitted light intensity as a function of photon energy or wavelength).

This is, of course, still a simple model, as bands will also vary in energy with position in k space due to dispersion effects. This also has the effect of widening

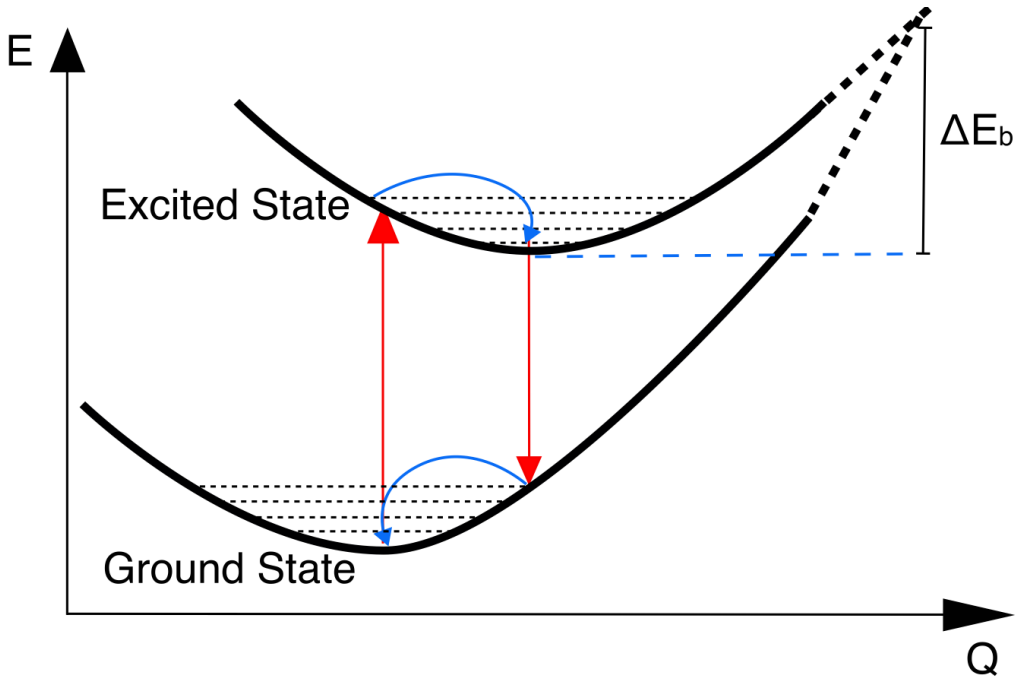

Figure 2.3: Energies of the ground state and an excited state as a function of configuration coordinate, Q. Optical transitions between states are shown as red arrows and phonon mediated transitions are shown with blue arrows. Dashed lines indicate phonon eigenvalues, and ΔE_b represents the energy barrier to non-radiative transition to the ground state.

the PL curve, as a wider array of energies can give rise to transitions - although the band gap energy will still be coincident with the PL peak as the lowest energy transition from CBM to VBM (assuming small Stokes shift). A photon is also not necessarily emitted for every transition, as non-radiative transitions can exist, producing a lattice vibration (phonon) via which the necessary energy is released. The energy barrier to such a process is shown in Fig. 2.3 as ΔE_b, the energy difference between the energy minimum in the excited state and the crossing point of the excited state and ground state energy curves. By moving along such curves to de-excite an electron, the process can be achieved using purely phonons, hence resulting in a non-radiative transition [51]. Non-radiative transitions are usually defect-mediated, as defects cause a change in configuration coordinate, thus reducing ΔE_b. A defect can also form a state within the band gap, which

electrons and holes can fall into - with the trapping probability of an electron and hole simultaneously being maximized by a defect state in the centre of the band gap. Fig. 2.3 can also be used to explain Stokes shift: a process causing absorption and emission peaks to be non-coincident. As a phonon is emitted to relax the structure within the excited state, the energy difference between excited and ground states is reduced, thus reducing the energy of an emitted photon during recombination to reach the ground state - thus the absorbed photon can be of different energy to an emitted photon.

As the energy of states can vary as a function of **k** within reciprocal space, the VBM and CBM do not necessarily lie at the same point in k space. If such a transition is at one point in k space, the transition can be achieved via a photon. However, in the case of the VBM and CBM lying at different points in reciprocal space, an indirect band gap is formed. As a photon carries energy but little momentum, an indirect transition requires participation of phonons to conserve momentum, as shown in Fig. 2.4. This reduces the probability of such a transition compared to a direct transition due to the increased number of events necessary.

Within 2D materials, optical absorption is often small, as the reduced dimensionality means any incident light has the potential to interact with only a thin layer of material, while the majority of incident light passes through the sample without interaction. This exacerbates the need for a direct band gap to maximise the number of photons produced from this limited number of interactions by reducing non-radiative events. Even with a direct band gap, emission from such materials can be weak, sometimes requiring seconds of integration time to achieve a reasonable signal to noise ratio in photoluminescence measurements [52]. Monolayer photon absorption efficiency has been reported at between 2-12%, however in some cases this has been improved to 20-30% via the use of cavities [53].

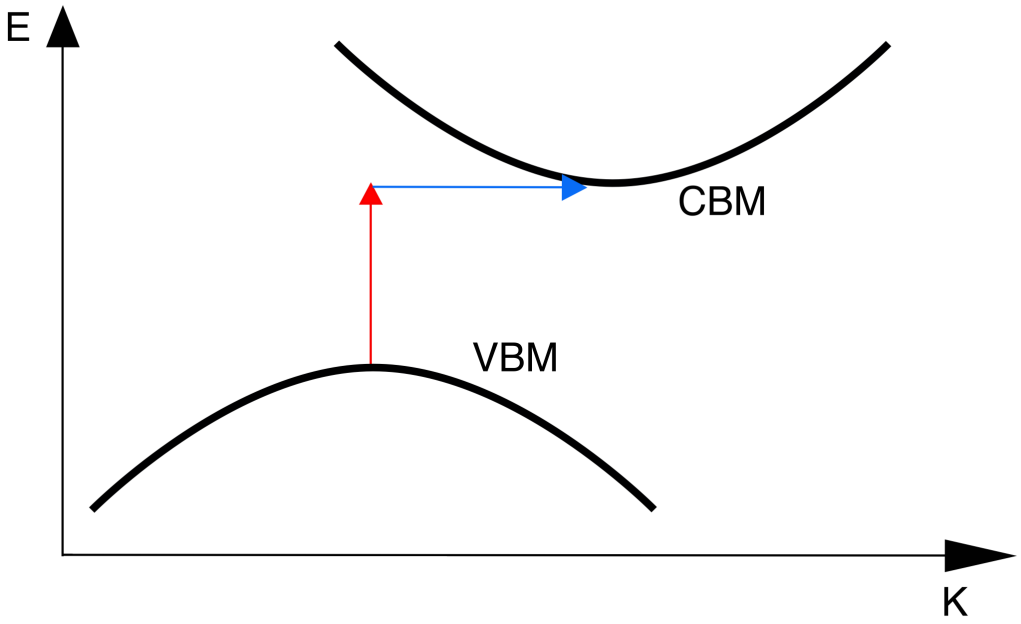

Figure 2.4: Diagram of an indirect band gap, showing a photon (red arrow) and phonon (blue arrow) being emitted to facilitate such a transition.

2.2.2 Excitonic effects

Excitons are quasiparticles comprised of an electron-hole pair bound by the coloumb interaction between the negatively charged electron and positively charged hole. This interaction stabilises the particle, causing the exciton to have lower energy than its constituent particles; this energy difference is known as the exciton binding energy. Typically in semiconductors, the large dielectric constant screens the electronic charges, thus resulting in weakly bound excitons, typically with 1-10 meV binding energy. Germanium and silicon are typical examples, with exciton binding energies of 2.7 meV and 10 meV respectively [54]. In contrast, 2D materials often have a reduced dielectric constant and thus reduced screening due to confinement of electrons within a plane [55]. This can result in larger exciton binding energies on the order of 100s of meVs, although the exact values depend on substrate. For example MoS_2 and WSe_2 both have exciton binding energies of 240 meV on a sapphire substrate, but these values reduce to 90 meV and 140

meV for MoS_2 and WSe_2 respectively on a gold substrate [56]. The substrate effect is exacerbated for 2D materials due to the reduced dimensionality resulting in field lines from excitons extending outside of the material bounds, thus interacting with the neighboring dielectric environment. Unlike the relatively small energies involved in bulk materials, these larger exciton binding energies can often result in effects larger than thermal motion of such particles, causing them to be present in the PL curve - visible as a shift in the optical band gap relative to the calculated band gap without inclusion of excitonic effects - with a difference of the exciton binding energy. This leads to an inherent overestimation in the band gap in an otherwise ideal DFT calculation (with a perfectly predicted atomic structure).

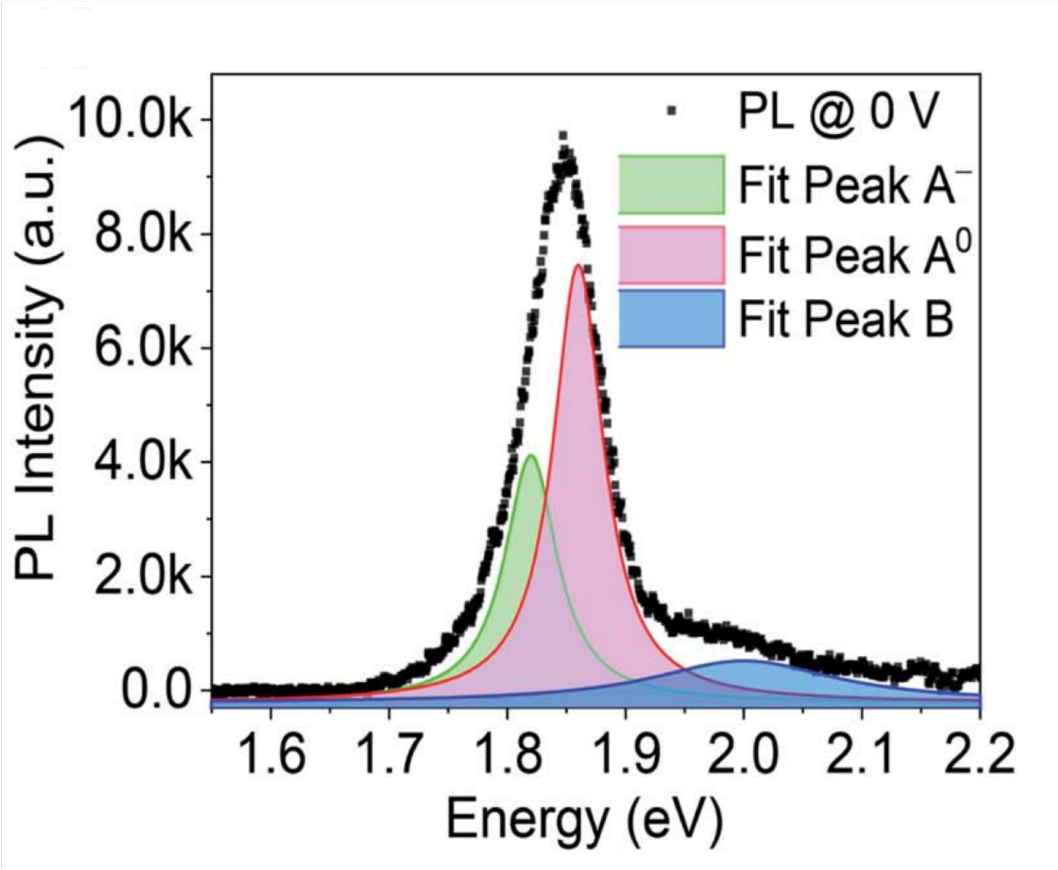

Figure 2.5: Example of MoS_2 PL curve decomposed into 3 peaks: A^0 exciton peak, B exciton peak, and A^- trion peak. Figure reproduced from [57] under a creative commons license.

Different types of excitons can exist in a material, leading to different peaks presenting in the PL spectrum. In the example of TMDs, three excitons usually exist: labelled the A and B excitons, plus the A^- trion. The A exciton is the simplest: formed via interaction between an electron at the CBM and a hole at the VBM. Spin splitting in the valence band also makes the B exciton possible. The B exciton is similar to the A exciton except that the hole originates from the lower energy spin-split valence band. The A^- trion is then formed from the interaction of an A exciton with an electron in the CBM. These clearly have different recombination energies and thus cause emission of photons of different energies during their respective recombination processes, producing different signals in a PL spectrum. This results in the PL spectra for TMDs being a convolution of the peaks resulting from each of these recombination processes [58]. These peaks fitted to a WS_2 PL curve are shown in Fig. 2.5. The exciton recombination energy levels are illustrated in Fig. 2.6.

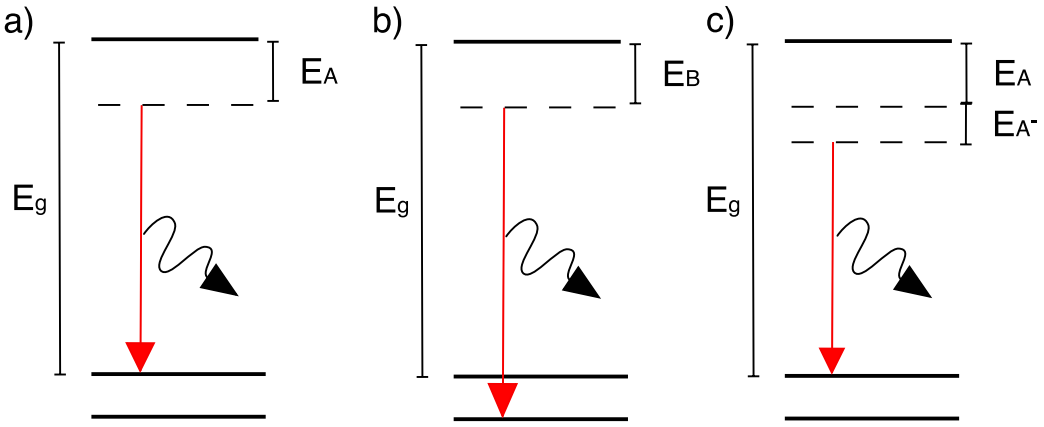

Figure 2.6: Energy level diagrams illustrating PL of the a) A exciton PL, b) B exciton and c) A^- trion. Transitions are shown, with E_g representing the single particle band gap, E_A the A exciton binding energy, E_B the B exciton binding energy and E_{A-} the A^- binding energy. Recombinations are shown in red and dashed lines represent exciton energy levels.

Excitons can be further classified as dark, bright and trapped, with the recombination mechanisms and associated energy levels shown in Fig. 2.7.

Fig. 2.8 illustrates the spin-valley effect, which causes bright and dark excitons to emerge. Electrons in the conduction band have a spin of $\pm 1/2$, however the spin-split valence band results in holes of $+3/2$ and $-3/2$ for the spin up and down states respectively. An A or B exciton can therefore have a spin of ± 1 or ± 2 - but only spins of ± 1 will couple to a photon. Excitons that do not couple to a photon are labelled dark excitons due to their suppression in the PL spectrum. Due to the lack of inversion symmetry in hexagonal 2D materials, two different kinds of splitting can exist at $\pm\mathbf{K}$, with the $+\mathbf{K}$ valleys shown in Fig. 2.8. The valleys at the $+\mathbf{K}$ point correspond to the up and down spin states in the valence band swapping energies relative to each other. The result of this is oppositely circularly polarised light couples to the bright excitons for the different K valleys.

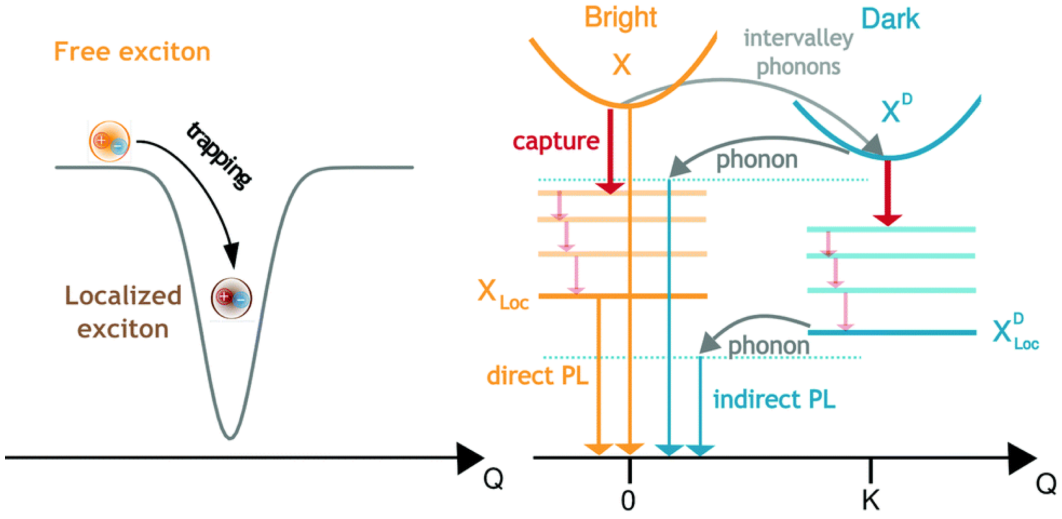

Figure 2.7: Energy level diagram showing phonon and photon transitions and associated energy levels of bright and dark excitons, with their associated localized states. Reproduced from [59] under a creative commons license.

The trapped exciton case can be either bright or dark, referring to a localised exciton due to trapping by a potential well. Such trapped excitons can be trapped due to defects or by 'self trapping', which is caused by strong coupling to phonons - heavily deforming the lattice close to the exciton and increasing its barrier to

movement within the lattice [59].

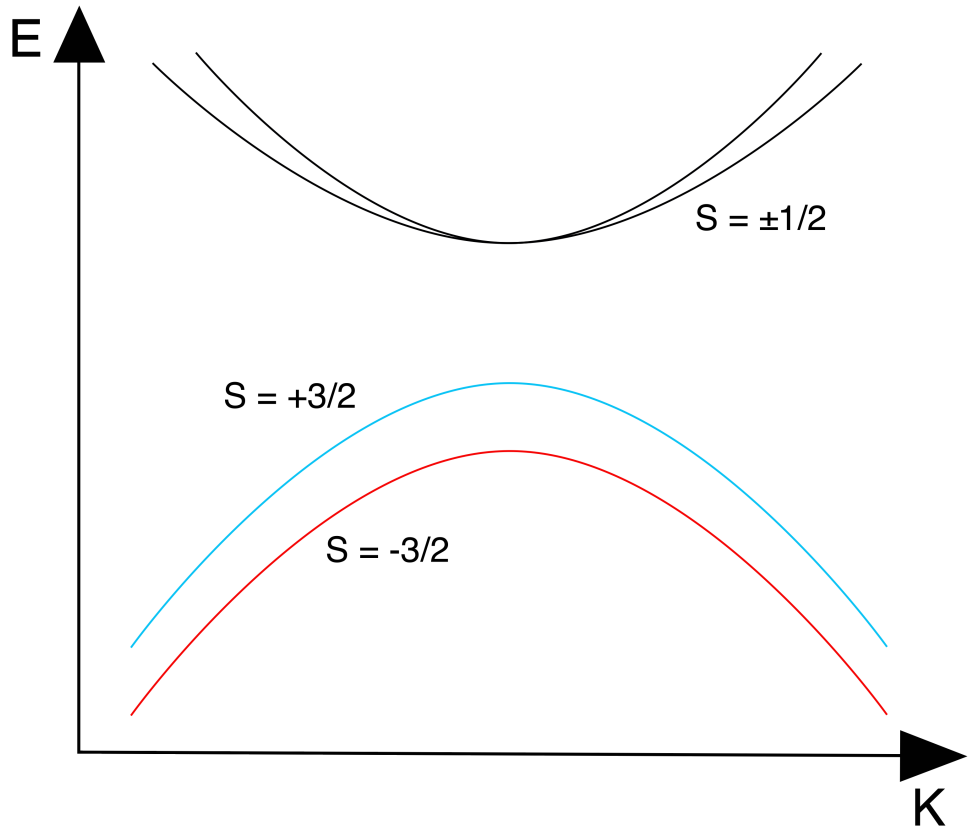

Figure 2.8: Spin valley effect illustration, showing the K valley. Spins for holes/electrons in the valence and conduction bands respectively are shown. Spin up and down energy levels indicated by blue and red arrows respectively.

2.2.3 Layer dependence

The PL in TMDs can often increase when the number of layers is reduced. Due to the layered structure, outer atoms in a layer can more easily interact with neighboring layers, hence their electronic structure can change when these interactions are removed by removing the neighbouring layers. This is not the case for the atoms sandwiched within the layer, thus their electronic structure changes far less when layer number is reduced. These different atoms can affect states at different points in reciprocal space, thus a change in layer number can cause a

shift in band gap not only in magnitude but also in position in reciprocal space; a result of this can be a change from direct to indirect band gap. This effect is shown for the example of MoS_2 in Fig. 2.9, where the states at the Γ point change with layer number, while the states at the K point remain unchanged, resulting in a shift in reciprocal space position of the lowest energy band transition. The magnitude of the optical band gap varies non-linearly from ∼1.9 eV to ∼1.3 eV as the number of layers is increased from monolayer to a bulk crystal [13].

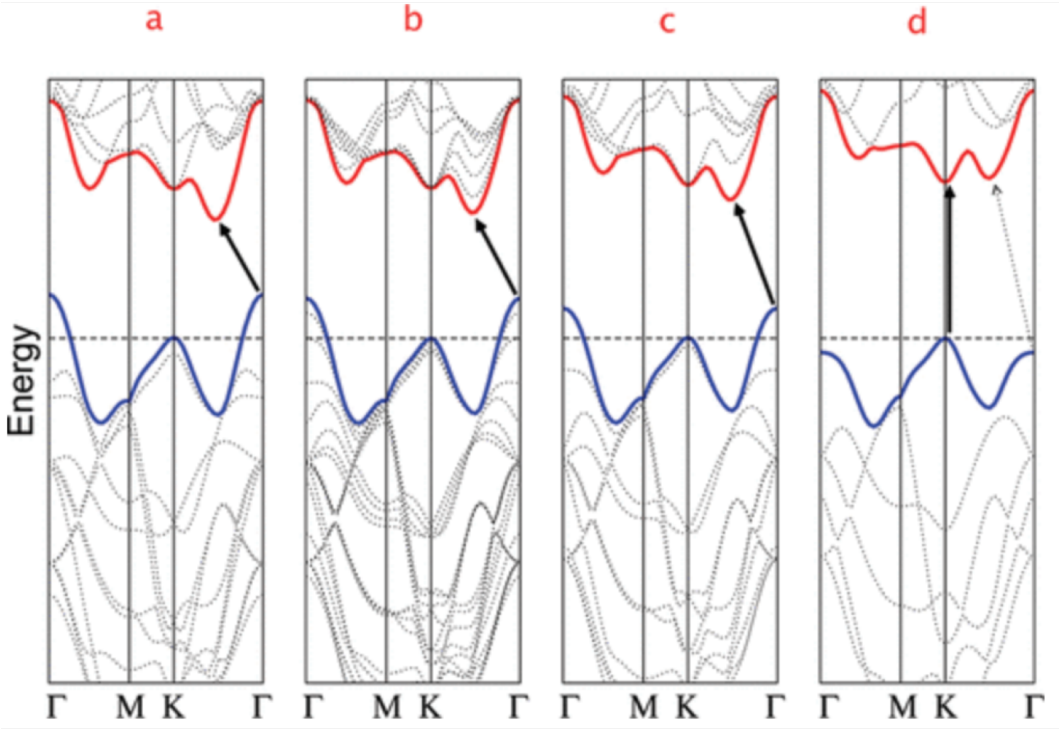

Figure 2.9: Evolution of band structure with varying number of layers for MoS_2, including a) bulk, b) 4 layer, c) bilayer, d) monolayer systems. Lowest energy transitions are indicated by a solid black arrow. The dashed arrow in d) represents the indirect transition for comparison, although this is not the lowest energy transition. Reproduced with permission from [60].

An electron transition across a direct band gap in reciprocal space involves a change in energy but not momentum, thus can be achieved by photon absorption only. However for an indirect band gap a momentum change is also required, which must also involve a phonon. The requirement for a phonon to also be

involved decreases the probability of a transition, hence results in a lower PL intensity than a direct transition. Direct band gaps are, therefore, preferable for many applications, especially for any photonic applications.

2.2.4 Substrate effect

Due to their 2D nature, vdW materials generally need to be deposited on a substrate to be useful in devices. Introduction of a substrate has the effect of changing the dielectric environment, which in turn can influence the way carriers behave, changing both the electronic and optical properties of such systems (dielectric screening). On top of this, the interface can introduce strain effects and charge traps, which also influences these properties. In TMDs this is apparent in the PL curve, which has a far lower intensity when using a substrate compared to a suspended flake [61]. The intensity also similarly varies between substrates, as shown in Fig. 2.10. A small shift in the PL peak can also be seen between substrates, which could be caused by substrate induced doping effects [62].

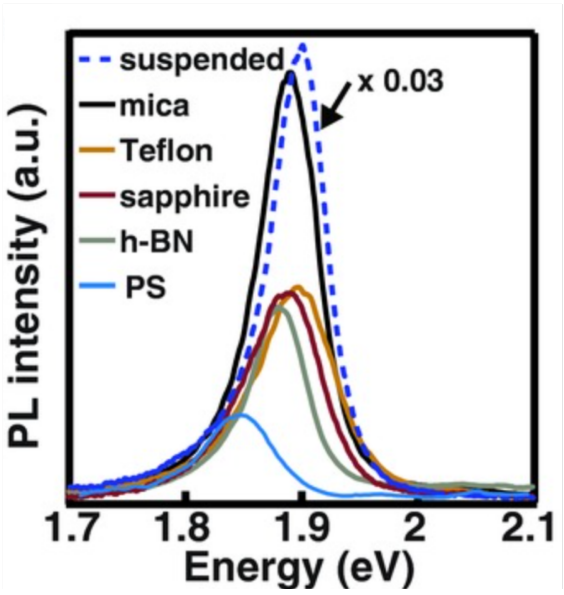

Figure 2.10: Photoluminescence curve from MoS_2 deposited on different substrates, with suspended MoS_2 PL curve also included. Substrates included are: mica, teflon, sapphire, polystyrene (PS). Reproduced with permission from [62].

2.3 Summary

The theory set out in this chapter constitutes the majority of required background knowledge required for the rest of the thesis, with some assumed knowledge. The first half of the chapter sets out the background and motivation for DFT simulations used throughout the thesis, while the second half of the chapter discusses the understanding of physical phenomena necessary to understand both DFT and photoluminescence study results in the context of 2D materials.

Chapter 3

Methods

3.1 Introduction

Further to the theory and background discussed in the previous chapter, further discussion of the specific methods used within this thesis is necessary. The first half of this chapter discusses such methods and approximations used within the context of DFT calculations. This is followed by outlining the specific experimental techniques required for the photoluminescence studies described within the thesis.

3.2 Computational implementation of DFT

3.2.1 Brillouin zone sampling

The calculation of many properties, for example the charge density of the system, involves summing the contributions from all electrons, however the eigenvalues and wavefunctions of the Kohn-Sham equations (equation 2.26) depend on $\mathbf{k}$. To treat this properly, contributions from all values of $\mathbf{k}$ must be taken into account, hence an integration over $\mathbf{k}$ must be undertaken. Due to Bloch's theorem, this

integration can be limited to include only **k** values that lie within the Brillouin zone because no new information is contained outside this zone. An example is the expression for charge density:

$$\rho(\mathbf{r}) = \frac{\Omega}{(2\pi)^3} \int_{\mathrm{BZ}} \rho_{\mathbf{k}}(\mathbf{r}) d\mathbf{k} \tag{3.1a}$$

$$\rho_{\mathbf{k}}(\mathbf{r}) = \sum_{i}^{\mathrm{occ}} \psi^{\star}_{n,\mathbf{k}}(\mathbf{r}) \psi_{n,\mathbf{k}}(\mathbf{r}), \tag{3.1b}$$

where Ω is the unit cell volume. Other properties, such as total energy of the system, involve similar integrals. The integral in equation 3.1 still involves an infinite number of **k** points, but can be approximated to a sum over a finite number of **k** points to ensure this is numerically solvable. The number of **k** points necessary to sample in this sum can be reduced at the expense of accuracy, however many systems require minimal **k** points because the wavefunction, $u_{n,\mathbf{k}}$, depends weakly on **k**. This is often the case for semiconductors, however it is not generally the case. For example in metals a large number of **k** points are often required due to the strong **k** dependence of $u_{n,\mathbf{k}}$. Calculations can be undertaken with different numbers of **k** points to determine the minimum number of **k** points to achieve a converged property. For example in an energy calculation, energy would be calculated at a variety of **k** point sampling densities, with energy gradually converging to a stable value above a certain level of **k** sampling.

A Monkhorst-Pack grid is used to sample k space within this thesis - a grid regularly spaced in reciprocal space. As many materials investigated in this work have a hexagonal structure, the grid must be shifted to ensure it is centred on the Gamma point: $\mathbf{k} = (0, 0, 0)$ - in order to fully capture the symmetry of the unit cell.

3.2.2 Basis sets

A linear combination of functions can be used to approximate the wavefunction:

$$\psi_i(\mathbf{r}) = \sum_b C_{ib}\phi_b(\mathbf{r}), \tag{3.2}$$

where C_{ib} are the coefficients for specific functions, ϕ_b. The form of the functions, ϕ_b, must be known to solve the Kohn-Sham equations (equation 2.26), a number of different options for which are possible. The set of such functions is called the basis set and in this work plane wave basis sets are discussed, as implemented in the Vienna *ab initio* simulation package (VASP) code.

The choice of functions in the case of the plane wave basis set corresponds to representing the wavefunction as a Fourier series:

$$u_{n,\mathbf{k}}(\mathbf{r}) = \frac{1}{\Omega^{1/2}} \sum_{|\mathbf{G}|<G_C} C_{n,\mathbf{k}}(\mathbf{G}) e^{i\mathbf{G}\cdot\mathbf{r}} \tag{3.3}$$

where Ω is the unit cell volume, $C_{n,\mathbf{k}}(\mathbf{G})$ are the coefficients for each term, $\mathbf{G}$ is an integer multiple of reciprocal lattice vectors and G_C is a cutoff defined to truncate the series. As each term in this series represents a wave, the cutoff is usually defined as the energy, E_C of the corresponding term:

$$E_C = \frac{\hbar^2}{2m} G_C^2. \tag{3.4}$$

3.2.3 Pseudopotentials

Core electrons exhibit minimal influence on properties close to the Fermi energy thus can, in many situations, be removed from the calculation. Removal of these electrons from the calculation can have an impact on the calculation expense, as less bands must be considered, but also by reducing the number of plane waves

necessary to describe the wavefunction. This is because the wavefunction tends to vary rapidly near to the nucleus, requiring a large number of plane waves to fully describe. Pseudopotentials remove these electrons from the calculation by smoothing the potential within a certain cutoff radius from the nucleus, while maintaining the same potential outside this radius to ensure outer electrons are not changed.

3.2.4 Projector augmented waves

Through the use of pseudopotentials, information is lost from electrons near the nucleus to enable representation with fewer plane waves. The projector augmented wave (PAW) method attempts to remedy this by representing the potential within the cutoff radius using a radial basis set, which requires less basis functions to represent the oscillating features of the wavefunction near the nucleus than using a plane wave basis. This is done by expanding the all electron wavefunction, $\psi_n(\mathbf{r})$:

$$\psi_n(\mathbf{r}) = \tilde{\psi}_n(\mathbf{r}) + \sum_a \sum_v \left(\phi_v^a(\mathbf{r}) - \tilde{\phi}_v^a(\mathbf{r})\right) \left\langle \tilde{p}_v^a \mid \tilde{\psi}_n \right\rangle \tag{3.5}$$

Where $\phi_v^a(\mathbf{r})$ and $\tilde{\phi}_v^a(\mathbf{r})$ are the all-electron and 'smooth function' basis sets respectively, and $\tilde{p}_v^a$ are the smooth projector functions. Qualitatively this has the effect of removing the pseudopotential within the cutoff radius, then adding the all-electron potential within this range using the radial basis.

3.2.5 Geometry optimisation

As discussed in section 2.1.2, in the Born-Oppenheimer approximation the nuclear potential is fixed due to the separation of nuclear and electronic wavefunctions. In practice, the exact atomic positions are not known and must be determined

separately. In each electronic minimization, the forces on each atom j can be calculated from the energy differential with respect to positions of each atom $\mathbf{R_j}$ (the Hellmann-Feynmann theorem [63]):

$$\mathbf{F}_j = -\frac{\partial E}{\partial \mathbf{R}_j} = \left\langle \Psi_0 \left| \frac{\partial \hat{\mathcal{H}}}{\partial \mathbf{R}_j} \right| \Psi_0 \right\rangle \tag{3.6}$$

If these forces are zero, the atoms are in their optimal positions - which we can achieve by calculating these forces, moving the atomic positions closer to the minimum, performing the electronic minimization and repeating until the forces are zero (within a certain tolerance). There exist several algorithms to update the atomic positions in each step. In this work both the conjugate gradient algorithm [64] and quasi-Newton algorithm [65] are used, as the former is robust but costly (often requiring many steps to reach the minimum), while the latter is quick to find a minimum but is only robust near the minimum. The stress tensor can also be calculated separately to the forces if the cell volume is not required to be constant, which can be similarly used to minimize lattice parameters.

3.3 Experimental Techniques

3.3.1 Mechanical exfoliation

Exfoliation is a well-known technique within the field of vdW materials which enables samples with low numbers of layers to be fabricated, often known as the scotch tape method. The technique requires a flake of bulk material to be stuck to adhesive tape, to which a clean piece of tape is adhered and slowly removed. The second tape then has a reduced number of layers of material adhered to it. The process is repeated to further reduce down to the desired number of layers. This is then adhered to polydimethylsiloxane (PDMS) (usually

$\sim$1 x 1 x 0.1 cm^3) and rapidly removed to transfer flakes. It must be noted that the process is not easily controlled, resulting in areas of both thin and bulk-like material, often in close proximity. An example of an exfoliated flake is shown in Fig. 3.1, with the monolayer area labelled and shown to be only a small portion of the flake. Optical microscopy is therefore used to identify visually which areas contain the desired flake thickness through contrast differences. The number of layers can be determined initially via optical contrast, and confirmed via PL due to the variation in peak emission wavelength with number of layers. An atomic force microscope (AFM) can also be used to further confirm layer number, although this method is used sparingly as the tip-sample interaction can sometimes cause sample damage. As the scale of the image suggests, it is typical to achieve monolayer areas of a few microns as a maximum with larger scale flakes only possible using other methods such as chemical vapour deposition (CVD) or molecular beam epitaxy (MBE) [66]. The main advantage of exfoliation is its simplicity, making it ideal for experiments but unsuitable for larger scale manufacturing applications due to the lack of repeatability and limited flake size. Wafer-scale growth techniques applied to 2D materials are still in their infancy, often achieving low quality flakes compared to exfoliation - which is the current state of the art for high quality flakes. Limiting defect growth in such technologies remains a challenge, while growth substrate choice is also limited in order to reduce lattice mismatch to prevent dislocations and strained areas from forming during the growth process although substrate choice is not an issue for CVD [66].

3.3.2 Substrate preparation

Prior to any transfer onto Si/SiO_2 substrates, substrates must be cleaned to minimise interactions with unknown contaminations on the surface. Such interac-

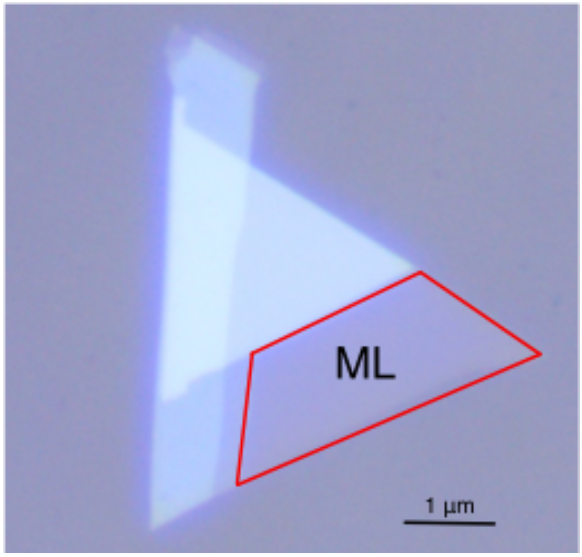

Figure 3.1: Example of exfoliated WS_2 flake viewed in an optical microscope using a 20x objective, with monolayer area highlighted and scale bar (bottom right).

tions could lead to reduced adhesion of flakes to the surface, resulting in transfer failure. Substrates are cleaned via a combination of methods. Initially a 'deep clean' is performed using 'piranha' solution of H_2SO_4 and H_2O_2 in a ratio of 1:3 to remove any organic material. This is then washed in acetone in a 40°C sonic bath for 10 minutes to remove any remaining debris. The sample is also washed using the same process with isopropyl alcohol (IPA) as the solvent. Substrates are then dried using nitrogen gas and transferred to an oxygen plasma treatment machine for 5 minutes. This also makes the surface hydrophilic, so the samples are vacuum packed before use to ensure nothing adheres to the surface.

3.3.3 Nanopillar fabrication †

Application of strain was achieved by depositing thin flakes onto a patterned substrate (6 μm SiO_2 on Si wafer) containing pillars etched into the substrate, with such pillars ∼250 nm and ∼500 nm in height and ∼1 μm in diameter. These

†Substrate fabrication was undertaken by Dr. Yue Wang but the process is outlined here for context.

pillars were fabricated in arrays with ∼10 μm separation between pillars (scanning electron microscopy (SEM) images of such samples included in Fig. 3.2). To fabricate the nanopillar arrays, a negative resist was deposited onto the substrate, which was then exposed to an electron beam in a technique known as electron beam lithography (EBL). EBL is a useful technique for patterning small features on the scale of tens of nanometers. During this process the negative resist was exposed to the electron beam in the desired pattern (using graphical data stream (GDS) pattern design software), which undergoes a chemical transformation to form cross-links, enabling these areas to remain when the resist is dissolved in a further step known as development. The sample then undergoes reactive ion etching (RIE), with the remaining resist acting as a mask to preferentially etch the areas around the pillars. Any residues are then removed via the deep clean process outlined above.

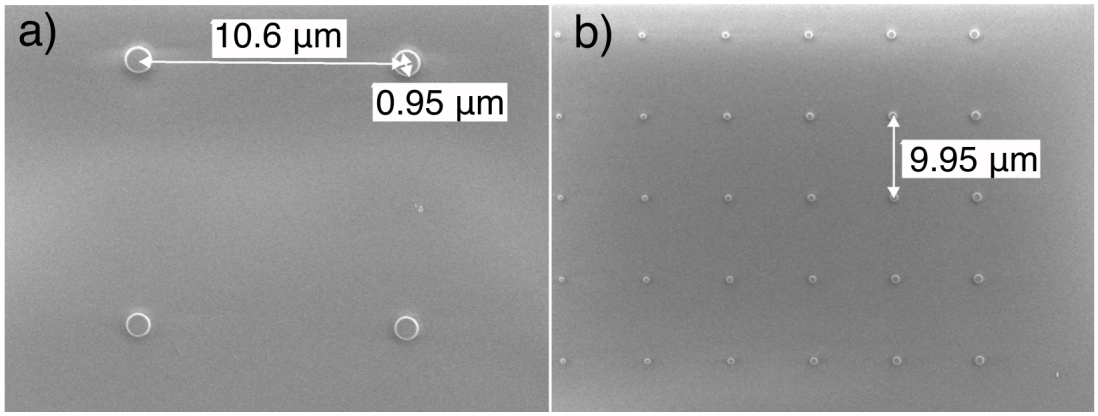

Figure 3.2: SEM images showing examples of patterned substrates with pillar heights of a) 250 nm and b) 500 nm (heights determined separately via AFM).

3.3.4 Dry transfer

Dry transfer is the process used to transfer an exfoliated sample from PDMS to another substrate such as Si/SiO_2. A diagram of apparatus used for this technique is shown in Fig. 3.3. Once the area of PDMS containing the flake is

identified, the PDMS is mounted on a glass slide. This is clamped into a movable arm and the flake is visualised through the glass and PDMS via a microscope. The substrate is heated to 80°C and the flake brought into contact with it. The PDMS is removed using the movable arm after 5 minutes to ensure the flake has fully adhered.

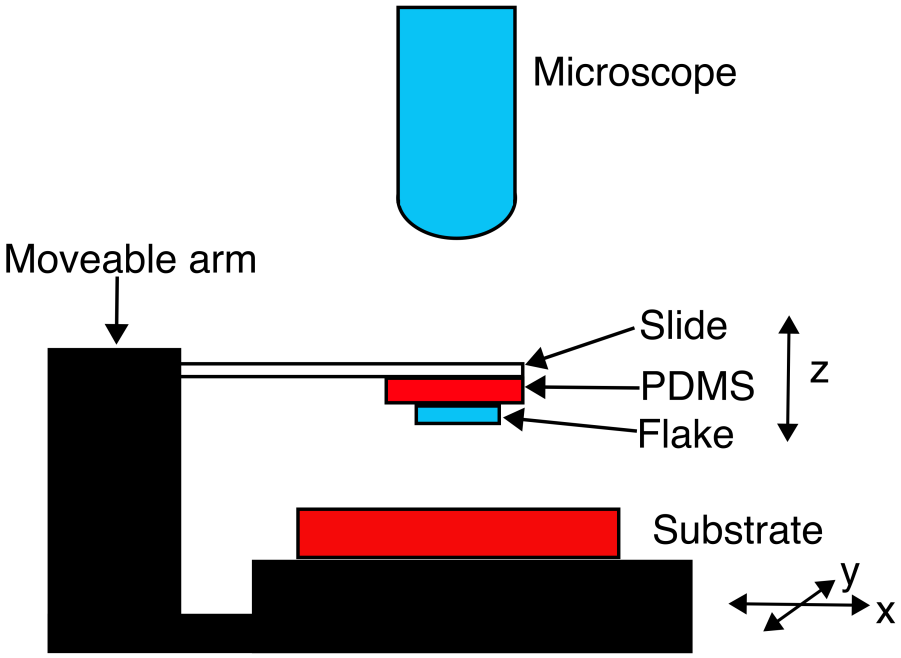

Figure 3.3: Apparatus diagram for the dry transfer of monolayer flakes from PDMS onto a new substrate.

3.3.5 Wet transfer

Wafer-scale samples can be manufactured by CVD. This thesis uses CVD grown monolayer WS_2 samples on a sapphire substrate, which must be transferred from their growth substrate. These are not suitable for dry transfer, so a different process is used - wet transfer (outlined in Fig. 3.4). The sample is spin-coated with Poly(methyl methacrylate) (PMMA) and the bond between the sapphire substrate and the monolayer WS_2 is broken using buffered hydrofluoric acid. The PMMA covered flake is then floated on water and the substrate lifted under

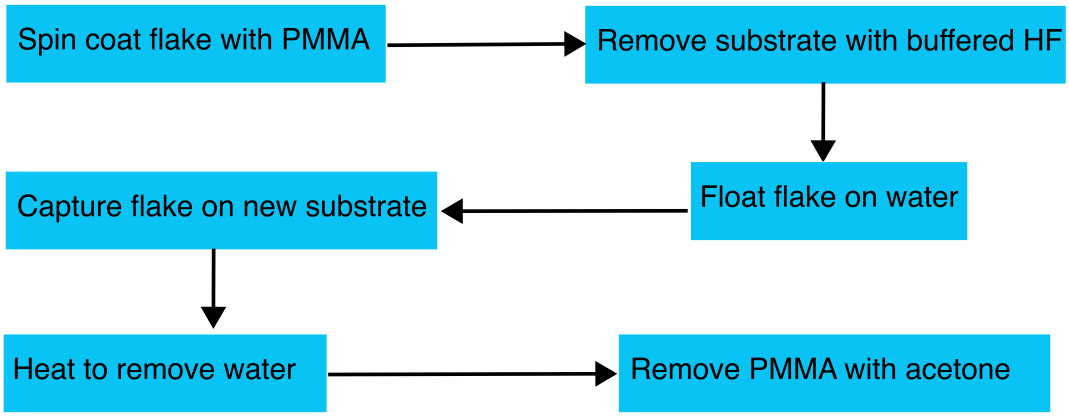

Figure 3.4: Process diagram for the wet transfer of monolayer flakes from sapphire substrates on which they are grown, onto a new substrate.

the water to catch the flake. The substrate is heated for 10 minutes at 60°C to remove any water between substrate and flake, then the PMMA layer can be removed by acetone submersion.

The wet transfer method outlined above is especially useful for large flakes, such as wafer-scale flakes grown on a substrate using methods such as CVD or MBE - however floating the flakes on water for transfer is not applicable to exfoliated flakes due to the smaller and randomly distributed flakes produced by such a process. Wet transfer is a much more complex process involving many steps, so dry transfer of exfoliated flakes is often preferable for experiments involving smaller scale device manufacture. Although wet transfer of exfoliated flakes is possible, its advantages are most apparent for larger, wafer scale samples. It is often not used, therefore, for novel materials as development of growth methods for wafer-scale samples often lags the discovery of such materials. This means exfoliation is usually best for novel materials, as the crystal quality of bulk materials is often better than underdeveloped thin film growth processes. For example only a few wafer scale CVD grown 2D materials are on the market to date. Dry transfer, as a simpler and less expensive process, is often more suitable for such

materials.

During wet transfer, there is more opportunity for a sample to relax compared to dry transfer which can result in lower mechanical strain induced by such a process (see chapter 5).

3.3.6 Atomic Force Microscopy

Another technique used to characterise surfaces is AFM (Bruker Bioscope Resolve), which enables the three dimensional profile of a surface to be mapped and number of layers determined with a height resolution of ∼0.1 nm. An example image of a few layer WS_2 sample is shown in Fig. 3.5, with a minimum thickness of four layers. AFM involves moving a sharp tip mounted on a cantilever across a sample to measure the force between atoms in the tip and those of the sample via deflection of the cantilever. This work makes use of the so-called tapping mode, which involves oscillating the tip close to its resonant frequency such that the tip is only in contact with the surface at one point in its oscillation and scanning this across the surface of the sample. The distance of closest approach between tip and sample is kept constant throughout the measurement via a feedback loop to maintain constant tip-sample interaction forces. This work makes use of the technique to visualise areas of strain within a two dimensional sample on a patterned substrate in chapter 5.

3.3.7 Photoluminescence measurement

PL is measured from the sample using a 532 nm laser, which is focused onto the flake to excite electrons into the conduction band. The wavelength of 532 nm was chosen as this is above the band gap energy, thus has the required energy to excite electrons across the band gap. The subsequently emitted light from the sample is collimated using an objective lens (numerical aperture of 0.55 to form a

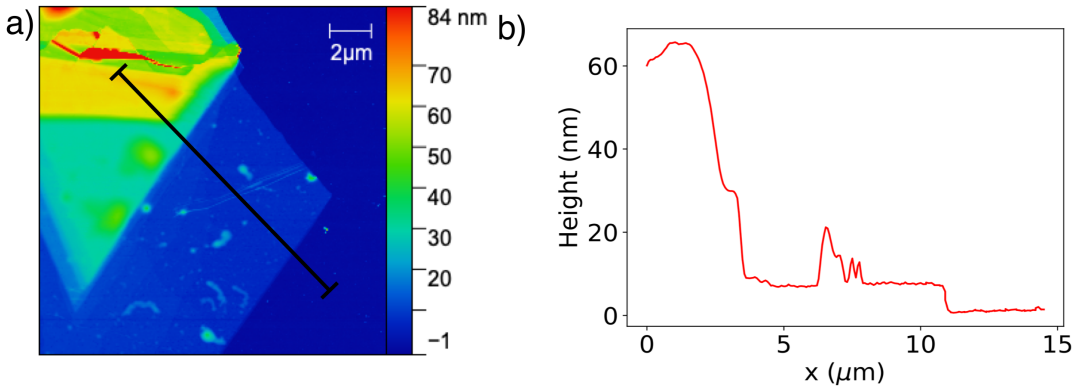

Figure 3.5: Figure showing a) AFM image of few-layer WS_2 flake, highlighting thickness differences between different numbers of layers and b) height profile shown along black line in a).

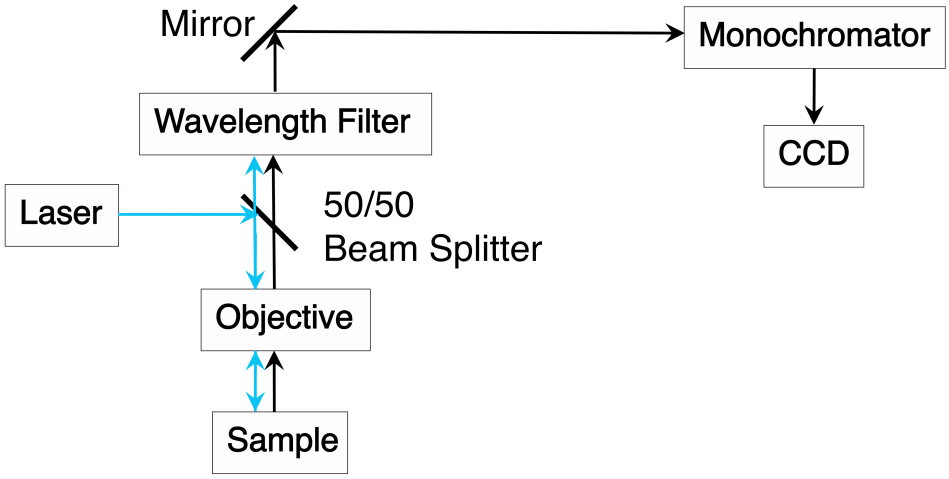

Figure 3.6: Schematic of micro-PL setup, showing excitation laser light in blue and photoluminescence signal in black.

spot size of ~2 μm), then passes through a filter to remove light at the excitation wavelength to avoid saturation of the detector. The light is then focused into a monochromator to disperse the light into a charge coupled device (CCD). The spectrum can be integrated over a specified time to increase the signal. The sample stage can be moved in three dimensions to probe different areas of the sample and focus the beam. Taking data by scanning in 2D is advantageous over scanning across a line profile, as it removes errors associated with aligning the

scanning line with the strained area in a study of strain. For example, if a line profile was taken slightly offset from the pillar, the strained area may not be captured. Although this could be rectified by pre-scanning the PL in the area using a large sample spacing to ensure the correct area is aligned, the 2D method increases both the repeatability and automatability of the process. An image of the actual photoluminescence measurement setup is shown in Fig. 3.7.

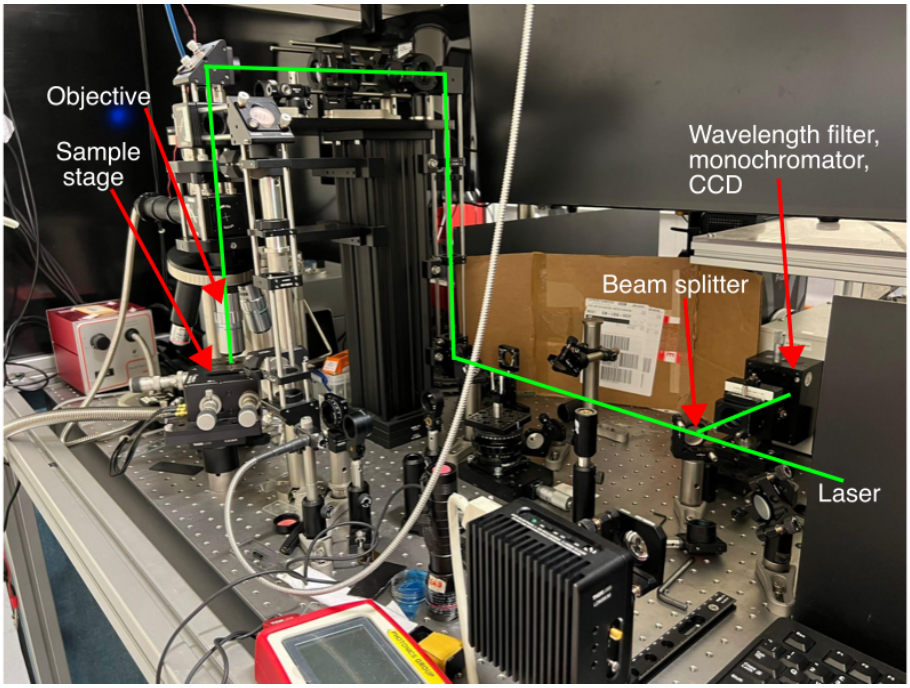

Figure 3.7: Labelled image of micro-PL setup, showing excitation laser path in green.

Chapter 4

Strain engineering [†]

4.1 Introduction

MoS_2, is one of the most studied vdW materials due to its band gap character changing with number of layers. The change in band gap character in MoS_2 with reduced number of layers is a result of a quantum confinement effect, as the sulfur states (near the Γ point) extend spatially across layers whereas the molybdenum states (near the K point) do not, due to the position of molybdenum within the unit cell. The result is that reducing layer thickness only changes the energies of states at points within the Brillouin zone (BZ) corresponding to sulfur states, changing the band structure more significantly at the Γ point than at the K point and leading to a change in band gap position in reciprocal space, as illustrated in the partial charge density visualisations shown in Fig. 4.1 [60]. This change in nature and position in k space of the band gap is also known to occur when strain is applied to the system [68].

[†]This chapter has been adapted from work that is published: Alex Armstrong, Keith P. McKenna, and Yue Wang. "Directional dependence of band gap modulation via uniaxial strain in MoS_2 and TiS_3" Nanotechnology, 35(1):015704, 10 2023 [67].

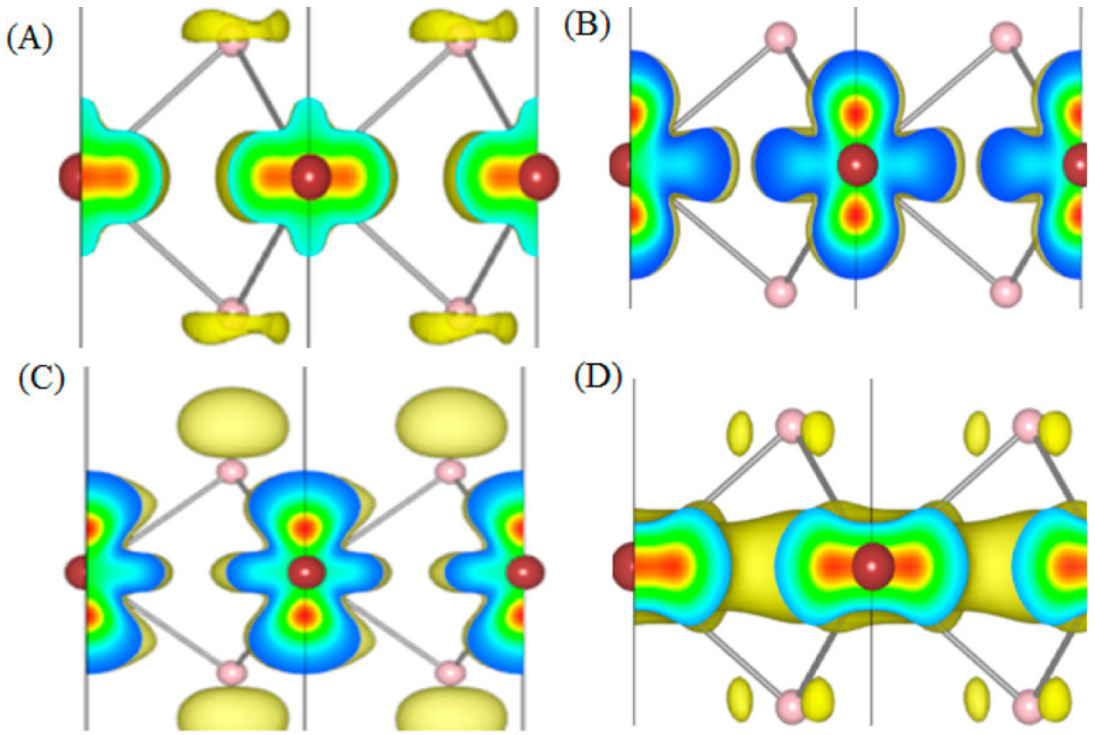

Figure 4.1: Spatial charge distribution for monolayer MoS_2, showing a) CBM at k point between Γ and K points b) CBM at K point c) VBM at Γ point and d) VBM at K point. Reproduced from [69] under a creative commons license.

TiS_3 is a layered material with many similarities to MoS_2, such as its direct band gap and semiconducting nature. It has also gained interest due to its smaller band gap, i.e. longer emission wavelength in the infrared range [70]. MoS_2 and TiS_3 can both be exfoliated as single- or N-layer flakes, with the MoS_2 band gap transitioning from direct to indirect as the number of layers are increased, accompanied by a reduction in PL yield [60], while the TiS_3 band gap character remains stable for mono- and few- layer systems. This is an important property since it would allow higher thickness tolerances, making TiS_3 particularly attractive for device and engineering applications. The band gap in both materials can be further manipulated with strain, enabling control over the position of the peak wavelength of the PL spectrum [24, 71, 72]. However, the effect of the strain direction on the band structures is not well studied. This is a question which

could impact viability of real-world applications if crystal alignment to strain direction must be considered. Heterostructures involving multiple vdW materials could also be affected, as strain can be introduced in the heterostructure growth or formation process. The impact of the strain could then vary depending upon its direction within the layers [73]. The directionality effect could also impact the field of twistronics, where angle is a highly critical parameter due to the large variation in supercell size with small twist angle [74]. In this chapter, we investigate this open question for both TiS_3 and MoS_2 using density functional theory.

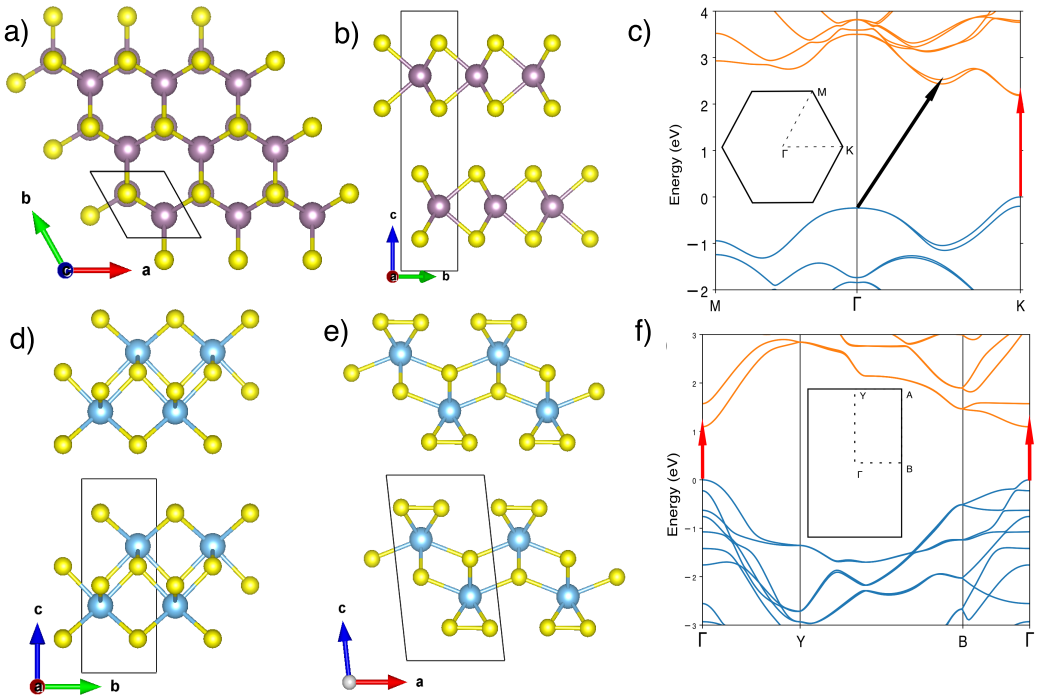

Figure 4.2: Structures, band structures and brillouin zones of MoS_2 and TiS_3 (structures created using VESTA [75]). (a,b) and (d,e) show the structures for MoS_2 and TiS_3 respectively (Mo purple, S yellow, Ti blue). Top and in-plane orientations are shown for MoS_2 in (a,b), however two in-plane orientations are shown for TiS_3 in (d,e) to illustrate its anisotropic structure. Two layers are shown for each material to show the layered structure. (c) and (f) show the band structures with 2D brillouin zones shown in insets for MoS_2 and TiS_3 respectively calculated on 2H-MoS_2 at HSE06 level of theory with Grimme's D3 corrections including spin orbit coupling [48]. Direct (red arrows) and indirect (black arrows) transitions labelled.

Differences in symmetry between these two materials are likely to cause different directional responses to strain. 2H-MoS_2 has a hexagonal symmetry, with its atoms arranged in a trigonal prismatic structure and space group P63/mmc in its bulk form, which then loses inversion symmetry in monolayer (ML) form, with the space group changing to $P\bar{6}m2$ [76]. TiS_3 has a monoclinic structure with a $P2_1/m$ space group, making it more anisotropic [77]. This can, however, be approximated to an orthorhombic structure for the monolayer system, as the angle of the cell perpendicular to layers can be neglected for the monolayer case. The bulk structures for MoS_2 and TiS_3 (Fig. 4.2a-b and d-e respectively) consist of layers stacked in the **c**-direction with weak van der Waals forces dominating between layers. For MoS_2, two transitions are important: the bulk indirect transition and the monolayer (ML) direct transition. The bulk band gap transition in reciprocal space is located between the Γ point and the halfway point between the Γ and K points (Fig. 4.2c), which then changes to a direct transition at the K point when in the ML form [60, 78]. The band gap transition is consistently direct and at the Γ point in ML and few-layer TiS_3 systems (Fig. 4.2f) [70]. The MoS_2 bulk and ML band gaps have been measured experimentally as 1.29 eV and 1.9 eV respectively using a combination of PL, optical absorption and photo-conductivity techniques [79], with DFT predictions varying significantly depending on the approximations employed (discussed further below).

Reduction in the band gap energy with increased lattice strain in MoS_2 has been reported experimentally using different methods of introducing strain, many of which may also be applicable to TiS_3 [80–82], for example Manzeli *et al* applied strain using an AFM tip and recorded a change in band gap measured via the piezoresistive effect [81]. This measurement has been supplemented with first principles predictions at various levels of theory [83–85]. Asymmetrical biaxial strain in MoS_2 involving some directional effects has been investigated computa-

tionally by Deng *et al*: fixing both lattice parameters a and b at various strain values (where strain along the two directions is not necessarily equal) to find the band gap in the **a**-**b** parameter space [86].

In this study, to model uniaxial strain we instead fix the unit cell for both materials along the direction of applied strain only, allowing for full structural optimisation in the perpendicular direction. Strain oriented along the two directions has been investigated for TiS_3, but not for intermediate directions [72]. Once the directional dependence of strain on the band gap is well understood, this determines if the alignment of a crystal relative to the strain axis necessary for the desired electrical and optical properties and performance in mechanically flexible devices, such as sensors, LEDs, transistors, and photodetectors [7, 87].

4.2 Method

All DFT calculations were undertaken using a plane wave basis set, as implemented in VASP [88]. A gamma centred Monkhorst-Pack grid of 8×8×1 k points was used to sample the Brillouin zone for all calculations, with optimized structures converged to a force tolerance of 0.01 eV/Å. Both PBE and HSE06 functionals were employed, with and without Grimme's D3 vdW corrections (shown as +D3 after functional name) [48]. For hybrid calculations, all supercells were first pre-optimised using PBE to allow for quicker convergence. Ideal values of D3 parameters for HSE06 are still an open area of research and could not,therefore, be sourced from literature, so this study used parameters quoted for the related hybrid functional PBE0 for calculations. Band calculations were then run on the optimized structures along a path through k space generated by SUMO package [89]. Version 5.2 PBE plane wave potentials (PAW) were used for all calculations, with plane wave cutoff value of 520 eV to ensure a sufficient basis

set while maintaining computational efficiency. Spin-orbit coupling was included for both geometry optimisation and band structure calculations.

The lattice constants of bulk 2H-MoS_2 have been experimentally measured using x-ray diffraction (XRD) as $\mathbf{a}$ = 3.16 Å (in plane) and $\mathbf{c}$ = 12.29 Å (out of plane) [90, 91]. Numerous DFT calculations have also been undertaken for MoS_2 using various levels of theory in order to calculate different properties. In plane lattice constants are generally close to the experimental values using either the GGA or hybrid levels of theory, for example $\mathbf{a}$ = 3.17 Å (PBE) [92] or $\mathbf{a}$ = 3.18 Å (HSE06) [93, 94]. There is some variation in the literature relating to different code implementations and parameters. The out-of-plane lattice constant is governed by the weaker inter-layer coupling, so is generally overestimated if Grimme's dispersion corrections are not included [48, 92, 95]. With regard to the choice of functional, one issue is that while yielding reasonably accurate lattice structures, GGA functionals such as PBE are known to underestimate band gaps [96]. This error can be reduced by using a hybrid functional which combines a GGA functional with a fraction of Hartree-Fock exchange [44]. The lattice structure also affects the band gap, so for a layered material inclusion of an approximate treatment of Van der Waals forces is necessary to enable more accurate lattice structure prediction. This is irrelevant in the monolayer systems, but is included for bulk systems [78,97]. The exciton binding energy can lead to a large difference between the calculated electronic band gap and the optical band gap measured experimentally [98,99]. GW calculations can predict a more accurate band structure when including the exciton binding energy, although trends in band gap should remain accurate for GGA and hybrid methods. The lattice parameters and band structure for TiS_3 were not calculated at different levels of theory to compare as it was assumed that the materials are similar enough that the same functional for both materials would suffice. The validity of this

assumption is further evidenced by the accuracy of lattice constants calculated to within 0.04 Å and 0.02 Å for **a** and **b** lattice constants respectively compared to experimental results [14]. This also ensured the calculations could be more easily compared between the materials.

Optimisation of materials subject to uniaxial strain in the x direction was performed by a small modification to the VASP source code to ensure the stress matrix was only non-zero along the direction perpendicular to the applied strain, therefore enabling optimization only along this direction. The desired strain is then imposed by multiplying the components of the lattice vectors along the strain direction by the relevant strain, as shown in Fig. 4.3. Strain can be applied in arbitrary directions by rotating the supercell in the **a**-**b** plane such that the desired strain direction is aligned along the x direction. We further verified the method reaches an energy minimum by calculating the energy of structures with the angle between **a** and **b** vectors changed by ± 0.5 degrees.

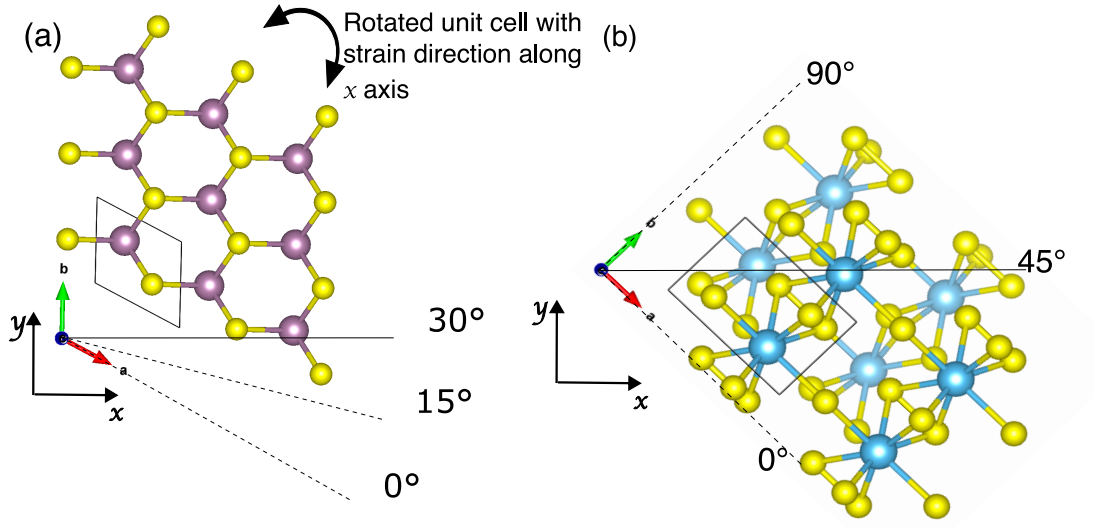

Figure 4.3: Method of applying uniaxial strain by rotating the unit cell to align with the x direction then increasing the components of the lattice vectors along this direction (x and y directions shown in axes). Only y components of lattice vectors are allowed to relax during cell optimisation. MoS_2 and TiS_3 are both shown with strain directions defined as angle from the **a** lattice vector. Exaggerated strain is applied to (a) to illustrate approach.

In order to gain further insight into the effect of strain on the band structure, band decomposed charge densities were calculated using the k points corresponding to the band edges and charge isosurfaces visualised in the VESTA package [75]. Due to limitations with the k point grid sampling, it was not possible to use k points corresponding to the exact conduction band minimum so the closest point to the band edges in the k point grid was used for this type of analysis.

4.3 Results

Table 4.1: Comparison of lattice parameters and band gap transitions predicted by different functionals for MoS_2. E_g^{Direct} and $E_g^{Indirect}$ are the direct and indirect band gap transitions respectively.

Functional	E_g^{Direct} (eV)	$E_g^{Indirect}$ (eV)	**a** (Å)	**c** (Å)
PBE(No SOC)	1.46	1.65	3.190	14.876
PBE	1.46	1.59	3.190	14.880
PBE+D3	0.96	1.63	3.170	12.490
HSE06	2.05	2.10	3.157	14.780
HSE06+D3	1.53	2.16	3.136	12.336
Experimental [100, 101]	1.29	-	3.168	12.322

The predictions of different functionals for lattice parameters and band gaps of bulk 2H-MoS_2 are compared in Table 4.1. The in plane lattice constant, **a**, is close to that measured in experiment for all functionals tested. The out of plane lattice constant, **c**, was found to be far higher than experiment for both PBE and HSE06 unless D3 corrections were applied, which significantly reduced **c** to be close to the experimental value. This suggests PBE+D3 or HSE06+D3 would be good choices for this material.

The dependencies of direct and indirect band gaps on functional choice are also shown in Table 4.1. Firstly, one can see there is a significant difference between the direct band gaps at the PBE and PBE with no spin orbit coupling (SOC) levels of theory. We include, therefore, SOC in all subsequent calculations. It

can also be seen from the difference between PBE and PBE+D3 functionals that the effect of D3 parameters was to reduce the indirect band gap, maintaining a similar direct band gap between the two cases. This was then mirrored in the hybrid calculations. Another effect of the inclusion of D3 parameters for both HSE06 and PBE functionals was a change in location of the CBM from the K point to the K-Γ midpoint, bringing the band structure closer to profiles calculated in the literature [60]. Finally, the effect of changing from PBE and HSE06 was to increase both the indirect and direct band gaps by a similar amount. Thus we conclude that the closest band gap to experiment is obtained using the HSE06+D3 functional. Although this approach predicts a fundamental gap far higher than the experimental band gap, the latter is based on optical measurement of the band gap, which is expected to be lower than the fundamental band gap by the exciton binding energy.

We then investigate the strain-engineered properties of ML MoS_2 and TiS_3 using tensile strain. The unit cells used for the ML were generated using the HSE06+D3 optimised bulk structures (Fig. 4.2) with a vacuum gap of 20 Å introduced, sufficiently large to remove interactions between periodic images. A symmetrically nonequivalent range of strain directions were sampled according to the unit cell symmetry. A 30 degree range and 90 degree range for MoS_2 and TiS_3 respectively were spanned (direction defined in degrees anticlockwise from the x direction shown in Fig. 4.3) and sampled every 15 degrees with various levels of uniaxial strain applied up to 5%. A larger range was necessary for TiS_3 due to the reduced symmetry in comparison to MoS_2. Both direct and indirect transitions were investigated for MoS_2 to assess which transition has a lower energy but this was unnecessary for TiS_3 as the direct transition has the lowest energy for both monolayer (ML) and few layer systems [70].

MoS_2 has two independent bonds per unit cell, one of which is increased in

length while the other decreases with applied strain, as expected to maintain a positive Poisson ratio. For each of these bonds, the difference in bond length for 5% strain along 0° and 30° directions is only 0.01 Å, suggesting a highly isotropic effect. TiS_3 has many more independent bonds per unit cell due to its more complex structure and here we focus on the two most significant bonds for band gap determination (the bonds with highest band edge charge density localised along these two bonds, which are circled in blue and black in Fig. 4.5b). These are oriented along two perpendicular directions and hence can be strained independently from each other. The change in length of these bonds for 5% strain along 0° and 90° is 0.2 Å and 0.1 Å for the Ti-Ti and Ti-S bonds respectively - an order of magnitude larger than the changes seen between strain directions for MoS_2.

Figure 4.4 shows how band gaps vary with strain applied in different directions in the ML systems. Band gaps in MoS_2 vary linearly, independent of direction. Least square linear fits were applied to direct and indirect gap trends separately and gradients with statistical error calculated from the fit. The strain at which the band gap changed from direct to indirect for each direction was found to be around 5.3-5.4 % for all three directions (although this is quite sensitive to the level of theory employed, so it is expected that the gradient of the band gap energy with respect to strain would be more useful for comparison to experiment [102]). In TiS_3 the story is different, as the band gap variation can only be reasonably approximated as linear with respect to strain for the extrema at 0 and 90 degrees. The gradient of the response is, therefore, not a good figure of merit for this system. Interestingly, the band gap energy change (ΔE_g) with increasing strain changes from negative, when applied along the **a** lattice vector, to positive, when applied at 90 degrees to this, highlighting the anisotropic nature of the effect in TiS_3 in contrast to the MoS_2 case. The total energies per unit cell as a function of

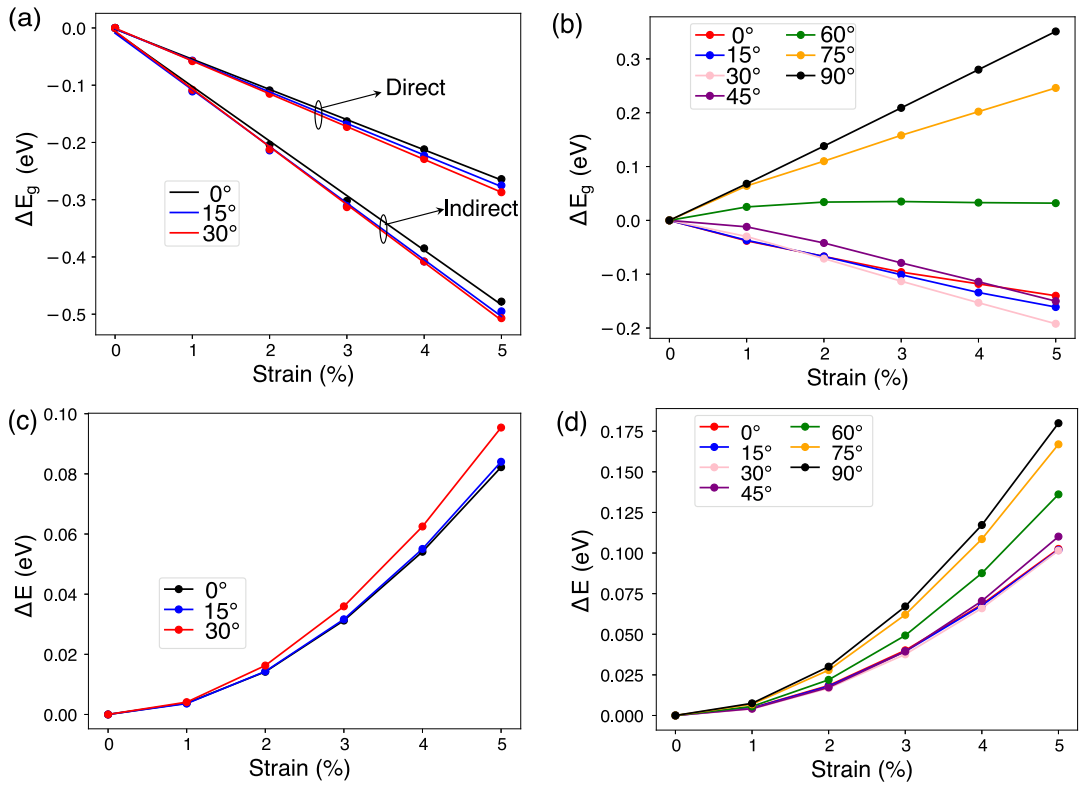

Figure 4.4: Changes in band gap transition energies compared to the unstrained system (ΔE_g) as a function of strain, with strain along different directions for a) MoS_2 and b) TiS_3, and total energies for these strains and directions are shown for c) MoS_2 and d) TiS_3. Modulations of the direct transition is shown for TiS_3, and modulation of both direct and indirect transition shown for MoS_2. Linear fits are shown for a) but lines are just a guide to the eye for b-d).

strain are also shown for both MoS_2 and TiS_3 in Fig. 4.4c and Fig. 4.4d. It can be seen that there is little difference in energy between directions at the maximum strains for MoS_2 (13.2 meV). This is in contrast to the case of TiS_3, where a far larger difference in energy 77 meV can be seen between 0 and 90 degrees. This suggests TiS_3 has a greater anisotropy in its elastic constants than is the case for MoS_2.

Changes in structure in the two materials under strain can also be noted. In MoS_2, there are two bonds per unit cell, both of similar length. Under five percent strain, one bond changes from 2.387 Å (unstrained) to 2.416 Å and 2.433 Å with strain along 0° and 30° directions respectively – corresponding to percentage

changes in length of 1.2% and 2.0%. The other bond changes from 2.387 Å (unstrained) to 2.370 Å and 2.375 Å with strain along 0° and 30° directions respectively – corresponding to percentage changes in length of -0.7% and -0.2%.

In TiS_3, two relevant bonds are identified, as shown in Fig. 4.5. The 'Short bond' changes under 5 percent strain from 3.383 Å (unstrained) to 3.365 Å and 3.552 Å with strain along the 0° and 90° directions respectively – corresponding to percentage changes in length of 0.5% and 5%. The 'Long bond' changes from 2.627 Å (unstrained) to 2.725 Å and 2.617 Å with strain along the 0° and 90° directions respectively – with percentage changes in length of 3.7% and -0.4%.

The differences in structure with strain aligned along different directions can be seen to be more pronounced in TiS_3 compared to MoS_2 due to notable differences in symmetry.

To provide further insight into the weak dependence of the band gap on strain direction for MoS_2, we analyse band decomposed charge densities corresponding to electronic states at the band edges (Fig. 4.5). At both the CBM and VBM in the unstrained system, the MoS_2 charge density is clearly not isotropic, resulting in some directional dependence on the band decomposed charge densities. However, the band decomposed charge density is localised mostly around the molybdenum atoms for both bands. This means that there is similar charge density along each of the bonds, suggesting straining each bond has a similar effect on the VBM/CBM energy. After straining, the 0° and 30° cases show similar charge densities, with only a small difference in the distribution in the CBM. This small difference explains the weak directional dependence of strain on the band gap.

The band decomposed charge density calculation results shown in Fig. 4.5 provide some explanation as to the different response to strain in TiS_3 compared with MoS_2. The valence band shown in Fig. 4.5b has charge localised along a

'long' Ti-S bond oriented parallel to the a lattice vector (circled in black), while the conduction band has charge localised along a 'short' Ti-Ti bond perpendicular to this direction (circled in blue). This causes the charge density along these 'long' and 'short' bonds to be modified more when strain is oriented along the a and b lattice vectors respectively. If stretching both bonds causes an increase in band energy, the valence band energy will be increased with strain along the **a** lattice vector, while the conduction band will be increased with strain along the **b** lattice vector. This will result in a decrease in band gap for the former case and an increase for the latter. The origin for the non-linearity observed at intermediate directions is not immediately clear and is likely due to the complex interplay between these two effects when there is a strain component along both **a** and **b** directions. Only the high symmetry directions were included here to illustrate the directional variation, as these directions showed the largest differences in the character of band edge states.

4.4 Discussion

The initial hypothesis that the strain-band gap relationship would be close to isotropic for MoS_2 and highly anisotropic for TiS_3 was proven to be correct. The non-linear transition between the high symmetry directions in TiS_3 was, however, unexpected. This builds upon work by Kang *et al.* where only the extreme directions were investigated in TiS_3, going further to compare to MoS_2 and provide insight as to how the differences between the two arise [103]. A study by Deng *et al* also found a similar directional symmetry of band gap variation for biaxial strain in MoS_2 [104].

The inclusion of excitonic effects using the Bethe-Salpeter equation could enable PL spectra to be calculated for easier comparison to experimental results

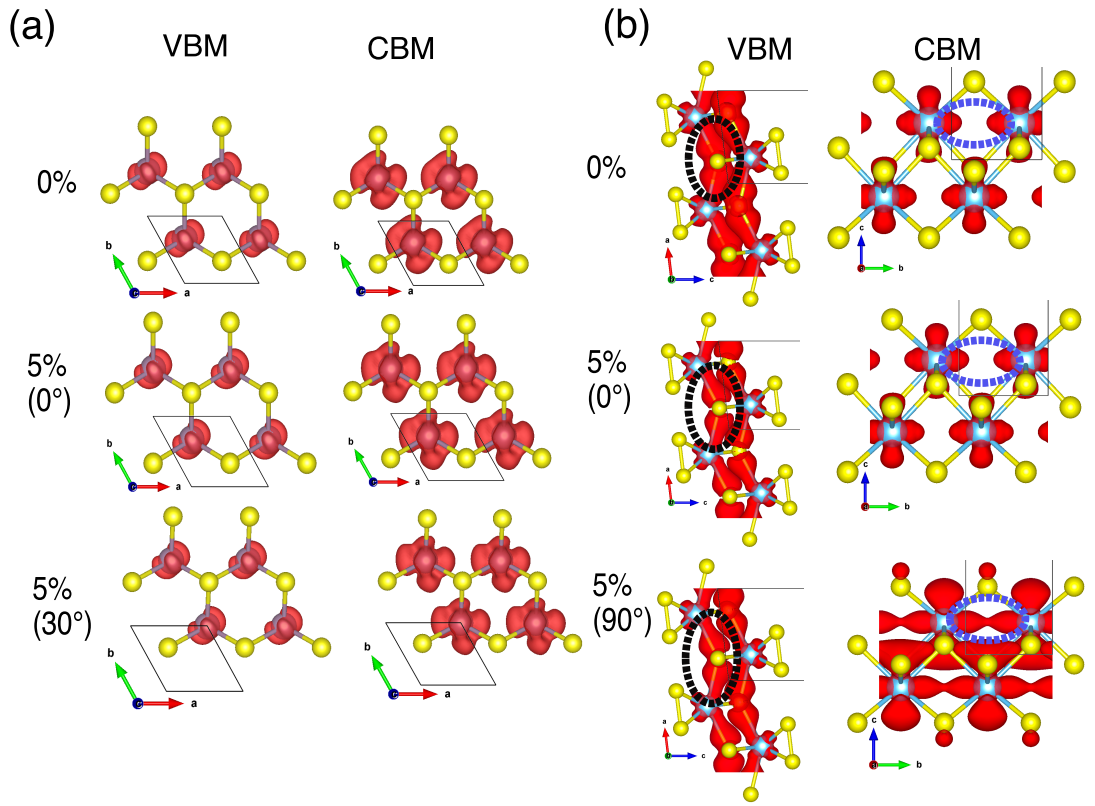

Figure 4.5: Band decomposed charge densities in a) MoS_2 and b) TiS_3 for VBM and CBM, for the unstrained system, and 5% strain applied along high symmetry directions. Isosurfaces are visualised using VESTA [75] with isosurface levels of 2.5×10^{-5} eÅ^{-3} for the VBM and 3×10^{-5} eÅ^{-3} for the CBM. Relevant TiS_3 bonds (most affected by strain) for strain in different directions referred to as 'long bond' and 'short' bond are circled in black and blue respectively. The VBM and CBM charge densities for TiS_3 are shown viewed along the b and a lattice vectors respectively to highlight directions with largest changes (unnecessary for MoS_2 due to higher symmetry).

and the exciton binding energy to be included in calculations. However, these types of calculations were not used in this study due to their prohibitive computational cost [105]. We expect the hybrid DFT approach used in this study to remain reliable for studying the trends in the variation of band gaps with strain, although quantitative evaluation of energies is likely to have 100s of meVs offset (exciton binding energy) from experimental values.

Weak directional dependence of the strain on band structure could be useful

in all application of uniaxial strain. Thankfully, in the case of MoS_2 we would not need to consider the crystal alignment to gain close to the maximum change in band structure. This is an advantage experimentally as crystal alignment is likely to limit real-world applications, as it can be difficult and is often not easily reproducible. As other 2H phase TMDs have similar hexagonal structures to MoS_2 this weak directional is likely also extendable to these materials (including WS_2, $MoSe_2$, $MoTe_2$ and WSe_2).

The advantage of TiS_3 is the freedom to increase or decrease the band gap by rotation of the strain axis. It is not clear what level of maximum strain could be supported by TiS_3 experimentally along the **b** lattice vector, as the material often breaks into long 1D flakes. This could be investigated further experimentally to discover what level of band gap change can be induced in reality. This behaviour is likely extendable to similarly structured trichalcogenides such as ZrS_3, $ZrSe_3$ and HfS_3 due to the structural origin of such behaviour. Experiments could be devised to investigate these predicted effects e.g by applying strain along different directions in the crystal and monitoring their photoelectric properties.

4.5 Conclusion

The variation of band gap with uniaxial strain applied along different directions for both MoS_2 and TiS_3 was investigated by DFT calculation. MoS_2 was found to exhibit negligible anisotropy in band gap modulation, but strong anisotropy is predicted for TiS_3. This results in a change in the gradient of the band gap with respect to strain from negative to positive, as the strain direction is rotated from the a to the b lattice vector directions. A non linear response was observed for the intermediary directions in TiS_3 due to the complex interplay between the system asymmetry and strain, whereas the MoS_2 system maintained a linear behaviour

for all strain directions, reflecting its more symmetric structure. From this we can conclude that the band gap in TiS_3 and likely other trichalcogenides with similar structures, can be either increased or decreased by strain. Such an effect is only limited to a small decrease in MoS_2 and other hexagonal dichalcogenides. Such directional dependent stain-induced band gap engineering could be useful in optoelectronic applications, for example to achieve fine tuning of the wavelength in light emitting devices. Further work is necessary to identify the maximum level of strain that TiS_3 can be physically supported along these crystal directions.

Chapter 5

Experimental strain effect on photoluminescence

5.1 Introduction

Following the success of other TMDs such as MoS_2, WS_2 has gained interest in recent years due to its similar structure and properties to MoS_2. As a result of these similarities, many of its applications are similar. For example applications have been realised in devices such as light emitting diodes (LEDs) and photodetectors [106, 107]. One of the main properties affecting such applications is in the band gap; bulk WS_2 has a band gap of 1.35 eV compared to the bulk MoS_2 band gap of 1.29 eV [79, 108]. The corresponding figures for monolayer are 1.97 eV and 1.9 eV for WS_2 and MoS_2 respectively [79, 109]. This similarity extends to the position of these transitions in reciprocal space; both MoS_2 and WS_2 have an indirect transition from Γ to halfway between Γ and K in the bulk and a direct transition at the K point in the monolayer [60, 78, 110]. The similarity in band structure enables WS_2 to be substituted for MoS_2 in some applications and, despite W and Mo having similar earth abundances, W currently has lower

demand pressures. WS_2 has also been reported to have the highest PL quantum yield of all transition metal dichalcogenides (TMDs) potentially making it a better choice for future technologies [110, 111]. Although similar, these differences are apparent enough to incentivize WS_2 research in its own right. This work focuses on tuning the band gap of WS_2 for such applications. As noted in chapter 4, introduction of lattice strain has emerged as a useful tool enabling band gap tuning. This, in turn, can change the PL of a strained sample, enabling the level of strain to be measured. Strain has been predicted to change the band gap by ∼55 meV/%, calculated using DFT [112]. Band gap engineering via strain has been experimentally realized through different methods of strain application, for example by transferring WS_2 to a flexible substrate such as PDMS and bending the substrate to induce strain, a system for which a strain of ∼0.5% and a band gap variation of ∼60 meV/% has been reported [113]. While useful in its ability to introduce a range of different strains, this method may not be optimal for many devices as bending occurs over a macroscopic length scale, thus does not lend itself to miniaturization. Another method for applying strain is by transfer of a monolayer flake onto a range of nanopillars patterned into a substrate - enabling a strained region to be formed in the surrounding area of the pillar [114]. Although not novel in itself, the method is further investigated within this work via PL studies, with an emphasis on optimisation of the method to maximise induced strain. This is initially investigated by varying the height of pillars and also highlighting differences in PL when using different flake transfer processes (using wet or dry transfer techniques). While strain induced via bending of a flexible substrate is mechanically tunable in real time, this impacts reliability as there is more chance of the flake slipping on the substrate. In contrast, induction of strain via pillars results in a set level of strain post-transfer. However the fixed position of the sample increases the reliability of such a system. The pillar mech-

anism could also apply to a variety of geometries, as the strained area is smaller and can therefore can induce strain on curved or flat substrates. We choose to use the pillar method in order to quantify the reliability of the method for differently prepared systems, allowing a more direct comparison between these methods.

5.2 Method

To prepare dry transfer samples, WS_2 samples were exfoliated onto PDMS and monolayer areas identified via optical microscopy. The monolayer areas were then transferred to nanopillarred SiO_2/Si substrates by directly applying the PDMS to the substrate surface and removing (dry transfer). Exfoliated flakes could have been used for both wet and dry transfer processes. However as we had access to CVD grown wafer scale samples provided by our industrial collaborator (AIXTRON) we were able to cover a large array of pillars but these samples can only be transferred via wet transfer. These CVD grown samples had a far lower PL efficiency ($\sim$10x lower) due to an increased level of defects. Wet transfer is a more involved process - CVD grown monolayer WS_2 samples on sapphire substrates were spin coated with PMMA and etched from the sapphire using hydrofluoric acid. These PMMA coated flakes were then floated on water and brought into contact with the substrate. The sample was heated to evaporate any water between substrate and flake and the PMMA removed with acetone. Substrates used contained pillars of $\sim$250 nm and $\sim$500 nm to assess the effect of pillar height variation on strain level introduced. All pillars were spaced by $\sim$10 μm to minimize interaction between strain fields from neighboring pillars while maintaining a sufficient pillar density to cover more than one pillar with each flake, improving the chance of successful strain introduction per sample. The PL spectrum was measured using a 532 nm pump laser, focused onto the

sample using a 50x objective to give a spot size of 1 μm. A map of spectra was taken for each sample with a step size of 1μm to be consistent with the spot size, however the z height was adjusted to maximise the PL signal only prior to the first spectrum being taken due to the large number of spectra required. This enabled a 2D map to be constructed, effectively imaging the PL across a given area. Dry transfer samples used lower integration times than wet transfer samples due to higher observed PL signals, using 1s unless otherwise specified (in some cases 0.5s was necessary due to CCD saturation). Wet transferred samples required 5s integration time. Laser power also differed between dry and wet transfer samples for this reason: 0.96 mW and 3.2 mW laser powers were incident on the sample for dry and wet transfer respectively. The spectra were characterised based on their integrated intensity and peak wavelengths. The peak wavelength was found by fitting of a single gaussian to the top 80% of each spectrum, while integrated intensity was integrated across all wavelengths captured by the CCD. When plotted in 2D maps integrated intensities in each map were normalised by dividing all integrated intensities by the highest value in each map. Strained areas were subsequently imaged with AFM using an RTESPA-300 tip to correlate any changes in PL with strained areas and highlight any broken flakes.

5.3 Results

Optical images of exfoliated WS_2 flakes dry transferred onto patterned substrates are shown in Fig. 5.1, with monolayer areas highlighted. Optical images of wet transferred flakes are not shown as large (cm scale) monolayer areas result in very limited contrast as can be seen from the dry transferred monolayer areas in Fig. 5.1. The minimal contrast in these areas highlights the need for confirmation that pillars are fully covered using AFM images.

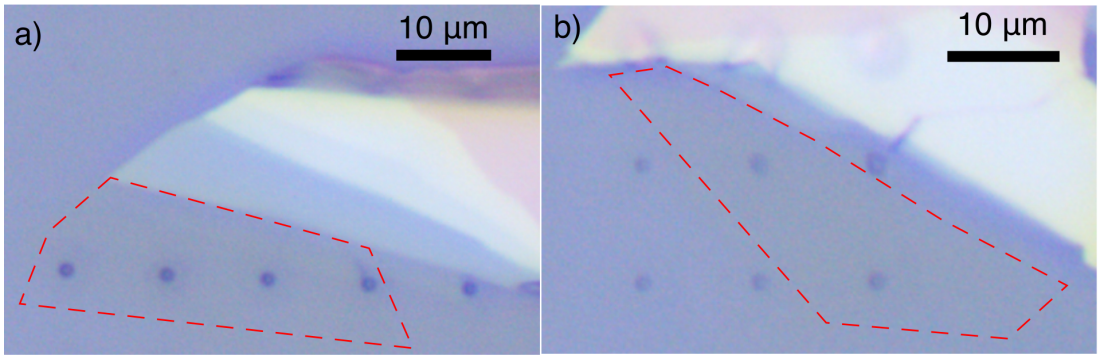

Figure 5.1: Optical images showing dry transferred WS_2 flakes on a) ∼250 nm ad b) ∼500 nm pillars. Monolayer areas are outlined in red dashed lines, with scale bars shown (top right of each image).

Examples for typical PL curves taken for strained and unstrained dry transferred monolayer areas on a ∼250 nm pillared substrate are shown in Fig. 5.2. As the probe was moved from an unstrained to a strained area, both peak wavelength and width increased - the peak due to the higher wavelength emission due to strain, and the width due to both strained and unstrained areas being illuminated by the pump laser due to the finite spot size. This is reflected in the integrated intensity which also increases due to the increase in peak width without a large decrease in intensity. The integrated intensity could be expected to stay constant or reduce when the strained area is probed because there is no change in the incident photon intensity and, all else being equal, absorption should not change. In this case, however, the photon absorption is reduced by the substrate due to scattering with optical phonons at the surface and in strained areas the sample is often suspended. The increased PL from suspended material compared to a flake adhered to a substrate is well-known in TMDs [115]. The wavelength changed due to a decrease in band gap, which would also result in a broadening of the peak as the finite laser spot size resulted in areas of both low and high strain being probed in each spectrum. This means a range of band gap would be present in each region, as a strain gradient can be assumed rather

than a step-change. The suspended flake can be seen in the AFM images in Fig. 5.3a-b), with an extended strained region beyond the central pillar clearly visible.

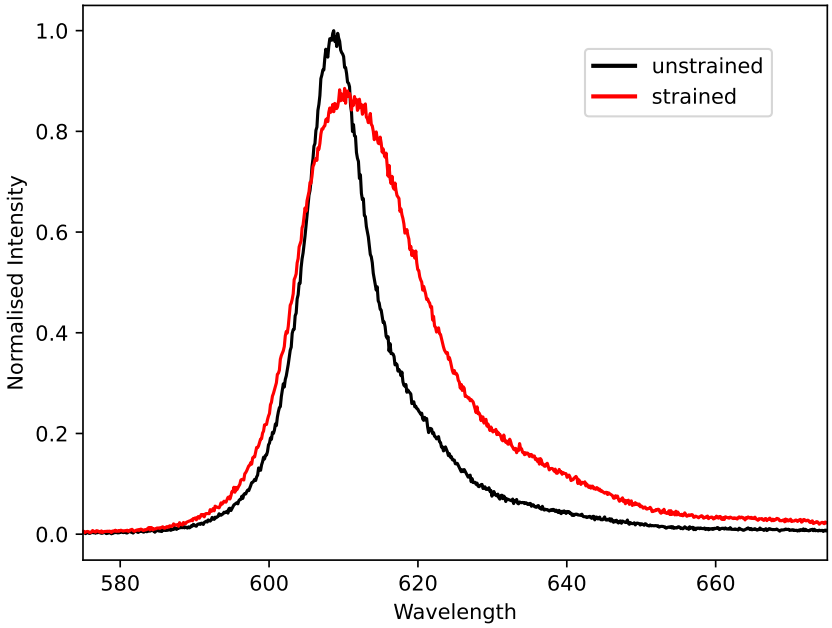

Figure 5.2: Typical PL spectra for WS_2 in strained and unstrained monolayer regions, shown for dry transferred ~250 nm height pillars.

Fig. 5.3 also shows a striking difference between the height profiles of the dry and wet transferred examples, with no obvious suspended region visible in the latter case. This is likely a result of the differences in transfer process, the main candidate being that during dry transfer the flake was forced onto the pillared substrate using a PDMS substrate, which constrained the material as the PDMS was still adhered to the flake throughout most of the process. In contrast, the wet transfer process involved floating the flake on water, then capturing this on a substrate and baking the system. There perhaps exists more opportunity for the flake to relax in this case as the water does not constrain the flake in the same way as PDMS. The sample height in the unstrained region also varied more in the wet

transfer case than for dry transfer, which can be attributed to few-layer island growth during the CVD process producing small areas of increased thickness. This is consistent with the quality of samples not being constant between wet and dry transfer samples due to different growth processes.

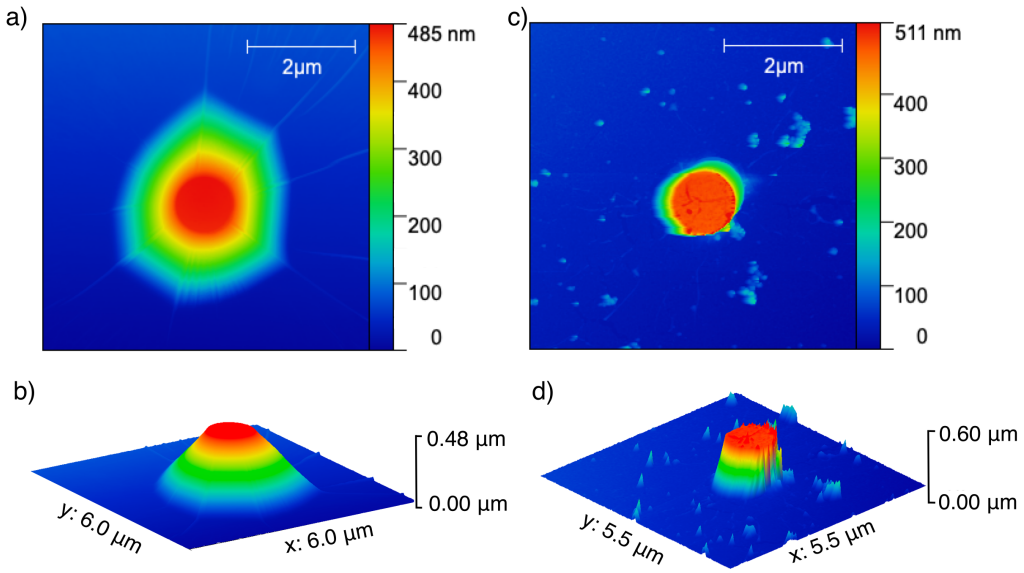

Figure 5.3: Examples of typical AFM images taken from a-b) a dry transfer sample with one strained pillar (top left) and c-d) a wet transfer sample (all pillars covered in monolayer, but minimal strain shown). a) and c) show colour maps, while b) and d) show 3D profiles. Both show ∼500 nm pillar heights.

The difference in profile around the pillars between wet and dry transfer samples is clearly reflected in the differences between wavelength shifts between Figs. 5.5 and 5.6. If the ∼250 nm pillar height case is considered across these figures, the range in wavelength shifts for dry transfer of ∼9 nm is far larger than the equivalent ∼2 nm figure in the case of wet transfer - highlighting a lack of strain within such samples. This effect is also visible in the ∼500 nm pillar height cases, where the equivalent figures are ∼12 nm and ∼2 nm for dry and wet transfer respectively. It is also interesting to note this wavelength range for wet transferred samples changes only minorly across different height pillars - introducing further disparity between the transfer methods. This further suggests

little to no strain was induced by the wet transfer process. There could also be, however, highly localised areas of strain at the edges of the pillars, which would provide a limited signal due to a low fill fraction of the laser spot size. This effect is illustrated in Fig. 5.4, where the high strain region close to the pillar is a fraction of the overall excitation laser beam diameter of 2. These areas would likely not be visible in AFM images due to the rapid change in height in these regions which introduces larger error in the measured height in such regions. A higher objective magnification could be used to further reduce the excitation laser spot size, however this would also require larger integration times due to lower numerical aperture.

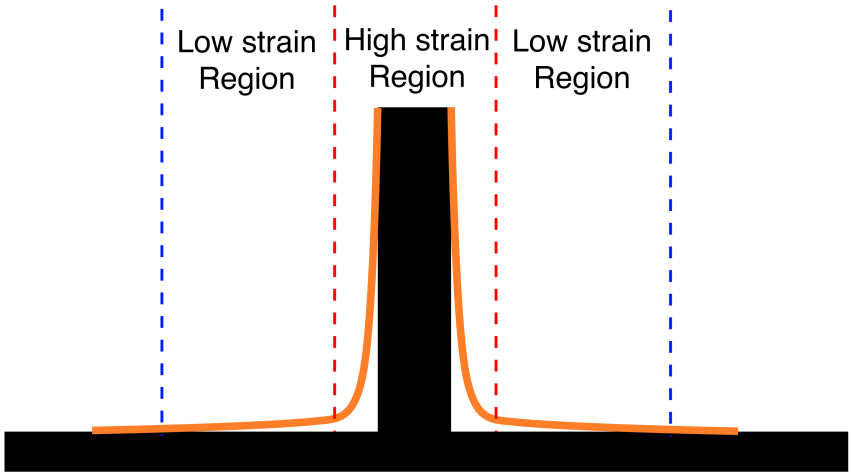

Figure 5.4: Illustration of possible highly localised strain regions which could appear undetected during wet transfer due to limits of AFM and PL spatial resolution. High strain region is shown by red dashed lines and laser spot size is shown by blue dashed lines.

In the dry transferred samples, two pillar heights were probed, ∼250 nm and ∼500 nm. Figure 5.5a-b) shows an example of the PL maps one of these smaller pillars, compared to Figure 5.5c-d), which shows the same for two adjacent pillars for the taller pillar case. The number of pillars did not change results as the pillars are clearly distinguishable due to having dimensions larger the laser spot

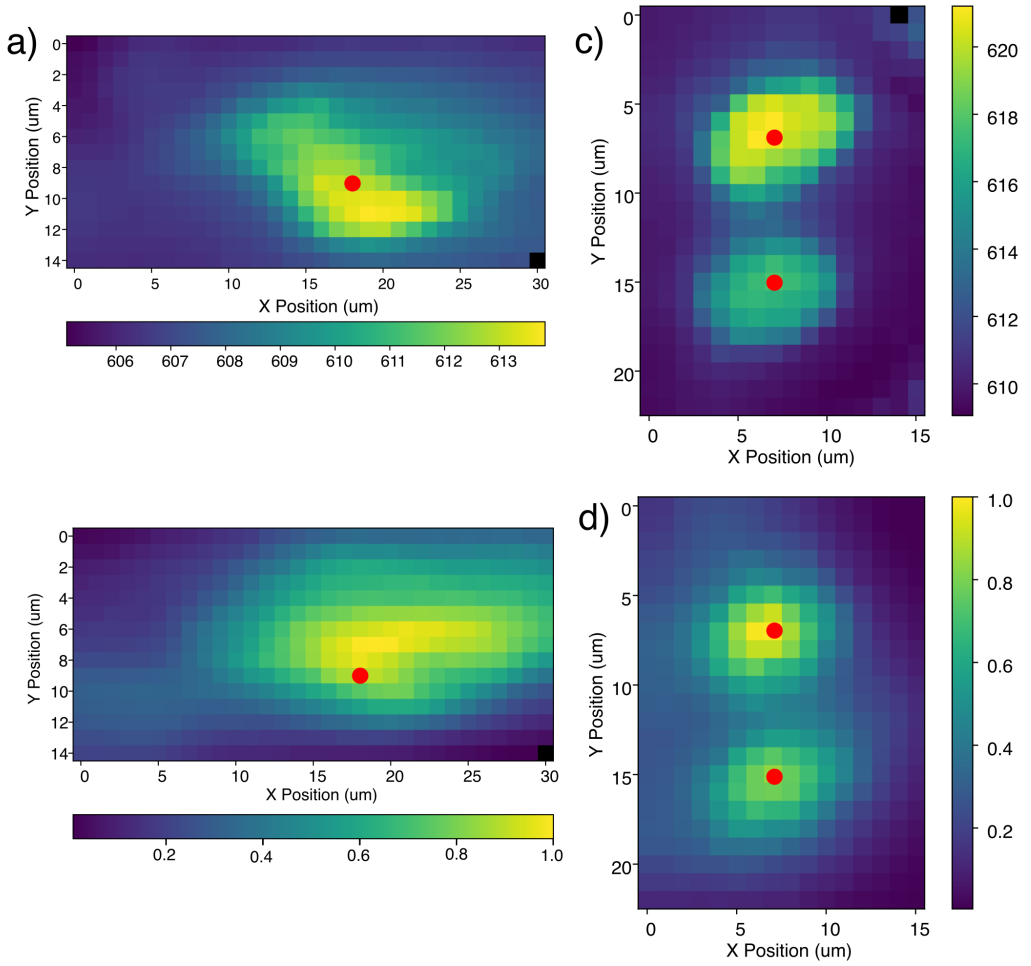

Figure 5.5: 2D PL maps of the surface of dry transferred flakes for a-b) 250nm samples and c-d) 500nm samples. a) and c) show peak wavelength, while b) and d) show integrated intensity. Pillar positions are shown by red dots in a-d)

size and number of pillars in each map was based purely on how many pillars showed strain within a region. Some samples formed cracks around the pillars (confirmed by AFM), making them unsuitable for analysis due to the resulting crystal relaxation in such regions.

Figure 5.5 provides only representative examples of such data as many samples were subjected to such mapping. The areas of maximum strain within these images correspond to the pillar locations. The smaller pillar samples gave an av-

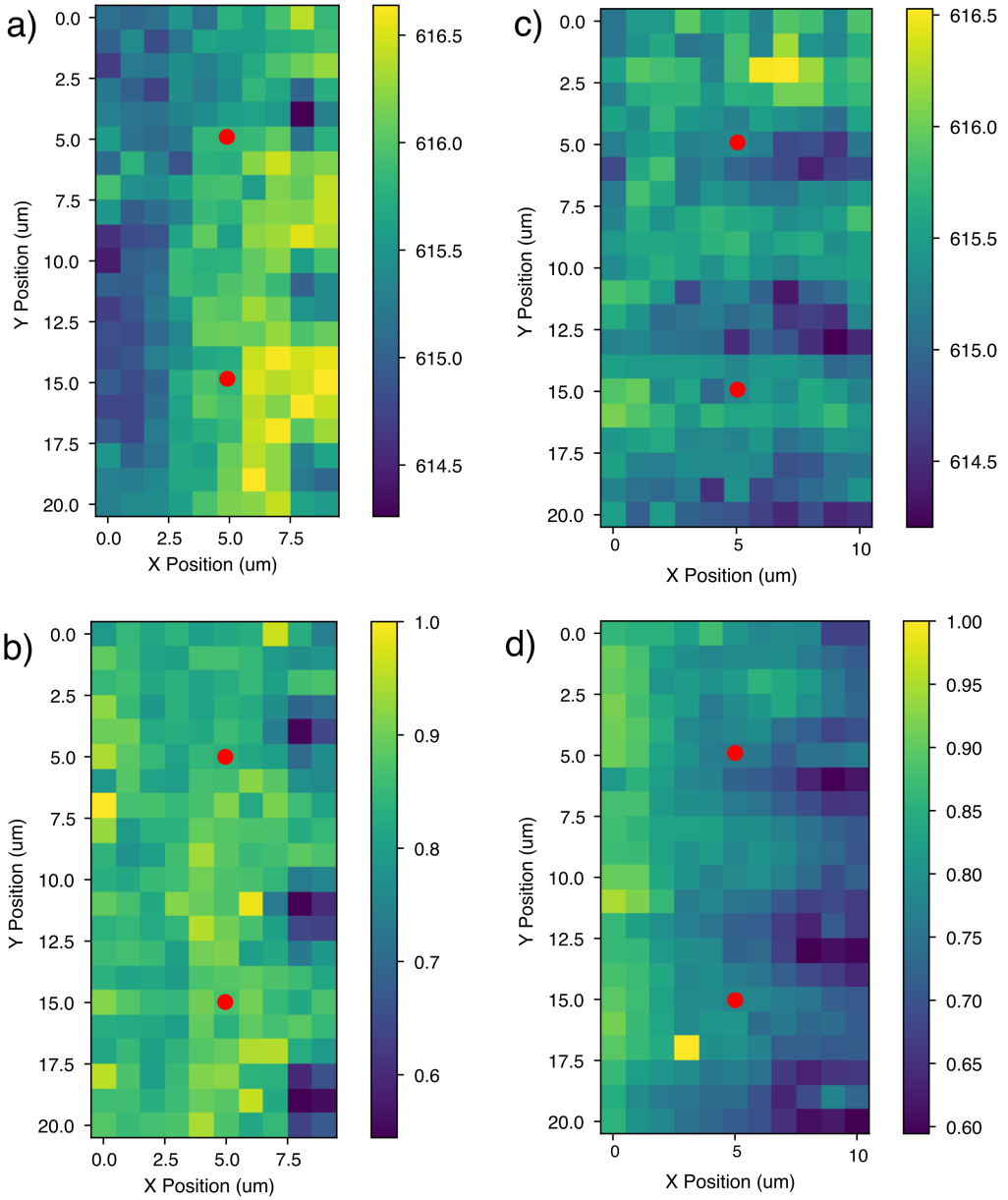

Figure 5.6: 2D PL maps of wet transferred flakes for a-b) 250 nm samples and c-d) 500 nm samples. a) and c) show peak wavelength, while b) and d) show integrated intensity (normalised). Pillar positions are shown by red dots in a-d).

erage wavelength shift of (8.4±0.2) nm while the larger pillar height samples gave an average wavelength shift of (15±2) nm; with uncertainties obtained from repeated measurements via the standard error of the mean. This shows a clear correlation between pillar height and wavelength shift and therefore induced strain.

The larger pillars, however, also showed a larger spread in wavelength shift, as illustrated by the error in the average shift. This is attributed to sample slippage during transfer due to larger forces within the larger pillar samples. If these forces are larger than those keeping the flake adhered to the PDMS, the flake may relax slightly on the PDMS reducing the strain induced by the process.

The gradient of band gap with respect to strain has been determined by Deng et al as ∼50 meV/% [86]. Applying this figure to the dry transferred samples yields approximate strain values of ∼1 % and ∼0.5 % strains for 500 nm and 250 nm height pillars respectively. A point to note is that Fig. 5.5 shows non-circular strain fields, in contrast to the AFM images in Fig. 5.3, which is likely due to strain caused by creases localised along one dimension (visible as thin lines in Fig.5.3a)). As there is evidence for slipping between the substrate and flake, this suggests the adhesion strength between substrate and flake is the limiting factor in achieving higher strains, as strains of 0.5-1 % without breaking should be easily possible - with strains approaching 10% having been reported in TMDs [116]. Further work would be needed to confirm this comparison, however, as the latter figure is for maximum strain whereas this work focuses on an averaged effect, thus localised areas of higher strain could still exist - hidden by the spatial resolution of the PL measurements.

5.4 Discussion

Exfoliation remains an unscalable method, thus it is crucial to develop a method of inducing strain using a more scalable method, for example for CVD grown flakes, if such technology is to be viable for further application. Results suggest dry transfer introduced far higher strain levels than for wet transfer, however the possibility exists of localised strain introduced within wet transferred samples on a length scale smaller than the spot size used. Further work with reduced probe and step size could shed light on this, however any strain discovered would be present over a limited area, thus may have limited applications.

One potential application for strain engineering within 2D materials is in single photon emission. As the strained area can be highly localised this can provide a potential well for bound excitons which then have a well defined emission wavelength. Such localisation can, therefore, lead to single photon emission, which could be present in the samples in this work but would not be visible at room temperature [117]. Further experiments at cryogenic temperatures would be necessary to confirm any single photon emission in this system, as the signal from such systems is a well-defined low-width peak in the PL spectrum, which is undetectable at room temperature due to broadening mechanisms.

5.5 Conclusion

The results suggest that the wet transfer of CVD grown monolayer was not an effective method for implementing strain using nanopillars. This is contrary to dry transfer of exfoliated flakes, which readily introduced detectable strain within such systems. Furthermore, the wavelength shift introduced in dry transferred samples was (8.4±0.2) nm and (15±2) nm for ∼250 nm and ∼500 nm height pillars respectively, meaning a larger wavelength shift was possible for larger pillar

heights, however the spread was larger. The spread was taken as the standard error of the mean from a range of samples. This suggests ∼250 nm pillars are more reliable at introducing a specific strain, whereas ∼500 nm pillars can introduce larger strains at the expense of repeatability. The wavelength shifts introduced in dry transferred flakes correspond to strain levels of ∼0.5 % and ∼1 % for ∼250 nm and ∼500 nm height pillars respectively when correlated to the estimated band gap change from DFT results by Deng et al [104].

Chapter 6

Surface defect engineering via UV-Ozone and 1,2-dichloroethane treatments [†]

6.1 Introduction

Engineering defects within the surfaces of materials can be a useful route to varying the optoelectronic properties of materials. One method for defect introduction is via chemical treatment. For example submersion in 1,2-dichloroethane has recently gained traction as a method for doping with Cl in TMDs [118]. However the optical effects of introducing such defects is an open question.

Chlorine-sulfur substitution defects were investigated via DFT calculations to investigate potential changes to the density of states which could cause changes in the optoelectronic properties. Chlorine contains five p electrons in its outer

[†]Part of this chapter has been adapted from work that is published: Fahrettin Sarcan, Alex J. Armstrong, Yusuf K. Bostan, Esra Kus, Keith P. McKenna, Ayse Erol, and Yue Wang. "Ultraviolet-Ozone Treatment: An Effective Method for Fine-Tuning Optical and Electrical Properties of Suspended and Substrate-Supported MoS_2" Nanomaterials 2023, Vol. 13, Page 3034, 13(23):3034, 11 2023 [13].

orbitals compared to four for sulfur meaning it has potential to be a good n-type dopant in the MoS_2 system, which would introduce defect states near the conduction band minimum. Although MoS_2 is naturally an n-type material, tuning to further increase the charge density of electrons could also be advantageous for some applications, enabling more efficient charge transfer. Doping within semiconductor devices is pivotal to their operation in many circumstances, for example transistors require areas of both p and n type doped material.

A convenient method for surface modification is UV-ozone treatment. Such treatment involves irradiation of oxygen with ultraviolet (UV) light, dissociating O_2 into triplet oxygen, which can then react with O_2 to form O_3. UV also dissociates O_3 into O_2 and singlet oxygen - the latter being highly oxidizing and resulting in high reactivity with organic compounds. This reactivity with organic compounds, while being relatively inert with respect to interaction with inorganic compounds such as silicon, makes the technique ideal for removal of organic residue on inorganic substrates, hence it is often used in substrate cleaning [119]. The forming of polar bonds involving oxygen on surfaces during this process also increases hydrophilicity of surfaces enabling the use of the technique for surface modification purposes, for example to increase attraction between a substrate and flake during dry transfer, increasing transfer success rate. The reactive species generated by the UV-ozone process can also interact with materials in other ways, potentially causing changes in their properties by introducing defects [120].

P-type doping has become a highly sought after property within the field of 2D materials, as both n- and p-type materials are necessary in a transistor. Both would, therefore, be necessary in any all-2D transistor, however the latter is generally more difficult to achieve. In the case of MoS_2, there is evidence to suggest the native structure after growth is n-type doped, with p-type doping requiring specialised methods to achieve [121]. For photonic applications, it is

also important the PL spectrum maintains a high intensity - dramatically reducing intensity would result in low efficiency for any applications involving light. Some progress has been made in this area, for example doping with Nb during CVD growth has been shown to reduce the native n-type behaviour in MoS_2, while increasing the PL intensity and also blue-shifting the PL spectrum [122]. Phosphorous ion implantation has also been shown to reduce n-type behaviour within MoS_2, however the effect on PL remains unclear for this process [123].

Usual methods for doping bulk crystals involve introducing dopants during the crystal growth process. This forces a change in structure, which has negligible effect in a three dimensional (3D) crystal. However in the case of a 2D crystal this is not appropriate - the large surface area to volume ratio renders the crystal properties extremely sensitive to structural changes. Ideally these structural changes can be limited by introducing doping at the post-growth stage, when global restructuring of the lattice is far less likely. UV-ozone treatment is presented as a potential method to achieve this.

Evidence for p-type doping in UV-ozone treated four layer MoS_2 has been observed experimentally but the mechanism causing this is currently an open question [13]. The experimental work motivating these calculations initially focused on how treatment time affected PL intensity for different numbers of layers to ensure a limited reduction in PL (Fig. 6.1). For suspended MoS_2, the optimum treatment time was four minutes, maintaining a consistent PL intensity for this treatment time, however a consistent decrease in intensity was measured when a Si_3N_4 substrate was included. Higher layer numbers were found to have a more stable PL intensity with increasing treatment time. As an example with stable electronic properties and PL, four layer MoS_2 was chosen to fabricate a transistor, which was electrically characterised to determine the level of p-type doping induced by UV-ozone treatment for different treatment times. The results of this

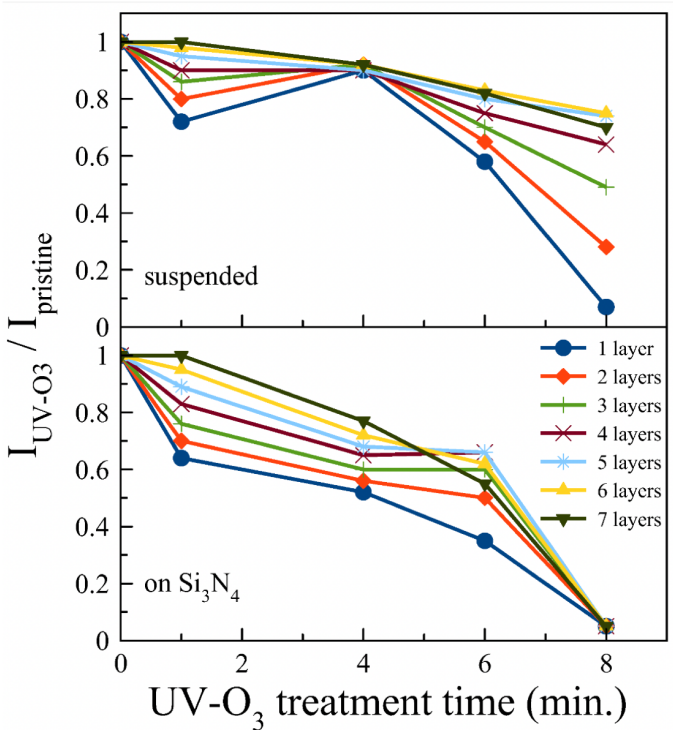

Figure 6.1: PL intensity ratio between treated and untreated MoS_2 with varying treatment times, shown for different MoS_2 layer numbers from 1-7. Results are shown for both MoS_2 on a Si_3N_4 substrate and suspended MoS_2 [13].

characterisation are shown in Fig. 6.2. It should be noted that this characterisation was undertaken by other collaborators but is included here to provide motivation for subsequent DFT calculations. Fig. 6.2b shows a clear transition from negative to positive dominant charge carriers as treatment time is increased, with this transition occurring between 4 and 6 minutes of treatment. This is illustrated by the change in sign of the gradient of drain current with respect to gate voltage. In Fig. 6.2d drain current with both positive and negative bias can be seen to reduce above 6 minutes of treatment time, suggesting that both electron and hole densities are decreased above this limit. The p-type behaviour induced by the UV-ozone treatment process motivated further investigation via DFT calculations to identify possible charge trapping defects causing such changes to material properties.

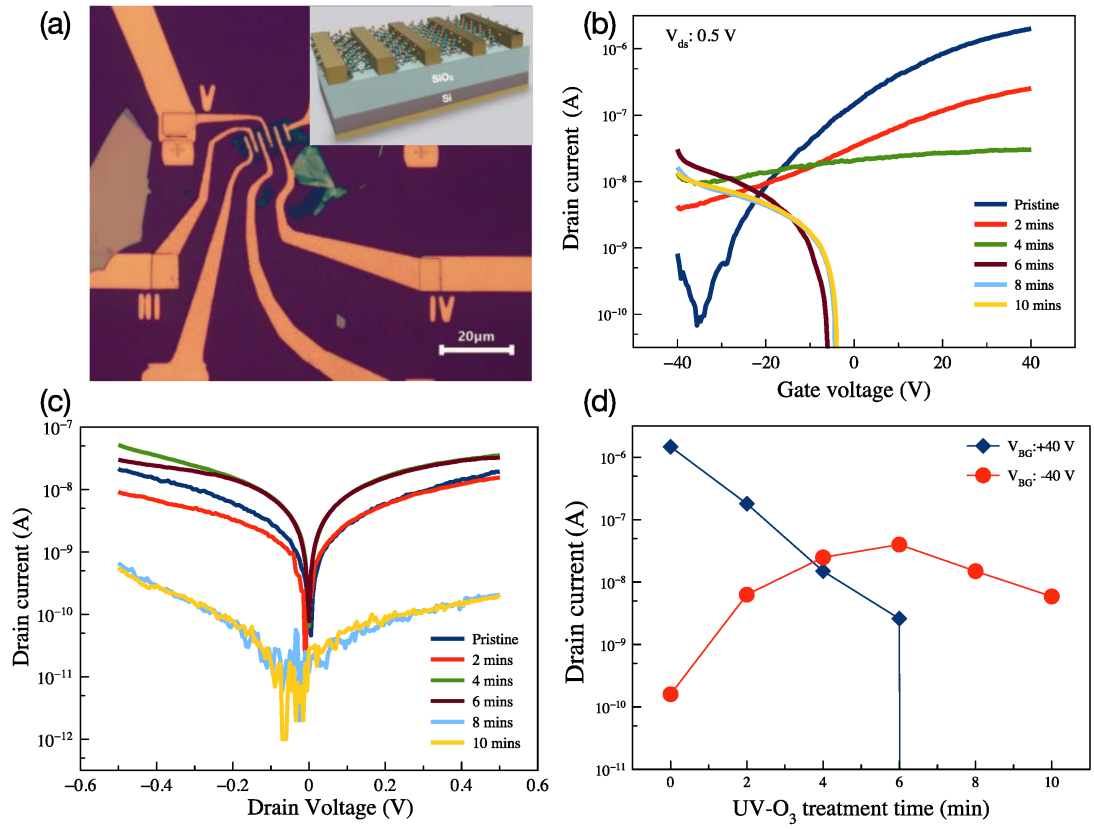

Figure 6.2: a) Optical microscope image with 20 μm scale bar and illustration (inserted) of the MoS_2 field effect transistor, drain-source current as a function of (b) applied gate voltage, c) applied drain-source voltage, and d) UV-ozone treatment time [13].

6.2 Method

Density functional theory (DFT) calculations were undertaken to investigate which oxygen species present during the UV-ozone treatment could cause p-type doping via charge trapping in defect states introduced into the band gap close to the VBM. Three species were identified: atomic oxygen (O), molecular oxygen (O_2) and ozone (O_3). Sulfur substitutional defects involving these species, as well as surface adsorption onto various symmetrically inequivalent high symmetry sites were considered as potential charge-trapping defects. Preliminary geometry optimisations were undertaken with the PBE functional, including Grimme's D3 van der Waals corrections [48] to determine the lowest energy adsorption site and

adsorbate bond orientations for the adsorption calculations.

Further calculations, and all calculations for substitution defects, were undertaken using the HSE06 functional with D3 corrections, ensuring more accurate energy levels above the valence band to fully capture any charge trapping levels. These calculations were initially optimised with an extra electron added to capture the geometry of the charged structure, then reoptimized for the neutral case. This enabled Bader charge analysis [124] to be conducted on both neutral and charged cases to identify any areas where the charged case differed greatly at the defect site, which would be indicative of charge trapping. To reduce the defect density and prevent bands forming from the defect levels, the unit cell used was double the size of the primitive cell in x and y directions, while all defect simulations were undertaken on a 4-layer system. Calculations were also undertaken for 1-5 layer and bulk pristine MoS_2 to confirm the layer dependence of the band gap. These were optimised using the PBE functional with D3 corrections to determine an initial structure and wavefunction, then further optimised using HSE06 with D3 corrections to obtain the final structure. Band calculations were then performed using HSE06 [44] with D3 corrections, with the high symmetry k path generated by the sumo package [89]. The band structure for the 4 layer system was also necessary to determine where the defect levels were relative to these bands.

All DFT calculations were undertaken using a plane wave basis set, as implemented in the VASP package [88]. A gamma centred Monkhorst-Pack grid of 2x2x1 k points was used to sample the Brillouin zone for all calculations, which were converged to a force tolerance of 0.01 eV/Å. Ideal values of D3 parameters for HSE06 are still an open area of research and could therefore not be sourced from literature, so this study used parameters quoted for the related hybrid functional PBE0 for calculations. Version 5.2 PBE plane wave potentials (PAW) were

used for all calculations, with plane wave cutoff value of 520 eV.

Defect formation energies were also calculated for each oxygen defect as a function of the chemical potential of sulfur to determine which defects were most stable under different sulfur conditions. These energies were calculated as:

$$E_f^{def} = E^{def} - E^{bulk} - \sum_i n_i \mu_i \tag{6.1}$$

Where E_f^{def} is defect formation energy, E^{def} is the energy of the defected system, E^{bulk} is the energy of the bulk, n_i is the number of atoms removed of species i, and μ_i is the chemical potential of species i.

Both sulfur rich and sulfur poor limits were considered at a constant oxygen chemical potential – with only two points necessary due to the clear linear nature of these energies with respect to one chemical potential. These limits were defined as the sulfur chemical potential when $\mu_s = \frac{1}{2}E^{\mathrm{S_2}}$ and $\mu_{Mo} = E^{\mathrm{Mo}}$ for the sulfur rich and sulfur poor cases respectively, as either of these conditions uniquely defines both μ_{s} and μ_{Mo} according to:

$$E^{\mathrm{MoS_2}} = \mu_{\mathrm{Mo}} + 2\mu_{\mathrm{S}} \tag{6.2}$$

All energies used were calculated at PBE+D3 level of theory and formation energies for O_2 defects were halved to calculate energies per oxygen atom and ensure these energies are comparable between the different systems.

Defect energy levels were defined as the lowest lying state above the valence band with a non-negligible weight attributed to the defect site in the neutral charge case. To ensure the energies were consistent between systems despite any systematic shifts in VBM and CBM energies, density of states were calculated using sumo and energies aligned to the pristine surface using the lowest energy molybdenum core state as a reference [89].

Partial charge density from states within the band gap region were calculated for chlorine defects, which were then visualised in VESTA using an isosurface level of $1x10^{-3}eÅ^{-3}$ [75].

6.3 Results

6.3.1 Band gap variation with number of layers

The layer dependence of band gap in MoS_2 is shown in Fig. 6.3 both experimentally and calculated by DFT. It should be noted that the experimental work in this figure was undertaken by collaborators [13]. The comparison between calculated results and experiment provides evidence for validity of the DFT model for this system. The DFT calculated results in Fig. 6.3a show both direct and indirect transitions, however both energies are not accessible experimentally, so Fig. 6.3b shows only the lowest energy of these transitions. This is because the lowest energy transitions can be easily probed optically and identified from the peak in the PL spectrum, but for other transitions it can be difficult to determine which optical transitions correspond to different features within the PL curve. The experimental data should be equal to the calculations for the indirect transition, except in the monolayer case, for which the direct transition should be synonymous with the experimental data. Taking this into account, the trend of the two curves is visibly consistent, however the calculated values are larger than experiment by a constant value of ∼0.2 eV. This systematic difference between experiment and theory can likely be attributed to the exciton binding energy, which is not taken into account by standard DFT, however another contribution to this is the inherent overestimation of band gap by the HSE06 functional. Fig. 6.3a shows a transition from an indirect to a direct band gap when the number of layers is reduced to one. The model was not extended to include 6

and 7 layer systems to further compare with experiment due to the excessive computational cost associated with these larger systems and the substrate effect was excluded from calculations for the same reason. The bulk limit for both the direct and indirect transitions were calculated, shown by dashed lines, to represent an approximation to the many layer case. The indirect transition can be seen to be highly layer dependent in contrast to the direct transition which stays approximately constant in energy with a change in layer number (discussed further in chapter 4). Fig. 6.4 compares calculated band structures of the monolayer and bulk systems, illustrating the shift from direct to indirect gap with increasing layer numbers. This is also consistent with other calculations in the literature [125–127].

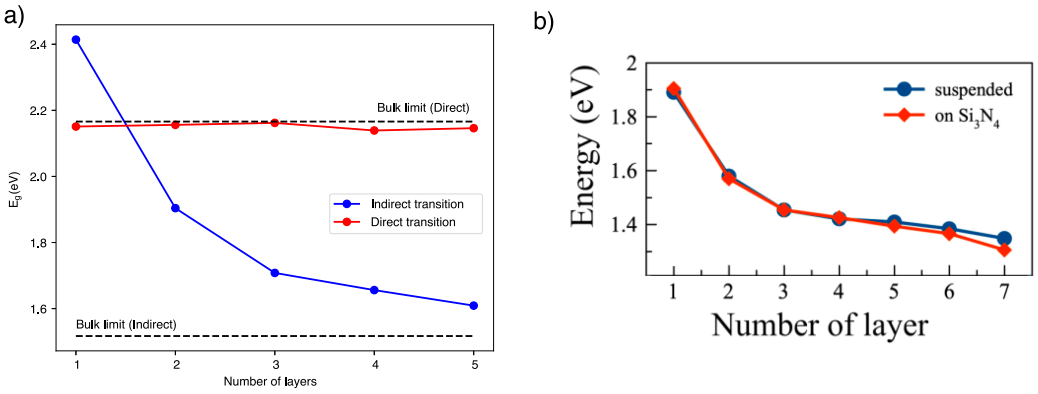

Figure 6.3: Band gap transition energies in MoS_2 with a) DFT electronic band gaps with both direct and indirect transitions shown, together with the calculated bulk limits for these parameters and b) experimentally derived optical band gaps from PL data. It should be noted that b) is adapted from work carried out by other collaborators, taken from published work [13]

6.3.2 Oxygen defect states

Both substitution and adsorption of O_3 resulted in dissociation into an O defect and a free O_2 molecule in the vacuum gap at the PBE level, so this was not investigated further as the structure would be the same as for O defects. From

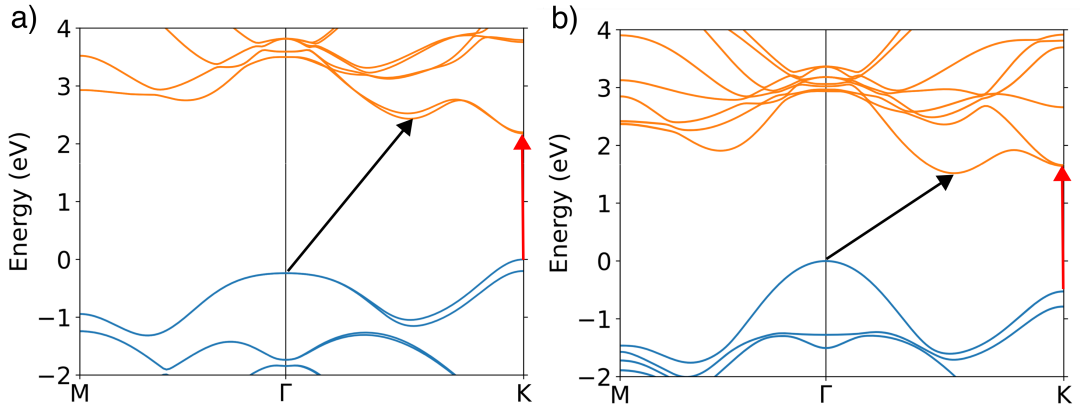

Figure 6.4: DFT calculated band structures in a) monolayer and b) bulk MoS_2 systems. Direct and indirect transitions marked by red and black arrows respectively.

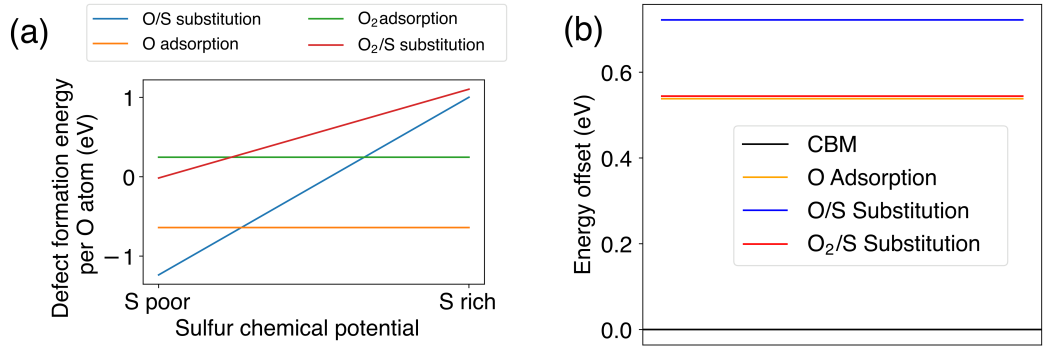

Figure 6.5: a) Defect formation energies for O and O_2 adsorption and S substitutional defects as a function of sulphur chemical potential; b) Defect energy level offsets for each stable defect mechanism, with respect to the conduction band minimum (CBM) in the pristine 4L-MoS_2 system.

Fig. 6.5a) it can be seen that the two most stable defects are those involving single O atoms, with sulfur substitution becoming the most stable only under sulfur poor conditions because of a higher density of S vacancies under these conditions, reducing the energy barrier to these defects forming. Under most conditions, single O atom adsorption has the highest stability.

Further analysis is displayed in Fig. 6.5b), showing the calculated energy levels introduced by the various defects relative to the CBM. All defect levels

were found to be above the CBM by more than 0.5 eV, suggesting no charge trapping would be introduced by any of these states, which would require states located within the band gap.

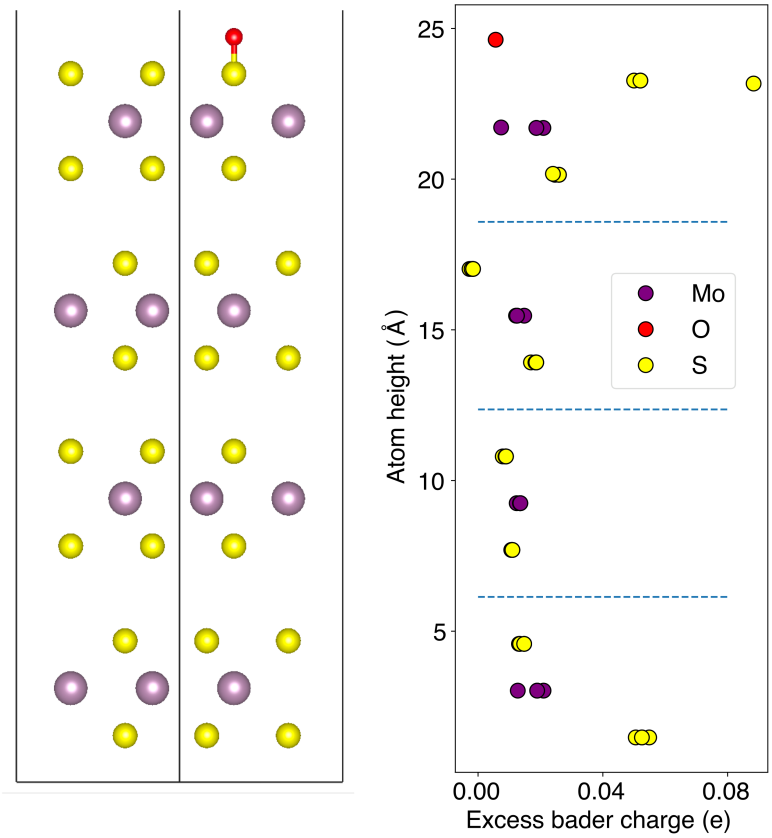

Figure 6.6: Excess Bader charge for each atomic site (right), with sites aligned vertically with unit cell (left), for the O adsorption case. Excess Bader charge was calculated as the charge difference at each site between the neutral system and the system with a single electron added.

A lack of charge trapping effects is further corroborated via explicitly calculating the difference in charge attributed to atomic sites between the neutral system and the system with an extra electron added (excess Bader charge). The findings were similar for all defect types, hence only one example is shown in Fig. 6.6, namely single O atom adsorption. This was chosen due to its higher stability compared to other defects under most conditions calculated. If non-negligible charge trapping were to occur, the excess Bader charge would be a reasonable fraction of

that of an electron, with ideal trapping representing a charge of 1e. Conversely, Fig.6.6 shows a maximum of ∼0.08e - indicating no charge trapping within the system. This is not unexpected as only freestanding MoS_2 was modelled, which did not show p-type doping experimentally. Inclusion of the substrate within the calculations could change these results but was too computationally expensive to calculate in full using the hybrid theory level necessary for these calculations.

The density of states (DOS) for O atom adsorption is shown in Fig. 6.8, which further highlights no differences between the two systems within the band gap region - indicating no defect states within the band gap. Differences in the DOS clearly exist outside of the band gap region, indicating defect states do exist, however their placement with respect to the band gap would not cause charge trapping effects. Only one defect is shown, as the key result of no defect states in the band gap was common across all defects considered. The optimized structures for calculated defects are shown in Fig. 6.7.

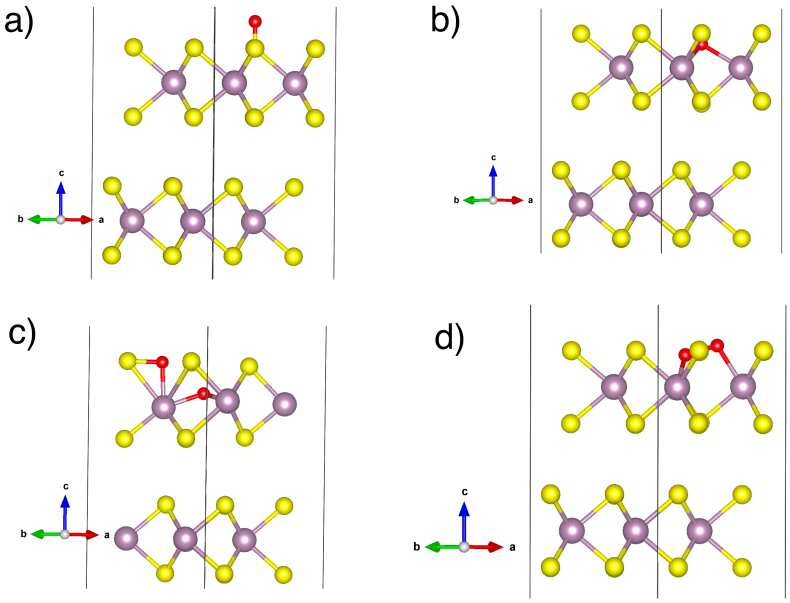

Figure 6.7: Structures of defects calculated, showing a) O adsorption, b) O substitution with sulfur, c) O_2 adsorption and d) O_2 substitution with sulfur

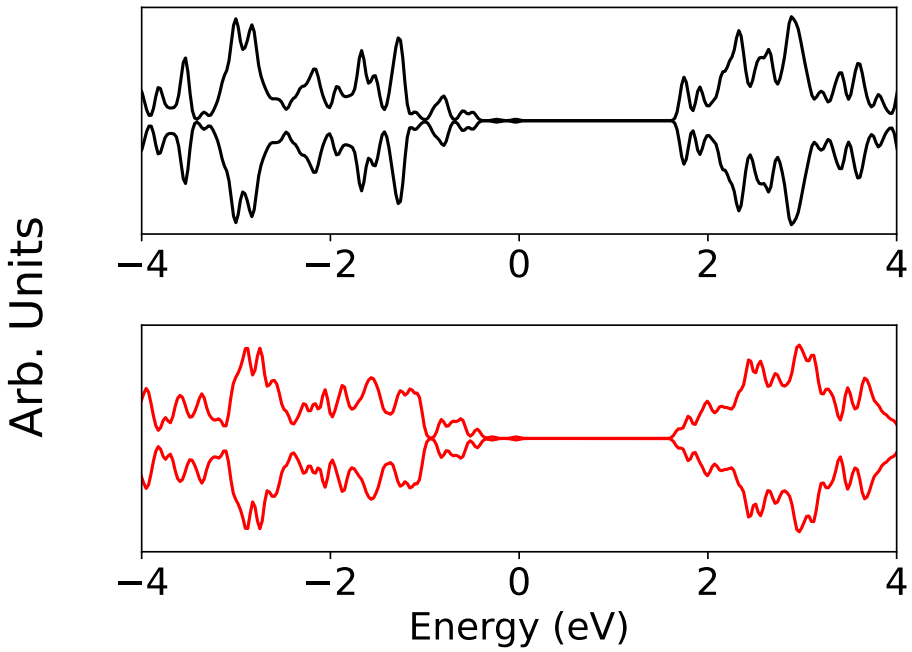

Figure 6.8: DFT calculated density of states for pristine 4L MoS_2 (top) and 4L MoS_2 with an O atom adsorbed on the surface (bottom). Spin up and down shown above and below x axis respectively.

6.3.3 Chlorine defect states

While Oxygen defects were not found to result in defect states within the band gap region, the story is different when a chlorine-sulfur substitution defect is considered. The calculated density of states for this system is shown in Fig. 6.9.

It can be seen from Fig. 6.9 that the introduction of a chlorine atom results in defect states in the band gap region. The shifting of the Fermi level to the top of these states suggests that these states represent the donation of an electron from chlorine to the system, meaning it could be a candidate for n-type doping. These states are not well localised in energy - however this is likely due to computational limitations, as a small unit cell only four times the size of the primitive cell was used. This relatively small unit cell can result in more diffuse states due to interaction with neighboring unit cells. The chlorine states coincide with the

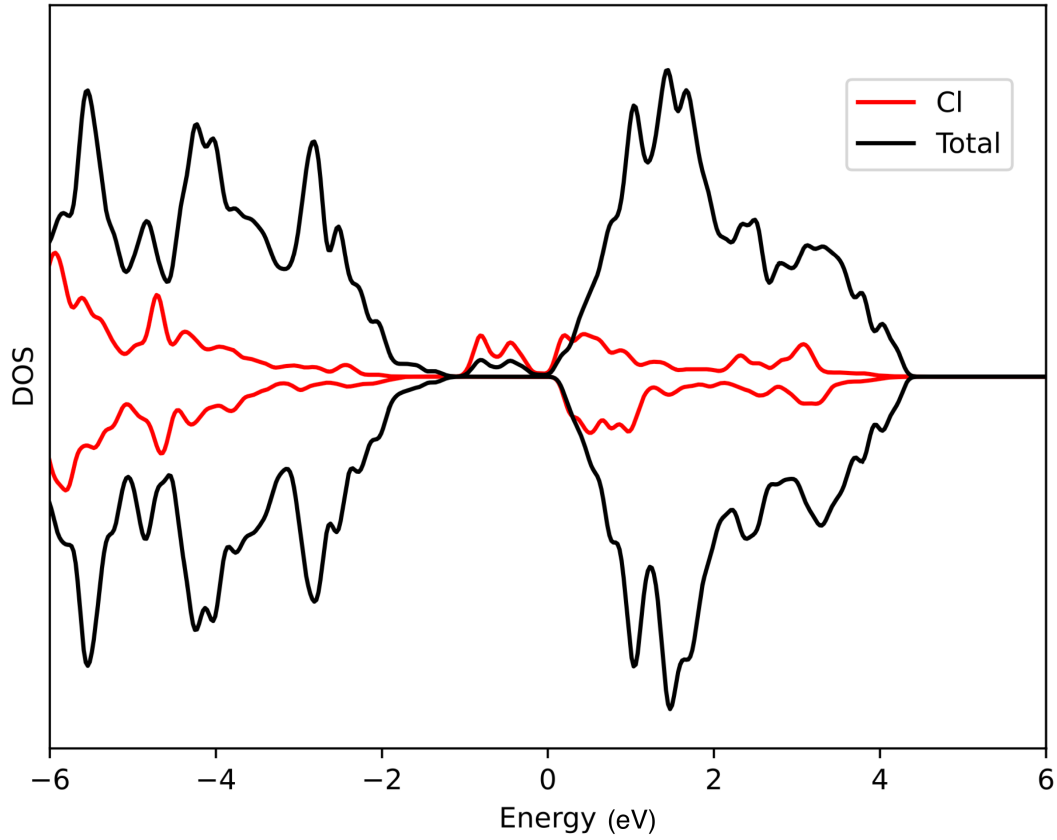

Figure 6.9: Density of states for chlorine substitution with a sulfur atom, as well as the partial density of states for chlorine (spin up and down shown above and below x axis respectively). Intensities of chlorine states are multiplied by 15 due to low intensity compared to other atoms.

energies of defect states shown in the total density of states, corroborating that these states are a result of chlorine defects. Fig. 6.9 also shows some chlorine states around the CBM region, which helps to explain the small decrease in energy of the conduction band minimum compared to the pristine system.

The potential for n type doping is corroborated by preliminary experimental evidence by collaborators, as shown in Fig. 6.10. This shows the drain-source current in transistors fabricated with four layer MoS_2 as a function of gate voltage, which is shown to increase when the material was soaked in 1,2-dichloroethane for increasing times up to an hour. The variation from this trend at higher treatment times could be due to reduced charge transport efficiency at higher

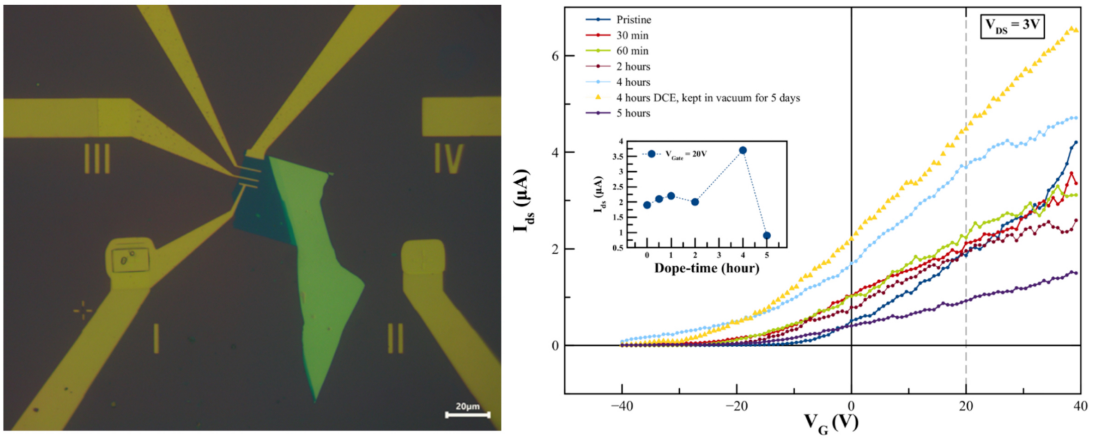

Figure 6.10: Figure showing a fabricated four layer MoS_2 transistor (left). Source-drain current is shown as a function of gate voltage for different 1,2-dichloroethane treatment times. This figure was produced by our collaborators from Istanbul university, lead by Fahrettin Sarcan.

defect densities - with further work necessary to determine the origin of this effect.

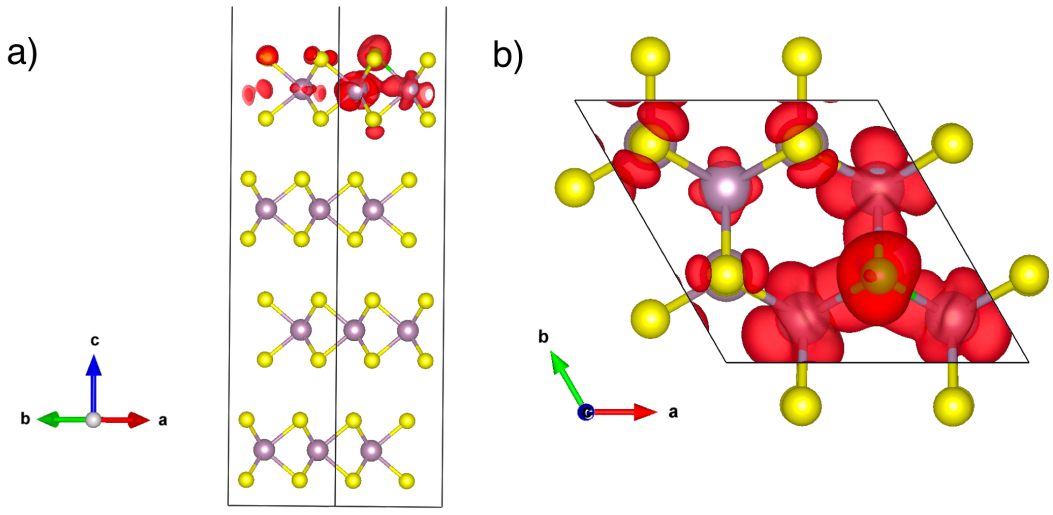

Figure 6.11: Charge isosurface from four layer MoS_2 with one sulfur atom substituted with chlorine. Only states within band gap region (energies between -1.1 and 0, relative to the Fermi energy). An isosurface level of $1x10^{-3}$ $eÅ^{-3}$ is used. a) and b) show the visualization from different directions.

The charge isosurface including only states within the band gap region is visualised in Fig. 6.11. Here the charge can be seen to be delocalised across the

unit cell which would likely result in interaction with neighboring cells. The diffuse nature of this charge distribution provides an explanation for the chlorine states being low intensity in Fig. 6.9, despite defect states having a larger intensity. These states are not all attributed to chlorine, as they are not all spatially localised near the chlorine atom.

6.4 Discussion

The layer dependence data could have been improved by including the Bethe-Salpeter equation to calculate the exciton binding energy and improve the data with respect to experiment, however this would increase computational cost. The formation energies were calculated with a constant oxygen chemical potential of half the energy of an oxygen atom. This could also take on a range of values which would result in a systematic shift of the formation energies and could result in O_2 defects becoming stable under some conditions, for example if the O_2 defect was mediated by an incident O_3 atom, the relevant chemical potential would be $\frac{1}{3}$ the energy of an O_3 molecule. The relevant chemical potentials for incident O, O_2 and O_3 were calculated as -1.5 eV, -4.9 eV and -4.5 eV respectively, to give an idea of the magnitude of this effect. As the O_2 defects would still be higher in energy than the O defects they would likely be short lived, decomposing to the lower energy defect so would not be relevant for this study. These short-lived defects could however be relevant for providing mechanisms to form O defects. As these calculations found no evidence for charge trapping in suspended MoS_2, these calculations should ideally be undertaken with a substrate included to confirm how this changes the carrier dynamics. This is considered future work due to the difficulties involved: large unit cells would be required for such calculations to effectively model the interface as lattice mismatch at such surfaces can

result in relaxation over distance far larger than the primitive cell. A potential way to further investigate the substrate effect would be to hypothesize some specific mechanisms for charge trapping induced by a substrate and modelling these rather than directly including the substrate within the calculation. The p-type doping effect of UV-ozone treatment has potential in gas sensing applications. For example recent research proposes a selective gas sensor for volatile organic compounds [128]. Here, UV-ozone treatment is used to increase the selectivity of polar compounds by changing the electron density.

Chlorine substitution was found to introduce states within the band gap region, suggesting it could be a good candidate for an n-type dopant. However these states are quite dispersed possibly as a result of a relatively small unit cell. Further investigation including larger unit cells could confirm the effect of the defect density on the dispersion of such states, which would be expected to reduce. Inclusion of excitonic effects in the model would also be necessary to predict any PL spectrum changes from such defects.

6.5 Conclusion

Calculations of band gap variation with number of layers confirmed a decrease in band gap energy with increasing layer number. This provides justification for the validity of the DFT model for electronic effects within the system when compared to experimentally measured band gaps for such systems found via photoluminescence spectroscopy. The oxygen defect calculation results suggest that no significant charge trapping or PL peak energy shift should be expected from the substitution and adsorption of O, O_2 and O_3 on the surface of a suspended MoS_2 flake. The charge trapping effect observed in experiment is likely to originate from the substrate interaction with the sample. However calculations to

confirm this are considered future work. Chlorine substitution with sulfur was also investigated, and found to donate an electron to the system with defect states introduced into the band gap region, which explains the n-type doping effect experimentally demonstrated in devices. This research represents a further step towards understanding the role of defects in controlling the optoelectronic properties of MoS_2 and is likely to apply similarly to other TMDs, which is necessary if devices using such technology are to be realised.

Chapter 7

Edge defect engineering in WS_2

7.1 Introduction

WS_2 is a 2D material that has attracted research attention in recent years. It has the same hexagonal structure as MoS_2, common to transition metal dichalcogenides and hence also exhibiting similar properties to other materials of this categorisation. Similar to the MoS_2 band structure detailed in chapter 4, WS_2 also has a layer dependent band structure changing from an indirect to a direct band gap as the number of layers is reduced to monolayer [110]. Chapter 1 discusses defects in such materials and how they can introduce states within the band gap, a well established phenomenon. A particularly interesting type of defect within 2 D materials is edge defects which comprise of a termination of a 2D material along a particular direction. This disrupts the structure from the infinitely repeating bulk structure to introduce relaxations at these edges and changing the electronic properties of the material. These terminations can exist along different crystallographic directions, the obvious candidates in a material with hexagonal symmetry such as WS_2 being termination along the armchair and zigzag directions.

Edge defects along these directions have been found to heavily modify the electronic properties, with such effects highly directionally dependent. For the example of WS_2, armchair terminations have been shown to cause a reduction in band gap via the introduction of defect states within the band gap. In contrast, zigzag terminations have been shown to introduce many states within the band gap, resulting in a metallic electronic structure and ferromagnetic order. While armchair and zigzag direction edge defects are covered in the literature, the effects of intermediate directions are completely unexplored [129–131]. These different edge types are illustrated in Fig. 7.1, which highlights how a termination between edge and armchair directions can have both armchair and zigzag character. This combination of zigzag and armchair edges is highlighted in Fig. 7.2, which shows a scanning tunneling microscopy (STM) image of a graphene nanoribbon including edges with both armchair and zigzag character.

The intermediate direction termination in Fig 7.1c, for example, can be viewed as an armchair termination (blue) with zigzag direction 'kinks' (red). Varying the termination direction can, therefore, be thought of as varying the density of such kinks. However, this does not mean a direct sum of zigzag and armchair states, as these kinks could cause a relaxation of atoms around them, with overlapping states from atoms in the zigzag and armchair regions forming slightly different states than the summation of the individual states. This could be a useful effect to fully understand because experimentally prepared edges are unlikely to be fully armchair or zigzag in character and likely to include such defects. Investigation of such effects could, therefore, provide a better description of experimentally produced edge defects. The investigation of these kink defects via DFT calculations is the main focus of this chapter.

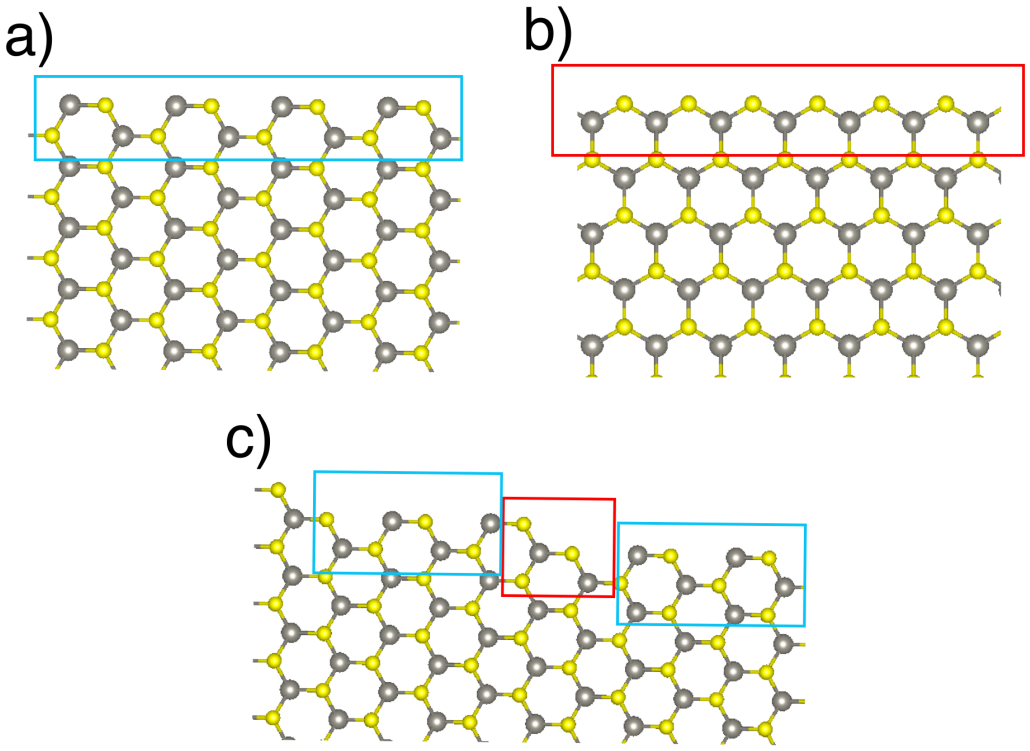

Figure 7.1: Illustration of different types of edge defects in WS_2, showing terminations along a) the armchair direction, b) the zigzag direction and c) an intermediate direction. Armchair and zigzag edges are highlighted in blue and red respectively.

7.2 Methods

Infinite WS_2 monolayer sheets were initially modelled, optimizing both atomic positions and lattice parameters to generate a baseline for comparison to edge calculations, referred to here as 'bulk' calculations. These bulk cells were also used to construct unit cells for edge calculations to ensure consistent lattice parameters between the systems. A transformation of lattice vectors to a conventianal cell was necessary to construct armchair direction terminations, whereas zigzag terminations were constructed using the primitive cell. To enable periodic boundary conditions to be used to model edges, nanoribbons were modelled including two edges per unit cell with a vacuum gap of 10 Å. DFT calculations

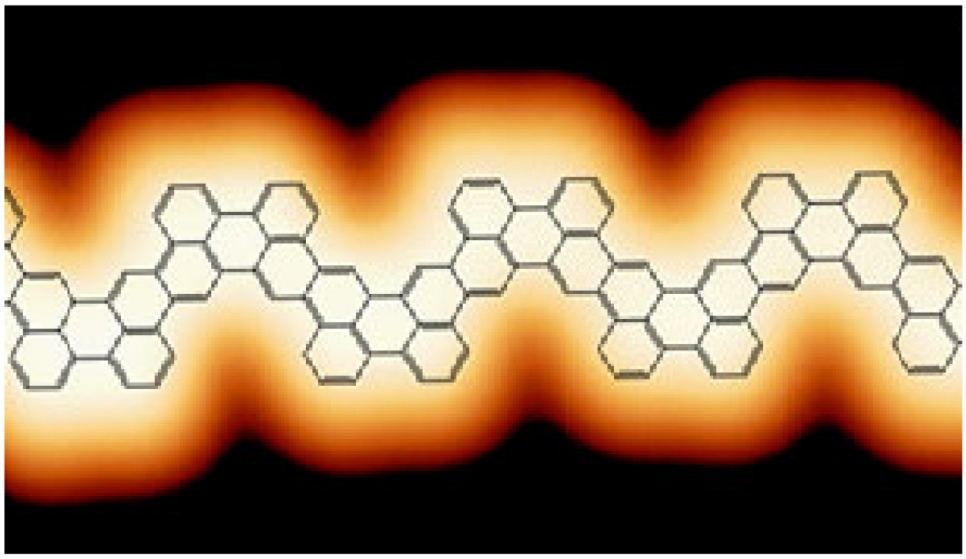

Figure 7.2: Scanning tunneling microscopy image of a graphene nanoribbon, with proposed structure superimposed over the image. Reproduced from [132] with permission.

were undertaken for both zigzag and armchair terminated nanoribbons of different thicknesses. The optimized unit cells were compared to that of the bulk calculations to determine displacement from the bulk atom positions. This was necessary to determine the minimum thickness of ribbon necessary to have close to zero displacement in the centre, implying a central bulk region and outer edge regions. The displacements of each atom along the direction normal to the ribbon edge are shown in Fig. 7.3 alongside visualizations of these changes in structure, with bulk and edge regions defined.

Fig. 7.3 shows largest movement of atoms during optimization around the edges of each nanoribbon with relaxations due to the introduction of edges. The displacement of each atomic site decays to less than 0.05 Å at a distance of ∼6 Å from the edges, suggesting a minimum ribbon width with no edge-edge interaction of 12 $\mathring{A}$. This is far smaller than the width of the ten W atom thick ribbons modelled within this chapter (∼30 Å width), validating the model as a reasonable approximation to a single edged system. Small atom displacements

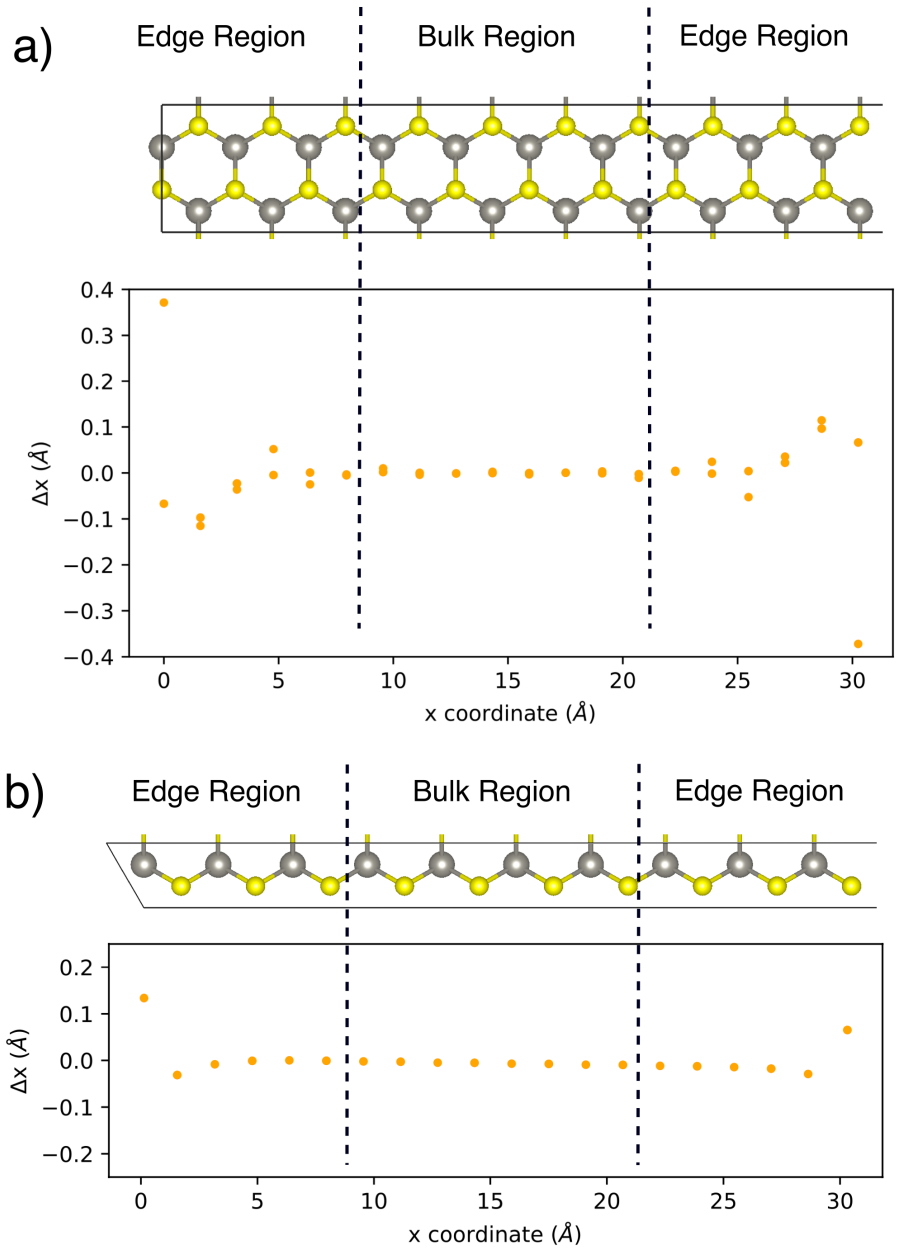

Figure 7.3: Displacements of atoms in the direction normal to the ribbon edge with respect to the bulk unit cell, aligned with corresponding atoms in a visualization of the unit cells. Displacements are shown for terminations along a) armchair and b) zigzag directions, with bulk and edge region boundaries highlighted.

in the bulk region implies any strain fields from the two edge regions do not overlap with each other, validating the model as a reasonable approximation of

single edge effects despite modelling a two edged system. Nanoribbons of ten W atoms thick were chosen for all edge calculations as this displayed sufficiently large bulk regions without being too computationally intensive. Kinked unit cells were constructed by terminating cells along different directions to sample a variety of different kink densities, namely along the (310),(410) and (510) Miller indices respectively for both the zigzag and armchair unit cells. As cartesian coordinates were used to calculate atom displacements, the identical displacements at each armchair edge present as mirrored in both the x and y axes. The opposite is true for the opposing changes in each edge along the zigzag edges, which have different relaxations at the edges. These relaxations are discussed further in the results section. The partial density of states for bulk regions were compared between systems to ensure consistency and further validate that the bulk regions did not contain edge states. The partial density of states for the edge regions were then compared to determine edge states within the band gap region from different edges and identify how this changed when kinks were introduced.

All DFT calculations were undertaken using a plane wave basis set, as implemented in VASP. A gamma centred Monkhorst-Pack grid with a k point grid density of 75 divided by the number of atoms in each unit cell, as generated by the pymatgen python package [133]. These k points were all along the length of the ribbon, with 1 k point used along other directions due to a lack of periodicity along these directions. All calculations were undertaken with the PBE functional, including Grimme's D3 corrections to a force tolerance of 0.01 eV/Å [48]. Density of states calculations were run on each optimized unit cell and evaluated on a grid of 2000 points to improve the resolution of peaks compared to the default grid. Version 5.2 PBE plane wave potentials (PAW) were used for all calculations, with plane wave cutoff value of 520 eV. Partial density of states for regions in different systems had varying numbers of atoms, thus density of states calculations were

all normalised by dividing by the number of atoms per unit cell to enable more effective comparison between systems. The numbers of atoms for each cell for the armchair terminations are 60, 240, 150, 90 and 60 for armchair, (510), (410), (310) and bulk cells respectively. The numbers of atoms for each cell for the zigzag terminations are 90, 146, 91, 71 and 90 for zigzag, (510), (410), (310) and bulk cells respectively.

7.3 Results

For clarity, directions of all edge terminations used in calculations are illustrated in Fig. 7.4.

The DOS for bulk regions within each cell were compared to that of the bulk unit cell. Fig. 7.5 shows the armchair and zigzag termination bulk region DOS compared to the bulk cell DOS. This shows all peaks in the density of states for each bulk region overlapping well with the bulk unit cell density of states, further validating the models as having well-defined bulk regions due to the lack of any edge states within the band gap produced by the bulk regions. Edge states originating from the bulk regions would indicate more extended edge regions. Small differences do exist between the DOS from the different terminations and the bulk unit cell. However this is likely due to slightly different k point spacing between cells. This was because the number of k points in each direction must be an integer and the cells were of different sizes, necessitating approximation of the number of k points to maintain a similar k point spacing.

The atoms that displaced the most in the armchair termination were W atoms along the edges, which moved towards the centre of the nanoribbon. Fig. 7.6b shows a smaller change during optimization of the zigzag termination - with outer W atoms moving towards the centre of the nanoribbon (blue) and outer S

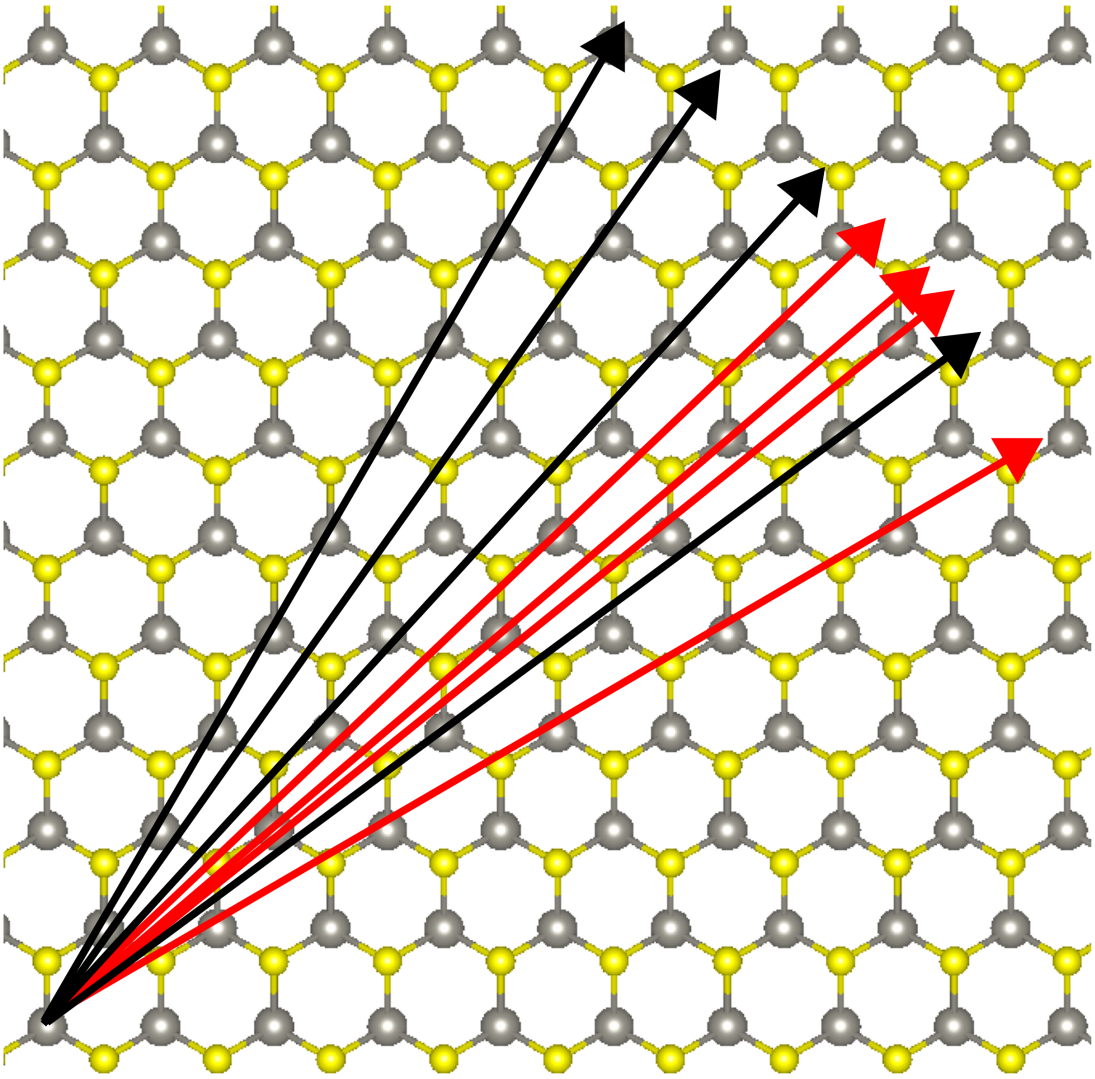

Figure 7.4: Edge termination directions overlaid on a bulk unit cell, showing (clockwise) armchair direction, (510) armchair,(410) armchair, (310) zigzag, (410) zigzag, (510) zigzag, (310) armchair, zigzag. Terminations generated from zigzag and armchair unit cells are shown in red and black respectively.

atoms moving away from the centre of the nanoribbon (red). These two different relaxations result from the asymmetry of the zigzag termination, resulting in two different edge types terminated with either W or S atoms.

Fig. 7.7 shows the partial DOS from the edge regions of all unit cells with mainly armchair edge character, compared to the DOS from the bulk unit cell. The armchair termination clearly adds many states into the band gap, reducing

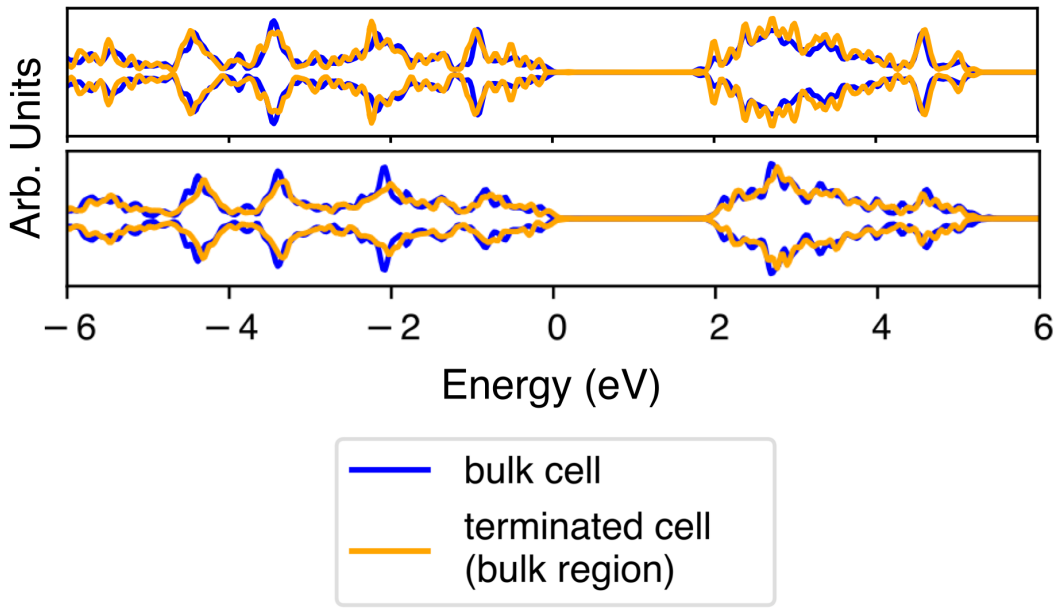

Figure 7.5: Bulk DOS compared to partial DOS from bulk regions of the armchair (top) and zigzag (bottom) terminated systems

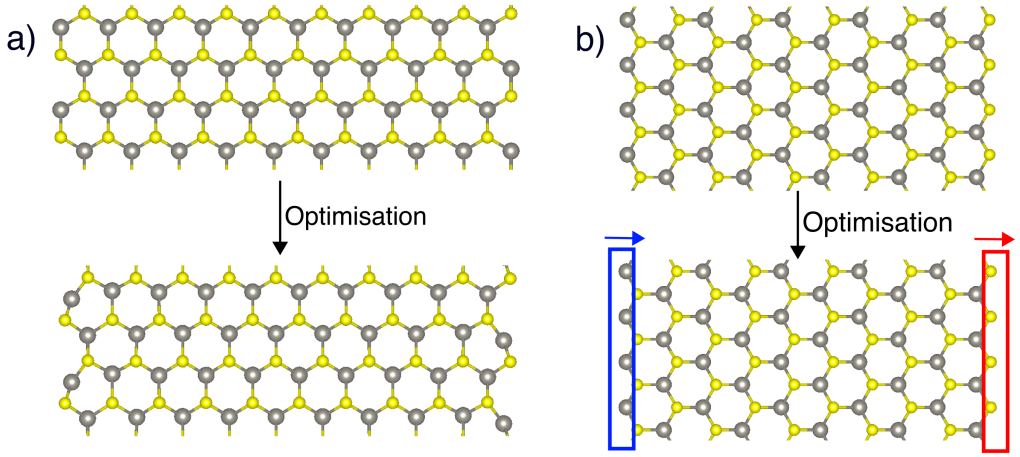

Figure 7.6: Visualizations of relaxations during optimization starting from bulk structures for a) armchair and b) zigzag terminations. Small variations in b) are highlighted by arrows showing directions of atom displacements for the left and right edges, shown in blue and red respectively.

the band gap to ∼0.3 eV, in line with literature [129]. The main effect of terminating along the (510) direction is to introduce some zigzag character to the edge, which introduces further states into the band gap to reduce this further to ∼0.2 eV. As the density of kink defects is increased the band gap is reduced to

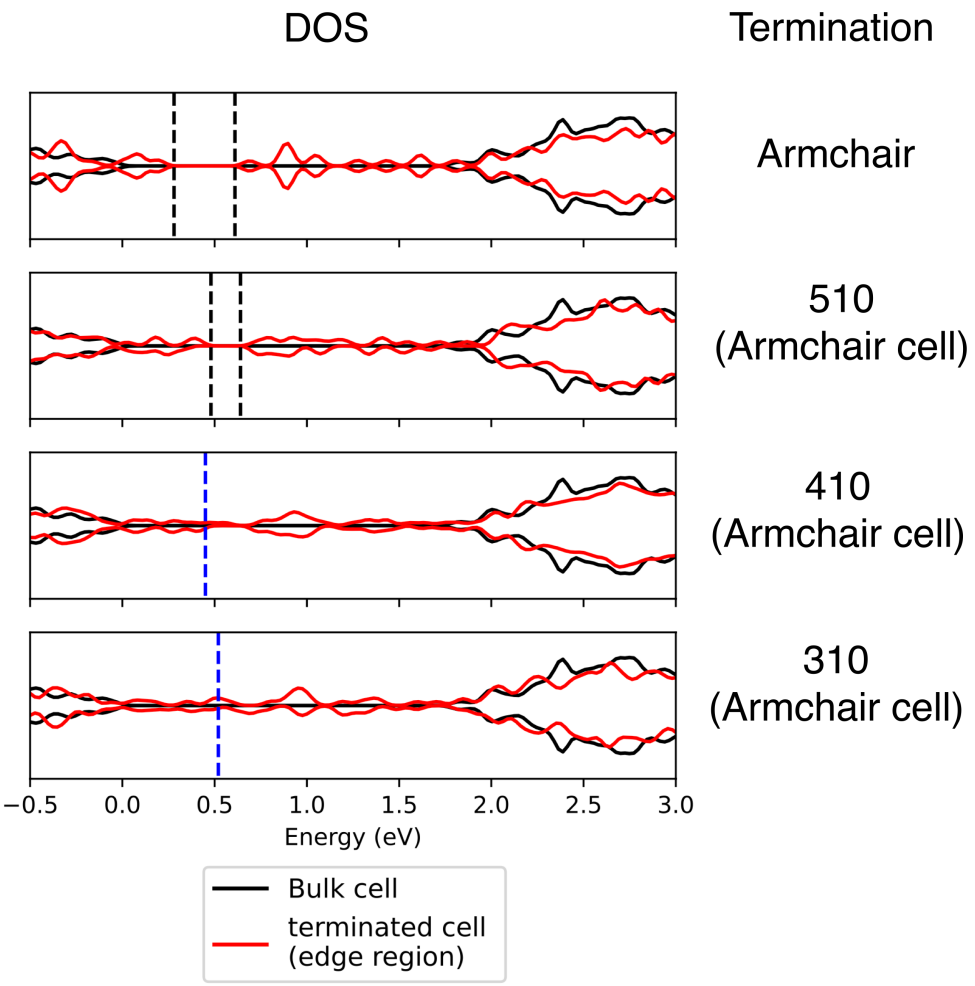

Figure 7.7: Partial density of states edge regions of each unit cell constructed from the armchair termination unit cell, compared to the bulk density of states. Armchair, (510), (410) and (310) terminations are shown from top to bottom. Band edges are shown by black dashed lines, and Fermi energies are shown by blue dashed lines for metallic systems.

zero as the system moves to a DOS closer to that of the metallic zigzag direction. The DOS was also calculated for a region around the kinks in each edge. This region is shown in Fig. 7.8, with W and S atoms chosen in a ratio of 1:2 to maintain the correct stoichiometric ratio. The DOS for each kink density is shown in Fig. 7.9. The reduction in band gap as kink density is increased is highlighted by this analysis, showing the density of states within the band gap region increasing - resulting in a metallic structure for the highest density of kinks. The different

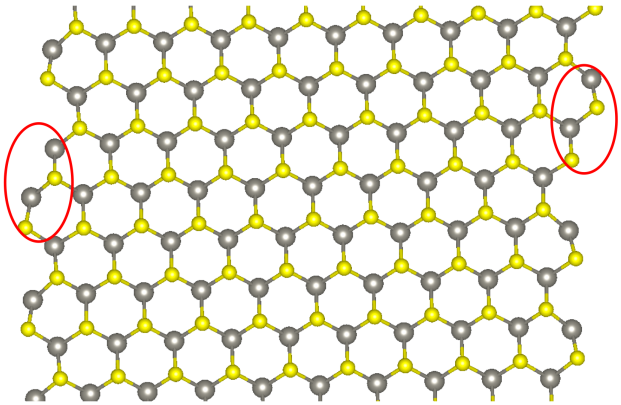

Figure 7.8: Kinked region atoms, illustrated for the 410 termination. 12 atoms total are chosen for each kink density: two W and 4 S atoms per edge.

states resulting from these atoms in different kink densities is likely due to strain fields from neighboring kinks interacting more with higher kink densities, resulting in a difference in structure, even within the armchair region, in comparison to the unkinked edge.

The corresponding results for edges with mainly zigzag character are shown in Fig. 7.10. There is no clear trend as the defect density is increased in this figure, as the zigzag edge produces a metallic electronic structure, so there is no band gap in any DOS to easily quantify the changes.

If the density of kinks could be controlled during the growth process, this provides a potential route to engineering the band gap. However this modification in band gap would be limited to the edge regions of any crystals. As the edges of a flake represent a larger fraction of the total flake area in nanoribbons, the effect would likely be more apparent in thinner samples. The effect could result in attraction of electrons from the bulk towards the edge region due to the lower energy transition compared to the bulk.

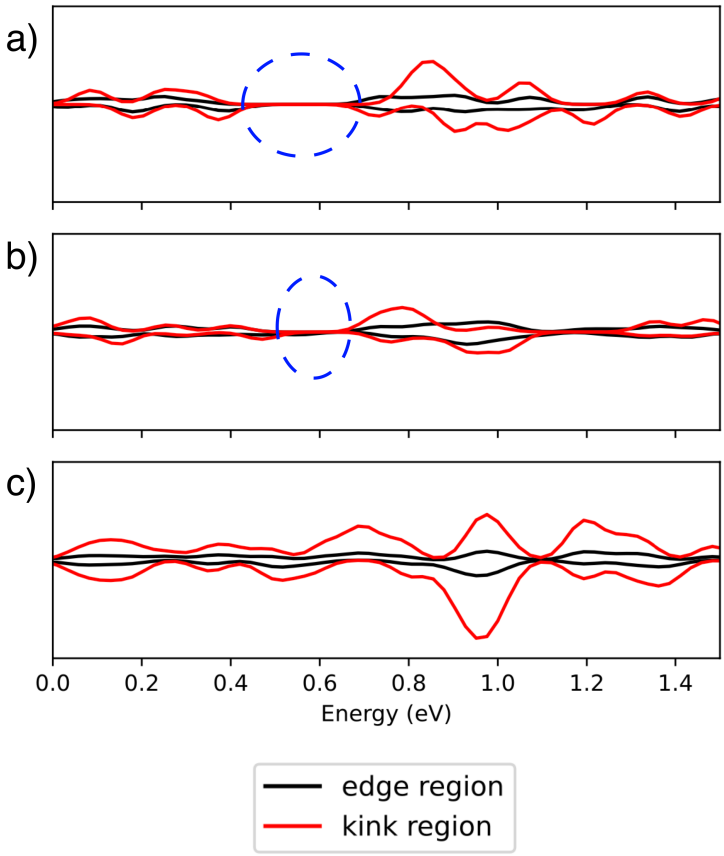

Figure 7.9: Density of states for armchair direction terminations with kinks, showing terminations along the a) (510), b) (410) and c) (310) directions. Reduced band gaps are highlighted in blue.

7.4 Discussion

As the band gap is reduced to below ∼0.3 eV when kink defects are introduced to the armchair termination, such defects are likely to act as non-radiative recombination centres - as the barrier to recombination across the band gap is reduced in these areas. This is expected to reduce the PL efficiency and could be probed by PL measurements of WS_2 nanoribbons to determine how PL intensity varies across nanoribbons with different kinks. However this is considered future work. The PBE functional was used for these calculations, which could lead to underestimation of the band gap. Such underestimation could be reduced by performing

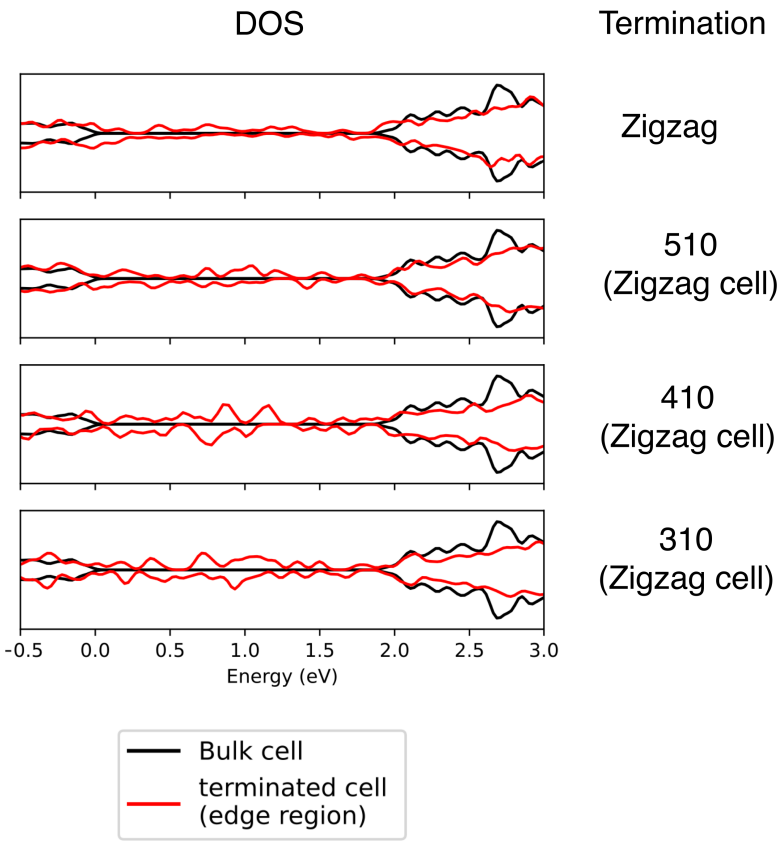

Figure 7.10: Partial density of states edge regions of each unit cell constructed from the zigzag termination unit cell, compared to the bulk density of states. Zigzag, (510), (410) and (310) terminations are shown from top to bottom.

calculations with a hybrid functional such as HSE06.

Further work would be necessary to consider further kink defect densities which would determine the limiting kink defect density along the armchair direction to maintain a band gap. This would allow further characterisation of the level of band gap variation as a function of this density. This work would be important in any application for band gap reduction, as it would determine the defect density necessary to reproduce a specific band gap. It would also determine the maximum defect density possible to still maintain a band gap.

7.5 Conclusion

Differing electronic structures between armchair and zigzag terminated WS_2 nanoribbons was confirmed, showing a reduced band gap of 0.3 eV for the armchair termination and a zero band gap metallic structure for zigzag terminated nanoribbons. Kink defects at different densities introduced along both armchair and zigzag edges separately were found to modify the density of states. However such defects introduced along an armchair termination were found to reduce the band gap with increasing defect density until a metallic structure is reached. This provides a potential route to engineering the band gap within 2D materials using edge defects. However further work would be necessary to determine the limiting defect density to maintain a band gap. This represents a novel contribution to the field as these calculations have not been undertaken for realistic edge defects containing both armchair and zigzag character - an important step towards development of realistic systems.

Chapter 8

Conclusions and Future work

8.1 Conclusions

In this thesis, defects and strain effects on electronic properties have been investigated in the 2D chalcogenide materials TiS_3, MoS_2 and WS_2, including both PL and DFT studies. Such studies are important to understand the fundamental effect of such defects and strain on optoelectronic properties, as both strain and defects are likely to be present in a realistic device. One example of this would be in flexible electronics where a successful device would need to deal with strain resulting from any flex of such a device. Defects are also present in any material, thus an understanding of their effect on optoelectronic properties is vital.

DFT studies investigating the orientation dependence of uniaxial strain in TiS_3 found this to be critical to the variation of band structure due to its anisotropic structure - strain was found to decrease linearly when oriented along the **a** lattice vector, but increased linearly when the strain direction was shifted by 90°. Comparing this to MoS_2, which was found to have a roughly constant band gap variation with strain independent of strain direction due to its highly isotropic structure, suggests the use of this technique within more anisotropic

materials could introduce another degree of freedom with which to tailor this strain response.

Extending the investigation of strain to monolayer WS_2, PL was used to characterise the band structure response to strain applied experimentally by pillars fabricated on a silicon substrate by varying the height of such pillars from 250 μm to 500 μm. The higher pillars were found to increase the strain supported by the suspended WS_2. However the standard error was smaller for 250 μm pillars, suggesting higher reliability for smaller pillars at the expense of a lower strain being introduced. Wet and dry transfer techniques were compared for transferring WS_2 flakes to the nanostructures with dry transfer found to introduce a $\sim$9 nm shift in the peak of the PL curve compared to a $\sim$2 nm shift for wet transfer. This suggests dry transfer is the optimum choice for introduction of higher strains using this method.

The impact of point defects on charge trapping was studied using DFT in four layer MoS_2, namely substitution and surface adsorption of different oxygen species. O, O_2 and O_3 were considered, with O adsorption found to be the most energetically favourable under most conditions. None of the defects considered were found to introduce charge trapping effects. Chlorine substitution with sulfur was also investigated as a comparison. This was found to cause n-type doping by creating states within the band gap near the bottom of the conduction band to donate an electron to the system, shown by density of states calculations.

Defects were considered within monolayer WS_2, focusing specifically on edge defects. Large differences in electronic structure were found between structures terminated along the armchair and zigzag directions. Armchair terminations resulted in a reduction in band gap, compared to zigzag terminations which introduced a metallic structure with no band gap. Terminations between the armchair and zigzag directions introduced a mixture of these outcomes, with

directions close to the armchair termination causing a further reduction in band gap, potentially suggesting a novel method for localised band gap engineering.

In conclusion, a selection of methods for modification of optoelectronic properties have been shown to be possible within 2D chalcogenide materials due to their reduced dimensionality, with such methods providing different changes in electronic structure. Each of the methods investigated has highlighted further research possibilities and directions.

8.2 Future work

While the work presented in this thesis provides insight into some methods of electronic structure modulation, it is by no means exhaustive, with various other routes possible to achieve this objective - some examples being twistronics and heterostructures [74, 134]. Opportunity to further extend the research purely involving methods considered within this thesis also exist.

A general avenue applying to all chapters would be to consider a broader range of materials; the field of 2D materials provides a large sample space to explore, with only a limited selection of structures and atoms explored within this work - even within the 2D chalcogenide family.

In terms of the strain calculations presented in chapter 4, further extension could include biaxial strain of such systems as well as directional strain experiments to determine the limit of mechanical strains applied along different directions before breaking of the materials.

Other ways of straining materials exist other than the pillarred substrate method utilised in chapter 5, including bending substrates allowing variable strain with time which could be explored. Only two pillar heights have been explored within this work, thus an improvement could involve examining the effects of

intermediate pillar heights as well as different substrates to further optimize the method. The effect of pillar shape could also be considered, for example triangular or square pillars could be introduced. The potential for this technique to enable single photon emission is also considered future work, as this would involve PL measurements under cryogenic temperatures.

Further point defects in MoS_2 could also have been included within chapter 6. While chlorine and oxygen dopants have been studied for example, many other dopant candidates could be included. A limited selection of chlorine and oxygen defects have also been included, leaving further possibilities to explore such defects within different numbers of layers or defects sandwiched between these layers.

One of the main opportunities to further build upon the work presented in chapter 7 is to include hybrid functional calculations. This was deemed prohibitively computationally expensive within this thesis but could provide more concrete conclusions on the band gap size for different edges due to the limited accuracy of unnocupied state energies at the PBE level of theory. Further edges could also be considered to further examine the level of band gap variation possible from different terminations.

Bibliography

[1] Unni Krishnan, Manjot Kaur, Kulwinder Singh, Manjeet Kumar, and Akshay Kumar. A synoptic review of MoS_2: Synthesis to applications. *Superlattices and Microstructures*, 128:274–297, 4 2019.

[2] Omnia Samy, Shuwen Zeng, Muhammad Danang Birowosuto, and Amine El Moutaouakil. A Review on MoS_2 Properties, Synthesis, Sensing Applications and Challenges. *Crystals 2021, Vol. 11, Page 355*, 11(4):355, 3 2021.

[3] Xiao Li and Hongwei Zhu. Two-dimensional MoS_2: Properties, preparation, and applications. *Journal of Materiomics*, 1(1):33–44, 3 2015.

[4] Rudren Ganatra and Qing Zhang. Few-layer MoS_2: A promising layered semiconductor. *ACS Nano*, 8(5):4074–4099, 5 2014.

[5] Dominik Lembke, Simone Bertolazzi, and Andras Kis. Single-layer MoS_2 electronics. *Accounts of Chemical Research*, 48(1):100–110, 1 2015.

[6] Dan Wang, Xian Bin Li, Dong Han, Wei Quan Tian, and Hong Bo Sun. Engineering two-dimensional electronics by semiconductor defects. *Nano Today*, 16:30–45, 10 2017.

[7] Shengxue Yang, Yujia Chen, and Chengbao Jiang. Strain engineering of two-dimensional materials: Methods, properties, and applications. *InfoMat*, 3(4):397–420, 4 2021.

[8] K. S. Novoselov, A. K. Geim, S. V. Morozov, D. Jiang, Y. Zhang, S. V. Dubonos, I. V. Grigorieva, and A. A. Firsov. Electric field in atomically thin carbon films. *Science*, 306(5696):666–669, 10 2004.

[9] Enlai Gao, Shao Zhen Lin, Zhao Qin, Markus J. Buehler, Xi Qiao Feng, and Zhiping Xu. Mechanical exfoliation of two-dimensional materials. *Journal of the Mechanics and Physics of Solids*, 115:248–262, 6 2018.

[10] John Radly M. Sevilla and Darwin B. Putungan. Graphene-hexagonal boron nitride van der Waals heterostructures: an examination of the effects of different van der Waals corrections. *Materials Research Express*, 8(8):085601, 8 2021.

[11] Phuong V. Pham, Srikrishna Chanakya Bodepudi, Khurram Shehzad, Yuan Liu, Yang Xu, Bin Yu, and Xiangfeng Duan. 2D Heterostructures for Ubiquitous Electronics and Optoelectronics: Principles, Opportunities, and Challenges. *Chemical Reviews*, 122(6):6514–6613, 3 2022.

[12] Ankur Gupta, Tamilselvan Sakthivel, and Sudipta Seal. Recent development in 2D materials beyond graphene. *Progress in Materials Science*, 73:44–126, 8 2015.

[13] Fahrettin Sarcan, Alex J. Armstrong, Yusuf K. Bostan, Esra Kus, Keith P. McKenna, Ayse Erol, and Yue Wang. Ultraviolet-Ozone Treatment: An Effective Method for Fine-Tuning Optical and Electrical Properties of Suspended and Substrate-Supported MoS_2. *Nanomaterials 2023, Vol. 13, Page 3034*, 13(23):3034, 11 2023.

[14] Nishant Tripathi, Vladimir Pavelyev, Prachi Sharma, Sunil Kumar, Anastasiia Rymzhina, and Prabhash Mishra. Review of titanium trisulfide (TiS_3): A novel material for next generation electronic and optical devices. *Materials Science in Semiconductor Processing*, 127:105699, 6 2021.

[15] Juhong Park, Min Su Kim, Eunho Cha, Jeongyong Kim, and Wonbong Choi. Synthesis of uniform single layer WS_2 for tunable photoluminescence. *Scientific Reports 2017 7:1*, 7(1):1–8, 11 2017.

[16] Taposhree Dutta, Neha Yadav, Yongling Wu, Gary J. Cheng, Xiu Liang, Seeram Ramakrishna, Aoussaj Sbai, Rajeev Gupta, Aniruddha Mondal, Zheng Hongyu, and Ashish Yadav. Electronic properties of 2D materials and their junctions. *Nano Materials Science*, 6 2023.

[17] Claudia Ruppert, Ozgur Burak Aslan, and Tony F. Heinz. Optical properties and band gap of single- and few-layer $MoTe_2$ crystals. *Nano Letters*, 14(11):6231–6236, 11 2014.

[18] J. C. Phillips. Band Structure of Silicon, Germanium, and Related Semiconductors. *Physical Review*, 125(6):1931, 3 1962.

[19] Zhiping Zhou, Bing Yin, and Jurgen Michel. On-chip light sources for silicon photonics. *Light: Science and Applications*, 4(11):358, 11 2015.

[20] Alireza Moridi, Haihui Ruan, L. C. Zhang, and Mei Liu. Residual stresses in thin film systems: Effects of lattice mismatch, thermal mismatch and interface dislocations. *International Journal of Solids and Structures*, 50(22-23):3562–3569, 10 2013.

[21] Robert Hull and John C. Bean. Misfit dislocations in lattice-mismatched epitaxial films. *Critical Reviews in Solid State and Material Sciences*, 17(6):507–546, 1 1992.

[22] Hao-Wei Guo, Zhen Hu, Zhi-Bo Liu, Jian-Guo Tian, H.-W Guo, Z Hu, Z.-B Liu, and J.-G Tian. Stacking of 2D Materials. *Advanced Functional Materials*, 31(4):2007810, 1 2021.

[23] D. Stradi, S. Barja, C. Díaz, M. Garnica, B. Borca, J. J. Hinarejos, D. Sánchez-Portal, M. Alcamí, A. Arnau, A. L. Vázquez De Parga, R. Miranda, and F. Martín. Lattice-matched versus lattice-mismatched models to describe epitaxial monolayer graphene on Ru(0001). *Physical Review B - Condensed Matter and Materials Physics*, 88(24):245401, 12 2013.

[24] Zhiwei Peng, Xiaolin Chen, Yulong Fan, David J. Srolovitz, and Dangyuan Lei. Strain engineering of 2D semiconductors and graphene: from strain fields to band-structure tuning and photonic applications. *Light: Science & Applications 2020 9:1*, 9(1):1–25, 11 2020.

[25] Yalan Yan, Shuang Ding, Xiaonan Wu, Jian Zhu, Dengman Feng, Xiaodong Yang, and Fangfei Li. Tuning the physical properties of ultrathin transition-metal dichalcogenides via strain engineering. *RSC Advances*, 10(65):39455–39467, 10 2020.

[26] Jin Li, Gui Gui, and Jianxin Zhong. Tunable bandgap structures of two-dimensional boron nitride. *Journal of Applied Physics*, 104(9):94311, 11 2008.

[27] Kai Zhong, Rupeng Bu, Fangbao Jiao, Guangrui Liu, and Chaoyang Zhang. Toward the defect engineering of energetic materials: A review of the effect of crystal defects on the sensitivity. *Chemical Engineering Journal*, 429:132310, 2 2022.

[28] Alexander Eeles. *Performance characterisation of photovoltaic devices: managing the effects of high capacitance and metastability.* PhD thesis, Loughborough University, 2016.

[29] Edmund G. Seebauer and Meredith C. Kratzer. Charged point defects in semiconductors. *Materials Science and Engineering: R: Reports*, 55(3-6):57–149, 12 2006.

[30] John A. Carr and Sumit Chaudhary. The identification, characterization and mitigation of defect states in organic photovoltaic devices: a review and outlook. *Energy & Environmental Science*, 6(12):3414–3438, 11 2013.

[31] Kehao Zhang and Joshua Robinson. Doping of two-dimensional semiconductors: A rapid review and outlook. *MRS Advances*, 4(51-52):2743–2757, 9 2019.

[32] Muge Acik and Yves J. Chabal. Nature of graphene edges: A review. *Japanese Journal of Applied Physics*, 50(7 PART 1):070101, 7 2011.

[33] Abhik Ghosh. Just how good is DFT? *Journal of Biological Inorganic Chemistry*, 11(6):671–673, 9 2006.

[34] Axel D. Becke. Perspective: Fifty years of density-functional theory in chemical physics. *Journal of Chemical Physics*, 140(18):18–301, 5 2014.

[35] Max Born. Born-oppenheimer approximation. *Ann. Phys*, 84:457–484, 1927.

[36] P. Lykos and G. W. Pratt. Discussion on The Hartree-Fock Approximation. *Reviews of Modern Physics*, 35(3):496, 7 1963.

[37] K Hirao. Recent Advances in Multireference Methods. 4, 2 1999.

[38] S. M. Blinder. Basic Concepts of Self-Consistent-Field Theory. *American Journal of Physics*, 33(6):431–443, 6 1965.

[39] P. Hohenberg and W. Kohn. Inhomogeneous Electron Gas. *Physical Review*, 136(3B):B864–B871, 11 1964.

[40] W. Kohn and L. J. Sham. Self-consistent equations including exchange and correlation effects. *Physical Review*, 140(4A):A1133, 11 1965.

[41] Julien Toulouse. Review of Approximations for the Exchange-Correlation Energy in Density-Functional Theory. *Density Functional Theory*, pages 1–90, 2023.

[42] John P. Perdew, Kieron Burke, and Matthias Ernzerhof. Generalized Gradient Approximation Made Simple. *Physical Review Letters*, 77(18):3865, 10 1996.

[43] Carlo Adamo and Vincenzo Barone. Toward reliable density functional methods without adjustable parameters: The PBE0 model. *The Journal of Chemical Physics*, 110(13):6158–6170, 4 1999.

[44] Jochen Heyd, Juan E. Peralta, Gustavo E. Scuseria, and Richard L. Martin. Energy band gaps and lattice parameters evaluated with the Heyd-Scuseria-Ernzerhof screened hybrid functional. *Journal of Chemical Physics*, 123(17):174101, 11 2005.

[45] Michael E. Foster and Karl Sohlberg. Empirically corrected DFT and semi-empirical methods for non-bonding interactions. *Physical Chemistry Chemical Physics*, 12(2):307–322, 12 2009.

[46] K. Berland, D. Chakraborty, and T. Thonhauser. Van der Waals density functional with corrected C6 coefficients. *Physical Review B*, 99(19):195418, 5 2019.

[47] Kristian Berland, Valentino R. Cooper, Kyuho Lee, Elsebeth Schröder, T. Thonhauser, Per Hyldgaard, and Bengt I. Lundqvist. van der Waals forces in density functional theory: a review of the vdW-DF method. *Reports on Progress in Physics*, 78(6):066501, 5 2015.

[48] Stefan Grimme, Jens Antony, Stephan Ehrlich, and Helge Krieg. A consistent and accurate ab initio parametrization of density functional dispersion correction (DFT-D) for the 94 elements H-Pu. *Journal of Chemical Physics*, 132(15):24103, 4 2010.

[49] G. Makov and M. C. Payne. Periodic boundary conditions in ab initio calculations. *Physical Review B*, 51(7):4014, 2 1995.

[50] Mario Pitteri and Giovanni Zanzotto. On the Definition and Classification of Bravais Lattices. *urn:issn:0108-7673*, 52(6):830–838, 11 1996.

[51] Yen-Lin Tsai, Jone F Chen, Shang-Feng Shen, and al . Non-radiative transitions in semiconductors. *Reports on Progress in Physics*, 44(12):1251, 12 1981.

[52] Yang Chun Lee, Sih Wei Chang, Shu Hsien Chen, Shau Liang Chen, and Hsuen Li Chen. Optical Inspection of 2D Materials: From Mechanical Exfoliation to Wafer-Scale Growth and Beyond. *Advanced Science*, 9(1), 1 2022.

[53] Itai Epstein, Bernat Terrés, André J. Chaves, Varun Varma Pusapati, Daniel A. Rhodes, Bettina Frank, Valentin Zimmermann, Ying Qin, Kenji

Watanabe, Takashi Taniguchi, Harald Giessen, Sefaattin Tongay, James C. Hone, Nuno M.R. Peres, and Frank H.L. Koppens. Near-unity light absorption in a monolayer WS_2 van der waals heterostructure cavity. *Nano Letters*, 20(5):3545–3552, 5 2020.

[54] G. G. Macfarlane, T. P. McLean, J. E. Quarrington, and V. Roberts. Exciton and phonon effects in the absorption spectra of germanium and silicon. *Journal of Physics and Chemistry of Solids*, 8(C):388–392, 1 1959.

[55] Matěj Velický and Peter S. Toth. From two-dimensional materials to their heterostructures: An electrochemist's perspective. *Applied Materials Today*, 8:68–103, 9 2017.

[56] Soohyung Park, Niklas Mutz, Thorsten Schultz, Sylke Blumstengel, Ali Han, Areej Aljarb, Lain Jong Li, Emil J.W. List-Kratochvil, Patrick Amsalem, and Norbert Koch. Direct determination of monolayer MoS_2 and WSe_2 exciton binding energies on insulating and metallic substrates. *2D Materials*, 5(2):025003, 1 2018.

[57] Yuchun Liu, Tianci Shen, Shuangyi Linghu, Ruilin Zhu, and Fuxing Gu. Electrostatic control of photoluminescence from A and B excitons in monolayer molybdenum disulfide. *Nanoscale Advances*, 4(11):2484–2493, 5 2022.

[58] Jun Xiao, Mervin Zhao, Yuan Wang, and Xiang Zhang. Excitons in atomically thin 2D semiconductors and their applications. *Nanophotonics*, 6(6):1309–1328, 11 2017.

[59] Maja Feierabend, Samuel Brem, and Ermin Malic. Optical fingerprint of bright and dark localized excitonic states in atomically thin 2D materials. *Physical Chemistry Chemical Physics*, 21(47):26077–26083, 12 2019.

[60] Andrea Splendiani, Liang Sun, Yuanbo Zhang, Tianshu Li, Jonghwan Kim, Chi Yung Chim, Giulia Galli, and Feng Wang. Emerging photoluminescence in monolayer MoS_2. *Nano Letters*, 10(4):1271–1275, 4 2010.

[61] Jae Ung Lee, Kangwon Kim, and Hyeonsik Cheong. Resonant Raman and photoluminescence spectra of suspended molybdenum disulfide. *2D Materials*, 2(4):044003, 10 2015.

[62] Yifei Yu, Yiling Yu, Chao Xu, Yong-Qing Cai, Liqin Su, Yong Zhang, Yong-Wei Zhang, Kenan Gundogdu, Linyou Cao, Y Yu, L Cao, C Xu, K Gundogdu, Y-q Cai, Y-w Zhang, L Su, and Y Zhang. Engineering Substrate Interactions for High Luminescence Efficiency of Transition-Metal Dichalcogenide Monolayers. *Advanced Functional Materials*, 26(26):4733–4739, 7 2016.

[63] R. P. Feynman. Forces in Molecules. *Physical Review*, 56(4):340, 8 1939.

[64] J. L. Nazareth. Conjugate gradient method. *Wiley Interdisciplinary Reviews: Computational Statistics*, 1(3):348–353, 11 2009.

[65] Jr. J. E. Dennis and Jorge J. Moré. Quasi-Newton Methods, Motivation and Theory. *https://doi.org/10.1137/1019005*, 19(1):46–89, 7 2006.

[66] Xiangming Xu, Tianchao Guo, Hyunho Kim, Mrinal K Hota, Rajeh S Alsaadi, Mario Lanza, Xixiang Zhang, Husam N Alshareef, X Xu, T Guo, H Kim, M K Hota, R S Alsaadi, M Lanza, X Zhang, H N Alshareef Materials Science, and Engineering Physical Science. Growth of 2D Materials at the Wafer Scale. *Advanced Materials*, 34(14):2108258, 4 2022.

[67] Alex Armstrong, Keith P. McKenna, and Yue Wang. Directional dependence of band gap modulation via uniaxial strain in MoS_2 and TiS_3. *Nanotechnology*, 35(1):015704, 10 2023.

[68] Cheng Yue Wang, Shao Rong Li, Su Fang Wang, Peng Xiang Zhao, and Ri Sheng Zhuo. First principles study of the effect of uniaxial strain on monolayer MoS_2. *Physica E: Low-dimensional Systems and Nanostructures*, 144:115401, 10 2022.

[69] Xiaofeng Fan, C. H. Chang, W. T. Zheng, Jer Lai Kuo, and David J. Singh. The electronic properties of single-layer and multilayer MoS_2 under high pressure. *Journal of Physical Chemistry C*, 119(19):10189–10196, 5 2015.

[70] Jun Kang and Lin Wang Wang. Robust band gap of TiS_3 nanofilms. *Physical Chemistry Chemical Physics*, 18(22):14805–14809, 6 2016.

[71] Keliang He, Charles Poole, Kin Fai Mak, and Jie Shan. Experimental demonstration of continuous electronic structure tuning via strain in atomically thin MoS_2. *Nano Letters*, 13(6):2931–2936, 6 2013.

[72] Robert Biele, Eduardo Flores, Jose Ramón Ares, Carlos Sanchez, Isabel J. Ferrer, Gabino Rubio-Bollinger, Andres Castellanos-Gomez, and Roberto D'Agosta. Strain-induced band gap engineering in layered TiS_3. *Nano Research 2018 11:1*, 11(1):225–232, 8 2017.

[73] Yaping Qi, Mohammad A. Sadi, Dan Hu, Ming Zheng, Zhenping Wu, Yucheng Jiang, and Yong P. Chen. Recent Progress in Strain Engineering on Van der Waals 2D Materials: Tunable Electrical, Electrochemical, Magnetic, and Optical Properties. *Advanced Materials*, 35(12):2205714, 3 2023.

[74] Stephen Carr, Daniel Massatt, Shiang Fang, Paul Cazeaux, Mitchell Luskin, and Efthimios Kaxiras. Twistronics: Manipulating the electronic

properties of two-dimensional layered structures through their twist angle. *Physical Review B*, 95(7):075420, 2 2017.

[75] Koichi Momma and Fujio Izumi. VESTA 3 for three-dimensional visualization of crystal, volumetric and morphology data. *Journal of Applied Crystallography*, 44(6):1272–1276, 12 2011.

[76] Z. Y. Zhu, Y. C. Cheng, and U. Schwingenschlögl. Giant spin-orbit-induced spin splitting in two-dimensional transition-metal dichalcogenide semiconductors. *Physical Review B - Condensed Matter and Materials Physics*, 84(15):153402, 10 2011.

[77] Kazuhiro Endo, Hideo Ihara, Kazuhiro Watanabe, and Shun Ichi Gonda. XPS study of one-dimensional compounds: TiS_3. *Journal of Solid State Chemistry*, 44(2):268–272, 9 1982.

[78] Ferdows Zahid, Lei Liu, Yu Zhu, Jian Wang, and Hong Guo. A generic tight-binding model for monolayer, bilayer and bulk MoS_2. *AIP Advances*, 3(5):052111, 5 2013.

[79] Kin Fai Mak, Changgu Lee, James Hone, Jie Shan, and Tony F. Heinz. Atomically thin MoS_2: A new direct-gap semiconductor. *Physical Review Letters*, 105(13):136805, 9 2010.

[80] Anastasia V. Tyurnina, Denis A. Bandurin, Ekaterina Khestanova, Vasyl G. Kravets, Maciej Koperski, Francisco Guinea, Alexander N. Grigorenko, Andre K. Geim, and Irina V. Grigorieva. Strained Bubbles in van der Waals Heterostructures as Local Emitters of Photoluminescence with Adjustable Wavelength. *ACS Photonics*, 6(2):516–524, 2 2019.

[81] Sajedeh Manzeli, Adrien Allain, Amirhossein Ghadimi, and Andras Kis. Piezoresistivity and Strain-induced Band Gap Tuning in Atomically Thin MoS_2. *Nano Letters*, 15(8):5330–5335, 8 2015.

[82] Mounika Vutukuru, Hossein Ardekani, Zhuofa Chen, Ryan L. Wilmington, Kenan Gundogdu, and Anna K. Swan. Enhanced Dielectric Screening and Photoluminescence from Nanopillar-Strained MoS_2 Nanosheets: Implications for Strain Funneling in Optoelectronic Applications. *ACS Applied Nano Materials*, 4(8):8101–8107, 8 2021.

[83] Sohail Ahmad and Sugata Mukherjee. A Comparative Study of Electronic Properties of Bulk MoS2 and Its Monolayer Using DFT Technique: Application of Mechanical Strain on MoS_2 Monolayer. *Graphene*, 03(04):52–59, 10 2014.

[84] Peng Lu, Xiaojun Wu, Wanlin Guo, and Xiao Cheng Zeng. Strain-dependent electronic and magnetic properties of MoS_2 monolayer, bilayer, nanoribbons and nanotubes. *Physical Chemistry Chemical Physics*, 14(37):13035–13040, 8 2012.

[85] Qu Yue, Jun Kang, Zhengzheng Shao, Xueao Zhang, Shengli Chang, Guang Wang, Shiqiao Qin, and Jingbo Li. Mechanical and electronic properties of monolayer MoS_2 under elastic strain. *Physics Letters A*, 376(12-13):1166–1170, 2 2012.

[86] Shuo Deng, Lijie Li, and Min Li. Stability of direct band gap under mechanical strains for monolayer MoS_2, $MoSe_2$, WS_2 and WSe_2. *Physica E: Low-dimensional Systems and Nanostructures*, 101:44–49, 7 2018.

[87] Dongting Jiang, Zhiyuan Liu, Zhe Xiao, Zhengfang Qian, Yiling Sun, Zhiyuan Zeng, and Renheng Wang. Flexible electronics based on 2D tran-

sition metal dichalcogenides. *Journal of Materials Chemistry A*, 10(1):89–121, 12 2021.

[88] G. Kresse and J. Furthmüller. Efficient iterative schemes for ab initio total-energy calculations using a plane-wave basis set. *Physical Review B - Condensed Matter and Materials Physics*, 54(16):11169–11186, 10 1996.

[89] Alex M Ganose, Adam J Jackson, and David O Scanlon. sumo: Command-line tools for plotting and analysis of periodic ab initio calculations. *Journal of Open Source Software*, 3(28):717, 8 2018.

[90] R. A. Bromley, R. B. Murray, and A. D. Yoffe. The band structures of some transition metal dichalcogenides. III. Group VIA: trigonal prism materials. *Journal of Physics C: Solid State Physics*, 5(7):759, 4 1972.

[91] R. Coehoorn, C. Haas, J. Dijkstra, C. J.F. Flipse, R. A. De Groot, and A. Wold. Electronic structure of ¡span class. *Physical Review B*, 35(12):6195, 4 1987.

[92] A. Kuc, N. Zibouche, and T. Heine. Influence of quantum confinement on the electronic structure of the transition metal sulfide TS_2. *Physical Review B - Condensed Matter and Materials Physics*, 83(24):245213, 6 2011.

[93] Ashwin Ramasubramaniam. Large excitonic effects in monolayers of molybdenum and tungsten dichalcogenides. *Physical Review B - Condensed Matter and Materials Physics*, 86(11):115409, 9 2012.

[94] Juan E. Peralta, Jochen Heyd, Gustavo E. Scuseria, and Richard L. Martin. Spin-orbit splittings and energy band gaps calculated with the Heyd-Scuseria-Ernzerhof screened hybrid functional. *Physical Review B - Condensed Matter and Materials Physics*, 74(7):073101, 8 2006.

[95] Hannu Pekka Komsa and Arkady V. Krasheninnikov. Native defects in bulk and monolayer MoS_2 from first principles. *Physical Review B - Condensed Matter and Materials Physics*, 91(12):125304, 3 2015.

[96] John P. Perdew and Mel Levy. Physical content of the exact kohn-sham orbital energies: Band gaps and derivative discontinuities. *Physical Review Letters*, 51(20):1884–1887, 11 1983.

[97] Ashok Kumar, Jagdish Kumar, and P. K. Ahluwalia. Electronic structure and optical conductivity of two dimensional (2D) MoS_2: Pseudopotential DFT versus full potential calculations. In *AIP Conference Proceedings*, volume 1447, pages 1269–1270. American Institute of Physics AIP, 6 2012.

[98] Chih Chiang Shen, Yu Te Hsu, Lain Jong Li, and Hsiang Lin Liu. Charge dynamics and electronic structures of monolayer MoS_2 films grown by chemical vapor deposition. *Applied Physics Express*, 6(12):125801, 12 2013.

[99] Nourdine Zibouche, Martin Schlipf, and Feliciano Giustino. GW band structure of monolayer MoS_2 using the Sternheimer GW method and effect of dielectric environment. *Physical Review B*, 103(12):125401, 3 2021.

[100] V. Petkov, S. J. L. Billinge, P. Larson, S. D. Mahanti, T. Vogt, K. K. Rangan, and M. G. Kanatzidis. Structure of nanocrystalline materials using atomic pair distribution function analysis: Study of $limos_2$. *Phys. Rev. B*, 65:092105, 2 2002.

[101] Chih Pin Lu, Guohong Li, Jinhai Mao, Li Min Wang, and Eva Y. Andrei. Bandgap, mid-gap states, and gating effects in MoS_2. *Nano Letters*, 14(8):4628–4633, 8 2014.

[102] Luqing Wang, Alex Kutana, and Boris I. Yakobson. Many-body and spin-orbit effects on direct-indirect band gap transition of strained monolayer MoS_2 and WS_2. *Annalen der Physik*, 526(9-10):L7–L12, 10 2014.

[103] Jun Kang, Hasan Sahin, and François M. Peeters. Mechanical properties of monolayer sulphides: A comparative study between MoS_2, HfS_2 and TiS_3. *Physical Chemistry Chemical Physics*, 17(41):27742–27749, 10 2015.

[104] Bingchen Deng, Riccardo Frisenda, Cheng Li, Xiaolong Chen, Andres Castellanos-Gomez, and Fengnian Xia. Progress on Black Phosphorus Photonics. *Advanced Optical Materials*, 6(19):1800365, 10 2018.

[105] M. Gerosa, C. E. Bottani, C. Di Valentin, G. Onida, and G. Pacchioni. Accuracy of dielectric-dependent hybrid functionals in the prediction of optoelectronic properties of metal oxide semiconductors: A comprehensive comparison with many-body GW and experiments. *Journal of Physics Condensed Matter*, 30(4):44003, 1 2018.

[106] Andreas Pospischil and Thomas Mueller. Optoelectronic Devices Based on Atomically Thin Transition Metal Dichalcogenides. *Applied Sciences 2016, Vol. 6, Page 78*, 6(3):78, 3 2016.

[107] Jorge Quereda, Sruthi Kuriakose, Carmen Munuera, Federico J. Mompean, Abdullah M. Al-Enizi, Ayman Nafady, Enrique Diez, Riccardo Frisenda, and Andres Castellanos-Gomez. Scalable and low-cost fabrication of flexible WS_2 photodetectors on polycarbonate. *npj Flexible Electronics 2022 6:1*, 6(1):1–9, 4 2022.

[108] Daniele Braga, Ignacio Gutiérrez Lezama, Helmuth Berger, and Alberto F. Morpurgo. Quantitative determination of the band gap of WS_2 with am-

bipolar ionic liquid-gated transistors. *Nano Letters*, 12(10):5218–5223, 10 2012.

[109] Qi Fu, Lei Yang, Wenhui Wang, Ali Han, Jian Huang, Pingwu Du, Zhiyong Fan, Jingyu Zhang, Bin Xiang, Q Fu, L Yang, W Wang, A Han, J Huang, P Du, B Xiang, and Z Fan. Synthesis and Enhanced Electrochemical Catalytic Performance of Monolayer $WS_2(1–x)Se_2x$ with a Tunable Band Gap. *Advanced Materials*, 27(32):4732–4738, 8 2015.

[110] Yanlong Wang Ting Yu Chunxiao Cong, Jingzhi Shang. Optical Properties of 2D Semiconductor WS_2. *Advanced Optical Materials*, 6(1):1700767, 1 2018.

[111] Ali Eftekhari. Tungsten dichalcogenides (WS 2 , WSe 2 , and WTe 2): materials chemistry and applications. *Journal of Materials Chemistry A*, 5(35):18299–18325, 9 2017.

[112] Wenshen Song and Li Yang. Quasiparticle band gaps and optical spectra of strained monolayer transition-metal dichalcogenides. *Physical Review B*, 96(23):235441, 12 2017.

[113] Mark A Bissett Ian A Kinloch Zheling Li Robert J Young Fang Wang, Suhao Li. Strain engineering in monolayer WS_2 and WS_2 nanocomposites. *2D Materials*, 7(4):045022, 8 2020.

[114] Si Huang Hugo Henck Zeineb Ben Aziza Laurence Ferlazzo Carl Naylor Adrian Balan Alan T. Charlie Johnson Jr. Rémy Braive Abdelkarim Ouerghi Julien Chaste, Amine Missaoui. Intrinsic Properties of Suspended MoS_2 on SiO_2/Si Pillar Arrays for Nanomechanics and Optics. *ACS Nano*, 12(4):3235–3242, 4 2018.

[115] Yinghui Sun, Rongming Wang, and Kai Liu. Substrate induced changes in atomically thin 2-dimensional semiconductors: Fundamentals, engineering, and applications. *Applied Physics Reviews*, 4(1):11301, 3 2017.

[116] Kailang Liu, Xiang Chen, Penglai Gong, Ruohan Yu, Jinsong Wu, Liang Li, Wei Han, Sanjun Yang, Chendong Zhang, Jinghao Deng, Aoju Li, Qingfu Zhang, Fuwei Zhuge, and Tianyou Zhai. Approaching strain limit of two-dimensional MoS_2 via chalcogenide substitution. *Science Bulletin*, 67(1):45–53, 1 2022.

[117] Oliver Iff, Davide Tedeschi, Javier Martín-Sánchez, Magdalena Moczała-Dusanowska, Sefaattin Tongay, Kentaro Yumigeta, Javier Taboada-Gutiérrez, Matteo Savaresi, Armando Rastelli, Pablo Alonso-González, Sven Höfling, Rinaldo Trotta, and Christian Schneider. Strain-Tunable Single Photon Sources in WSe_2 Monolayers. *Nano Letters*, 19(10):6931–6936, 10 2019.

[118] Taeyoung Kim, Yoonsok Kim, and Eun Kyu Kim. Characteristics of Cl-doped MoS_2 field-effect transistors. *Sensors and Actuators A: Physical*, 312:112165, 9 2020.

[119] John R. Vig. UV/ozone cleaning of surfaces. *Journal of Vacuum Science & Technology A*, 3(3):1027–1034, 5 1985.

[120] Abu Bakar, C H Azhari, Rozli Zulkifli, Abu Bakar Sulong, Che Husna Azhari, Mohd Roslee Othman, and Joohyuk Park. A Comparison of Defects Produced on Oxidation of Carbon Nanotubes by Acid and UV Ozone Treatment. *European Journal of Scientific Research*, 33(2):295–304, 2009.

[121] Youngsin Park, Nannan Li, Daesung Jung, Laishram Tomba Singh, Jaeyoon Baik, Eunsook Lee, Dongseok Oh, Young Dok Kim, Jin Yong Lee, Jeongseok Woo, Seungmin Park, Hanchul Kim, Geunseop Lee, Geunsik Lee, and Chan Cuk Hwang. Unveiling the origin of n-type doping of natural MoS_2: carbon. *npj 2D Materials and Applications 2023 7:1*, 7(1):1–7, 9 2023.

[122] Mengge Li, Jiadong Yao, Xiaoxiang Wu, Shucheng Zhang, Boran Xing, Xinyue Niu, Xiaoyuan Yan, Ying Yu, Yali Liu, and Yewu Wang. P-type Doping in Large-Area Monolayer MoS_2 by Chemical Vapor Deposition. *ACS Applied Materials and Interfaces*, 12(5):6276–6282, 2 2020.

[123] Ankur Nipane, Debjani Karmakar, Naveen Kaushik, Shruti Karande, and Saurabh Lodha. Few-Layer MoS_2 p-Type Devices Enabled by Selective Doping Using Low Energy Phosphorus Implantation. *ACS Nano*, 10(2):2128–2137, 2 2016.

[124] Richard FW Bader. Atoms in molecules. *Accounts of chemical research*, 18(1):9–15, 1985.

[125] Wencan Jin, Po Chun Yeh, Nader Zaki, Datong Zhang, Jerzy T. Sadowski, Abdullah Al-Mahboob, Arend M. Van Der Zande, Daniel A. Chenet, Jerry I. Dadap, Irving P. Herman, Peter Sutter, James Hone, and Richard M. Osgood. Direct measurement of the thickness-dependent electronic band structure of MoS_2 using angle-resolved photoemission spectroscopy. *Physical Review Letters*, 111(10):106801, 9 2013.

[126] Mit H. Naik and Manish Jain. Origin of layer dependence in band structures of two-dimensional materials. *Physical Review B*, 95(16):165125, 4 2017.

[127] Shishir K. Pandey, Ruma Das, and Priya Mahadevan. Layer-Dependent Electronic Structure Changes in Transition Metal Dichalcogenides: The Microscopic Origin. *ACS Omega*, 5(25):15169–15176, 6 2020.

[128] Esra Kuş, Gülay Altındemir, Yusuf Kerem Bostan, Cihat Taşaltın, Ayse Erol, Yue Wang, and Fahrettin Sarcan. A Dual-Channel MoS_2-Based Selective Gas Sensor for Volatile Organic Compounds. *Nanomaterials 2024, Vol. 14, Page 633*, 14(7):633, 4 2024.

[129] Florentino López-Urías, Ana Laura Elías, Néstor Perea-López, Humberto R. Gutiérrez, Mauricio Terrones, and Humberto Terrones. Electronic, magnetic, optical, and edge-reactivity properties of semiconducting and metallic WS_2 nanoribbons. *2D Materials*, 2(1):015002, 12 2014.

[130] Shao Long Xiao, Wen Zhe Yu, and Shang Peng Gao. Edge preference and band gap characters of MoS_2 and WS_2 nanoribbons. *Surface Science*, 653:107–112, 11 2016.

[131] Pavel V. Kolesnichenko, Qianhui Zhang, Tinghe Yun, Changxi Zheng, Michael S. Fuhrer, and Jeffrey A. Davis. Disentangling the effects of doping, strain and disorder in monolayer WS_2 by optical spectroscopy. *2D Materials*, 7(2):025008, 1 2020.

[132] Shijie Sun, Yurou Guan, Zhenliang Hao, Zilin Ruan, Hui Zhang, Jianchen Lu, Lei Gao, Xiaoqing Zuo, and Jinming Cai. Energy band engineering via "Bite" defect located on N = 8 armchair graphene nanoribbons. *Nano Research*, 15(1):653–658, 1 2022.

[133] Shyue Ping Ong, William Davidson Richards, Anubhav Jain, Geoffroy Hautier, Michael Kocher, Shreyas Cholia, Dan Gunter, Vincent L. Chevrier,

Kristin A. Persson, and Gerbrand Ceder. Python Materials Genomics (pymatgen): A robust, open-source python library for materials analysis. *Computational Materials Science*, 68:314–319, 2 2013.

[134] Xin He, Hai Li, Zhiyong Zhu, Zhenyu Dai, Yang Yang, Peng Yang, Qiang Zhang, Peng Li, Udo Schwingenschlogl, and Xixiang Zhang. Strain engineering in monolayer WS_2, MoS_2, and the WS_2/MoS_2 heterostructure. *Applied Physics Letters*, 109(17):173105, 10 2016.